ABSTRACT

Title of Document: COMPARISON OF FREE-VORTEX WAKE MODELS FOR A SUB-SCALE ROTOR AT LOW SPEEDS

Sean Howard Roark
Master of Science, 2007

Thesis Directed By: Dr. J. Gordon Leishman, Minta Martin Professor
Department of Aerospace Engineering

During shipboard testing in 1999, the V-22 Osprey tiltrotor experienced two separate uncommanded roll events as a result of an upwind-generated helicopter rotor wake, entrained in the ship's airwake, impinging upon its rotors. A portion of this thesis documents the author's involvement in one of the resulting wind tunnel tests created to investigate these events. The remainder details the attempts to validate the Maryland Free Wake (MFW) and Continuum Dynamics' CHARM free-vortex wake models using that low speed wind tunnel data. Results presented in this thesis show while the models qualitatively predict the downstream wake structure, they exhibit some interesting behavior in the far wake that is not in agreement with the measurements. To improve the correlation, changes to rotor parameters and the wake growth parameter were made, but with limited success. Potential explanations for the behavior are given, and recommendations for future research are also discussed.

COMPARISON OF FREE VORTEX WAKE MODELS FOR A SUB-SCALE ROTOR AT LOW SPEEDS

By

Sean Howard Roark

Thesis submitted to the Faculty of the Graduate School of the
University of Maryland, College Park, in partial fulfillment
of the requirements for the degree of
Master of Science
2007

Advisory Committee:
Dr. J. Gordon Leishman, Chair
Dr. James Baeder
Dr. Roberto Celi
Dr. Shreyas Ananthan

Acknowledgements

From attending the NASA wind tunnel test in November 2005 to my actual thesis defense two years later, numerous people from NASA, NAVAIR and the University of Maryland have made this effort possible. I would like to thank Wayne Johnson, Alan Wadcock, and Gloria Yamauchi from NASA, Mark Silva and Steve Donaldson, from NAVAIR, and Dan Waschpress from CDI. Each person helped out in their own way, and on their own time. Shreyas Ananthan and I have exchanged dozens of emails over the year and a half since he gave me the Maryland Free Wake code, and I am forever grateful for his patience and understanding, considering I tested both many times. I would also like to thank Dr. Leishman who has understood this author's off-site, part-time, graduate student status from the beginning and all that it entails. When work or life has gotten in the way of this research he has always been willing to work with me to determine a way forward. Lastly, I must thank my family and my girlfriend Catherine who have provided the love, support and motivation when I needed it the most.

Table of Contents

List of Tables

List of Figures

Nomenclature

a_1	Turbulent viscosity constant
C_T	Rotor thrust coefficient
I_b	Mass moment of inertia of the rotor blade in flapping, kgm^2
i, j,k	Unit vectors along the coordinate axes
M_A	Aerodynamic blade flapping moment, Nm
M_I	Inertial blade flapping moment, Nm
p, q	Roll and pitch rates, $rads^{-1}$
R	Rotor radius, m
Re_v	Vortex Reynolds Number
r_c	Viscous core radius of a vortex filament, m
r_{c0}	Initial core radius of a vortex filament, m
r	Position vector of collocation point, m
t	Time, s
u, v, w	Components of velocity along principal axes, ms^{-1}
V	Velocity vector at collocation point, m
V_∞	Forward flight speed of the helicopter, ms^{-1}, fts, kts
W_{mean}	Averaged out-of-plane velocity normalized by rotor tip speed
x, y, z	Cartesian coordinate system, m
x/R, y/R, z/R	Longitudinal, lateral, and vertical distance from hub

α	Blade sectional angle of attack, rad
β	Blade flapping angle, rad
Γ	Circulation associated with a vortex filament, m^2s^{-1}
Γ_v	Circulation associated with a finite length filament, m^2s^{-1}
$\Delta\zeta$	Discretization along spatial direction, rad
$\Delta\psi$	Azimuthal (or temporal) discretization, rad
δ	Turbulent or eddy viscosity parameter
ε	Strain rate, (= $\Delta l/l$)
ζ	Wake age, rad
λ	Non-dimensional inflow velocity
μ	Advance ratio
ν	Kinematic viscosity of air, m^2s^{-1}
ψ	Azimuthal angle, rad
Ω	Rotational speed of the rotor, $rads^{-1}$

Superscripts

*	
$(\,)^*$	Azimuthal derivative (= $\partial(\,)/\partial\psi = \Omega\partial(\,)/\partial t$)

Subscripts

i, j	General summation indices
x, y, z	Components of vectors along the principal coordinate axes

Maryland Free Wake Variables

mu	Advance ratio
muc	Climb ratio
pbar	Roll rate, (p/Ω)
qbar	Pitch rate, (q/Ω)
ct0	Required thrust setting
t0_0	Initial collective, deg
t1c0	Initial longitudinal cyclic, deg
t1s0	Initial lateral cyclic, deg
b0_0	Initial flapping angle (coning), deg
b1c0	Initial longitudinal flapping, deg
b1s0	Initial lateral flapping, deg
cttol, fltol	Thrust and flapping tolerances for trim
altitude	Operating altitude, m
nr	Number of rotors
nb	Number of blades
ns	Number of blade segments
asr0	Shaft tilt angle
rad	Blade radius
flph	Flapping hinge location (negative = teetering rotor)
rcout	Root cut-out
crd	Blade chord, m

twt	Blade twist, deg
om	Rotor rotational frequency, $rads^{-1}$
taperst	Starting point of taper
taper	Blade taper
rotgeo	Definition of rotor geometry
bmass	Blade mass, kg
kbeta	Flapping hinge spring stiffness
betap	Precone, deg
nw	Number of freewake trailers
pw	Number of prescribed wake trailers
nfw	Number of iterations
nk	Number of vortex cores to be used
ft	Number of free turns
bct	Boundary condition turns
dp	Azimuthal resolution, deg
dz	Wake resolution, deg
rcb	Initial core radius
dcy	Alpha parameter for core radius
trm	Trim procedure flag
lin	Linear aerodynamics flag
li	Vortex strength
method	Numerical scheme (t = time marching, r = relaxation)
initial	Initial solution flag (n = prescribed wake, b = old data)

CHARM Variables

NROTOR	Number of rotors
HEIGHT	Ground plane height, ft
U/V/W/P/Q/R	Velocities and rates of the aircraft in body coordinates
NSPI	Number of azimuth locations per blade revolution
NREV	Maximum number of blade revolutions in the trim solution
MREV	Number of time-marching revolutions after trim solution
IRST	Initial wake geometry flag
IFREE	Initial inflow model flag
IGPR	Solution method flag (time-marching or relaxation)
ISCAN	Flag to determine the velocity at a grid points in space
IFV	Flag for vortex method used (fast or aggressive hierarchical)
NSEG	Number of blade segments
CUTOUT	Blade cutout; distance from hub axis to blade root, ft
SL	Length of the span of each segment, ft
CHORD	Length of the chord, ft
TWRD	Twist at the blade root when there is zero collective pitch, deg
TWSTGD	Twist angle change per segment
THCKND	Blade thickness of each segment
NCHORD	Number of vortex lattice panels chordwise
NSPAN	Number of vortex lattice panels spanwise
ICOS	Vortex lattice spanwise spacing flag

NBLADE	Number of blades
OMEGA	Rotor angular velocity, $rads^{-1}$
IROTAT	Rotation direction (1 for CC from above, -1 for C)
ICOLL	Trim flag (trim to collective = 0, trim to C_T = 1)
COLL	Initial collective pitch, deg
CT	Thrust coefficient
ITRIM	Cyclic pitch inputs flag
NOWAKE	Free wake calculation flag
ICNVCT	Flag to include induced velocity effects on wake elements
NWAKES	Flag to ignore (or not) wake-on-wake induced effects
IFAR	Far wake flag
NBCVE	Curved or straight line segment vortex filament flag
ICORE	Vortex diffusion model flag
AKINEM	Kinematic viscosity for the vortex diffusion model, ft^2s^{-1}
A1	Turbulent diffusion coefficient in the vortex diffusion model
PCOREM	Power "*n*" used in the Vatistas core model
CRMON	Wake age at which the diffusion model begins
ISTRM	Structural mode input flag
IART	Hinge type indicator (Hingeless = 0, Articulated = 1)
HINGE	Distance of blade hinge from hub axis
PRECONE	Blade pre-cone angle, deg

Acronyms

AFCS	Automatic Flight Control System
C	Clockwise
CC	Counterclockwise
CDI	Continuum Dynamics Inc
CFD	Computational Fluid Dynamics
CVC	Constant Vorticity Contour
DCP	Differential Collective Pitch
FAA	Federal Aviation Administration
GTR	Generic Tilt Rotor
IGE	In Ground Effect
LDV	Laser Doppler Velocimetery
LIDAR	Light Detecting and Ranging
LLS	Laser Light Sheet
MFW	Maryland Free Wake
MIT	Massachusetts Institute of Technology
NAS	Naval Air Station
NASA	National Aeronautics and Space Administration
OGE	Out of Ground Effect
PC2B	Predictor Corrector 2nd Backward difference
PIV	Particle Image Velocimetry
RANS	Reynolds-averaged Navier–Stokes

R/C	Radio-Control
ROD	Roll On-Deck
RPM	Revolutions Per Minute
SBIR	Small Business Innovative Research
SIVE	Self-Induced Velocity Effect
SOF	Safety of Flight
VE	Vorticity Embedding
VSHAIP	V-22/Ship/Helicopter Aerodynamic Interaction
VTM	Vortex Transport Model
VWM	Vortex Wake Models
WOD	Wind Over-Deck

Chapter 1

1 Introduction

1.1 Problem Statement

A great amount of research has gone into understanding the wakes generated by the rotors of helicopters and tiltrotors. Most of the research has focused on understanding the flow field in, around and near the rotor disk, and for good reason. The rotor blades operate in a very complex environment, and one that is exceedingly hard to predict accurately. Many problems that are associated with helicopter flight, such as high blade loads, significant levels of vibration, and obtrusive noise can be understood and potentially mitigated once accurate modeling tools are developed that can detail this flow environment.

Experimental results, some of which are documented in this thesis, have shown that at least qualitatively, the downstream wake trailed from single and dual-rotor helicopters resembles that generated by a fixed-wing aircraft. This wake appears essentially as a pair of rolled up vortices. However, experience has shown that the exact nature of the wake trailed from a helicopter or tiltrotor is not known precisely, and this can have various consequences. For the U.S. Navy the inability to understand the downstream wake has resulted in various operational problems that not only have delayed aircraft acquisition programs, but also have resulted in loss of life in operational environments.

The primary objective of the work presented in this thesis is an attempt to validate, using sub-scale wind tunnel measurements, two free-vortex wake models currently being used by industry and academia: the Maryland Free Wake (MFW) and

Continuum Dynamics Inc (CDI) CHARM codes. These computer codes have been used successfully to predict the rotor wake's effect on rotor loads and performance, but these models, the MFW code in particular, have not been used extensively to investigate a helicopter's rotor wake numerous rotor radii downstream. For instance, in 2004, as part of a Small Business Innovative Research (SBIR) program, CDI made simplifying assumptions to their free-vortex wake model, CHARM, to make it viable for a real-time simulation environment. Beyond two rotor-diameters downstream of the rotor the CHARM free wake model was not used, and a simple, dual-vortex wake structure was put in its place. It was decided that beyond two rotor diameters using CHARM to account for all the vortex filaments became "inefficient" (Ref. 1). Also, the decay and diffusion rate of the rolled up vortices were not computed from first principles, but instead were modeled from algebraic formulations previously used to predict long time aircraft wake characteristics for the agricultural dispersal industry (Ref. 1).

1.2 Background

The basic idea of a helicopter has been around for hundreds of years. The Chinese had spinning tops as far back as 400 BC and Leonardo da Vinci's "aerial screw" is widely recognized as the first intended design of a heavier-than-air machine, although it was totally impractical. It was not until the late 1930s and early 1940s, however, that the first successful helicopters were designed, such as the Breguet–Dorand coaxial helicopter and the Fw-61 developed by Heinrich Focke in 1936. The Fw-61, a two-rotor design with the rotors mounted on outriggers in a side-by-side configuration, was the first helicopter to demonstrate fully controlled flight

and repeatable autorotations, and is arguably the first practical helicopter. Igor Sikorsky's VS-300, flying for the first time in 1939, and followed shortly after with his R-4, R-5, and R-6 models would serve as the template for most of the helicopter designs to follow during the next sixty years (Ref. 2).

Since the days of the VS-300, helicopters have progressed in their design, airworthiness, flight capability, and also in the number of ways they are utilized by an operator. The helicopter's ability to fly slowly and hover stationary in the air, combined with its ability to take off and land in confined areas have made it the perfect platform for search and rescue operations and the vehicle of choice to transport the critically injured to local hospitals quickly, and even as rooftop taxis in large cities. The helicopter has proven to be equally important to the military, and a modern military would simply fail to function without the use of helicopters.

In particular the U.S. Navy utilizes the helicopter for combat, antisubmarine operations, vertical replenishment of ships and submarines, and search and rescue, just to name a few roles. Some of the environments in which a U.S. Navy helicopter operates differ from those seen in the civilian world, or at the very least are environments that are seen more often by a U.S. Navy helicopter. While civilian helicopters operate around oil platforms and surface ships, U.S Navy helicopters such as the H-1, H-46, H-53 and H-60, as well as the V-22, were specifically designed to operate in the shipboard environment. Also, military helicopters and tiltrotors spend significant time taking off, flying and landing in formation (Fig. 1.1). Since they operate in extremely tight quarters, performing high workload tasks such as landing on a moving ship deck or flying in close formation, most of the time with other

rotorcraft in close proximity, the effects of their rotor wakes on a downwind rotorcraft cannot be ignored. Rotorcraft wake interactions, whether in a shipboard environment or while in formation flight, if not well understood and properly safeguarded against, can result in upsets that can damage the aircraft and cause injury to the pilots involved, or worse.

Figure 1.1: Five MH-60S helicopters perform a formation takeoff at NAS Norfolk.

The U.S. Navy invests millions of dollars a year conducting what it calls, "dynamic interface" testing. Surface ships are pulled away from combat duty or exercises to serve as floating wind tunnels for these tests. Test pilots and cadres of engineers spend days or weeks determining the operating Wind Over-Deck (WOD) envelope, defined in terms of wind azimuth and speed, for each helicopter and ship combination. A representative WOD envelope is shown in Fig. 1.2. While the ship

class, helicopter model, and wind azimuth and magnitude are all completely fictitious, this figure is representative of what is published and released to the fleet pilots for their routine use.

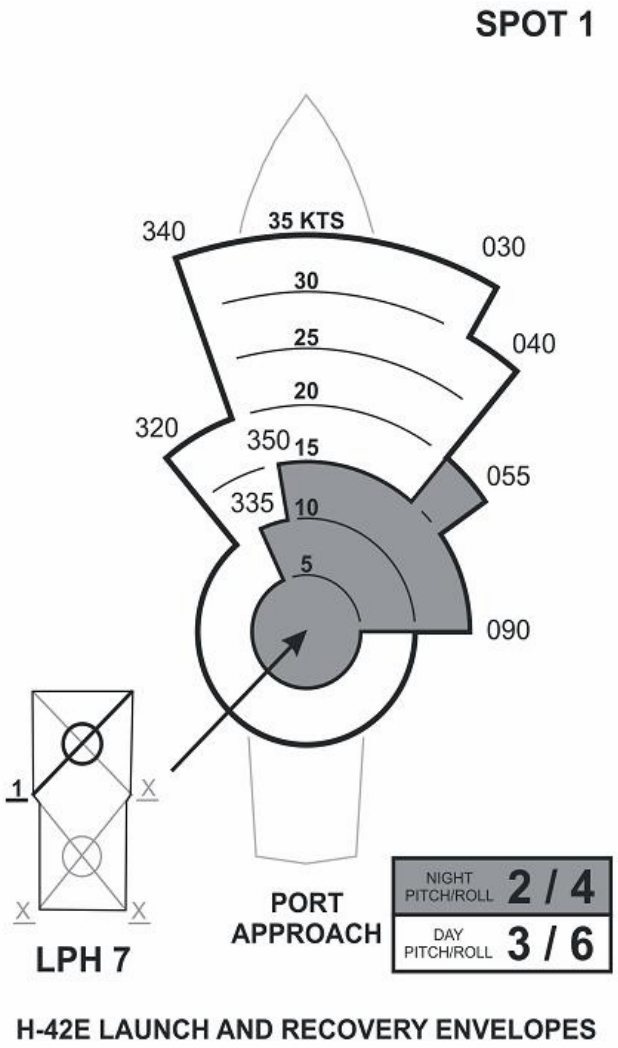

Figure 1.2: Sample WOD Envelope. Courtesy of the "dynamic interface" group at Patuxent River Naval Air Station.

The test team is subject to uncooperative weather conditions, helicopters that frequently break down, and the pressure of staying within cost and schedule. Similar test programs have been created to define safe separation distances and bearings between aircraft for formation flight. While flight test is what defines limitations and

sets guidelines, it is inherently inefficient, costly, lengthy and risky. There are even times when flight test can be almost deadly, even within areas deemed safe from previous flight testing because of unforeseen issues.

1.3 The Roll On-Deck (ROD) Phenomenon

1.3.1 A Description of the Incident

In January and August of 1999, shipboard compatibility testing was being conducted aboard the USS Saipan. During the testing, the V-22 Osprey tiltrotor aircraft experienced an uncommanded roll while on the deck with rotors turning, under the influence of the wake from a H-46 helicopter, estimated to be operating at 18,500 lbs gross weight, that was recovering in front of it. The recorded winds during both events were determined to be within acceptable launch and recovery WOD limits for the H-46 helicopter. These test events being the first time a tiltrotor was flown in a shipboard environment with other rotorcraft, no significant consideration was given to the upwind helicopter's influence on the V-22 while it sat on deck. The maximum V-22 roll from this complex ship, upwind helicopter, and on-deck V-22 interaction, was –5.8 degrees, as obtained during the January testing. The pertinent details of both incidents are given in Table 1.1.

Table 1.1: 1999 Roll On-Deck Conditions.

	Incident 1	Incident 2
Date	30 Jan 1999	20 Aug 1999
V-22 spot	8	7
V-22 Nr	88%	104%
H-46 spot	6	4
Spot separation	255 ft	315 ft
Wind over deck	357deg/38 kts	350deg/27 kts
Ship's roll angle	0.9 deg	1.3 deg
V-22 max roll angle	−5.8 deg	−4.5 deg

Video of the January event was captured by a flight deck camera and a frame taken from the video showing the moment of greatest negative roll angle during the January test event is shown below (Fig. 1.3).

Figure 1.3: January 30, 1999 ROD Incident.

As the H-46 approached its desired spot on the ship, the right outboard portion of its downstream rotor wake impinged on the V-22's left rotor. For reference, a "spot" is a designated landing area on the flight deck identified by the intersection of

three white lines, two at right angles to each other, with the third line at 45 degrees from the other two lines. A helicopter pilot aims to land with the helicopter's nose gear at the intersection of the three white lines, commonly referred to as "crow feet" using the lines for approach and line-up visual cueing. During the landing phase, the upwash from the H-46 increased the thrust on the V-22's left rotor causing an initial positive, right roll. In Fig. 1.3, it can be seen that the H-46 is approaching the second set of intersecting white lines from the on-deck V-22 Osprey. As the H-46 transitioned over its spot ahead of the V-22, the position of the H-46's wake at the V-22 rotors resulted in the left rotor experiencing a downwash while the right rotor experienced an upwash, resulting in a thrust asymmetry between the two rotors, and hence the larger magnitude negative, left roll. Although the pilots sitting on deck in the V-22 were able to return the aircraft to a wings level attitude, the resulting roll response from the wake interaction was so significant that the right main gear lifted off the deck and the weight-on-wheels sensor was tripped. This activated the in-flight flight control laws and engaged the Automatic Flight Control System (AFCS). When the AFCS engaged the flight control system gains changed from what they were on the ground without the pilots' knowledge. This was a Safety of Flight (SOF) issue that had to be addressed immediately.

Both incidents, the like of which had never been witnessed before with conventional helicopters, involved a light gross weight helicopter recovering multiple spots ahead of an on-deck V-22, as detailed in Table 1.1. The concern was that the phenomenon would only become worse with helicopters that had greater disk loadings and so potentially stronger downstream wakes, such as with the H-53 and V-

22. As a result of these two incidents, all shipboard compatibility testing was halted and multiple deficiencies were written against the V-22. These deficiencies had to be corrected prior to operational deployment. The resulting restrictions placed on the V-22 until the deficiencies were addressed were so prohibitive that a substantial test effort was initiated to not only understand the underlying causes of the ROD phenomenon but also to develop and demonstrate a permanent solution.

1.3.2 The Resulting Test Program

While it was clear that the wake trailed downstream from the H-46's rotors caused the uncommanded roll response of the V-22, the exact nature of the interaction was unknown. The effect of the upwind helicopter's gross weight, rotor configuration, and distance from the on-deck V-22 and above the deck of the ship could not be predicted. It was also unknown how the ship's own airwake influenced the interaction, and if there was a critical wind azimuth and magnitude that may have contributed to the problem.

It was decided that the resulting test program, created to understand the ROD phenomenon, would be divided into four parts: 1. Wind tunnel testing; 2. Simulation mathematical model development; 3. Computational fluid dynamics (CFD) analysis; 4. Flight test. The CFD analysis primarily focused on generating a time-accurate representation of an L-class ship's airwake at various WOD combinations to be used in the simulation analysis. This was done to understand how the ship's airwake interacted with the upwind helicopter's rotor wake. The mathematical model development involved taking the Generic Tilt Rotor (GTR) Math Model used by both

the engineering and training groups, and modifying the rotor model to accept the data obtained during the flight test effort (Ref. 3).

The flight test effort was broken up into multiple phases, the first being land-based downwash surveys. Using an array of ultrasonic anemometers mounted on aluminum polls, the height of which matched the height of the V-22 rotors off the deck, various helicopters were flown over them and the resulting downwash field was measured. Then, the same helicopters flew over a V-22 with rotors turning to provide a correlation between the measured downwash from the anemometers and the roll attitude response of the V-22. The second phase of testing involved conducting the same downwash survey as was done on land, but this time aboard an L-class ship in an attempt to understand how the ship's airwake affected the upwind helicopter's wake. Three helicopters, the H-1, H-46, and H-53 were used in this phase of the effort. Phase three involved an H-1 helicopter hovering over one spot in front of a chained down V-22 with its rotors turning. This helped to refine the test matrix for subsequent ship-based testing, and gave the test team further confidence that shipboard tests with heavier gross weight helicopters could be safely conducted. While the third phase of flight test was being conducted, the results from the second phase and analysis using the V-22 simulation both in batch mode and with pilots in the loop, were being used to develop the control law fix. This fix was to be done entirely in software, requiring no physical changes to the aircraft.

Phase four was the actual demonstration of the flight control law fix. The H-46, H-53 and V-22 were all flown in front of a chained-down, rotors turning, V-22 at various wind conditions deemed to be critical by previous flight test, wind tunnel and

simulation analysis. Because of the lack of sufficient winds during testing, and the disagreement of CFD with the wind tunnel measurements on the critical conditions, there actually ended up being three separate phase four testing efforts so that all critical conditions could be demonstrated. Despite all the setbacks, the V-22 exceeded all design goals for the control law fix (Ref. 4).

In parallel with, and in support of the flight tests, an extensive wind tunnel effort was undertaken. The goals of the test were to determine the critical conditions for the ROD phenomenon (upwind aircraft type, separation and WOD combinations) and to quantify the flow field at the V-22's rotors. The first objective would be accomplished by recording the forces and moments from an instrumented wind tunnel model of a V-22. The second objective required the use of particle image velocimetry (PIV) measurements (Ref. 5). The first phase of wind tunnel testing concentrated on quantifying the ship airwake, with and without an upwind aircraft, using PIV images (Fig. 1.4) and conducting a sensitivity analysis of WOD speed and azimuth, upwind aircraft position and gross weight and V-22 position and rotor thrust (Ref. 6).

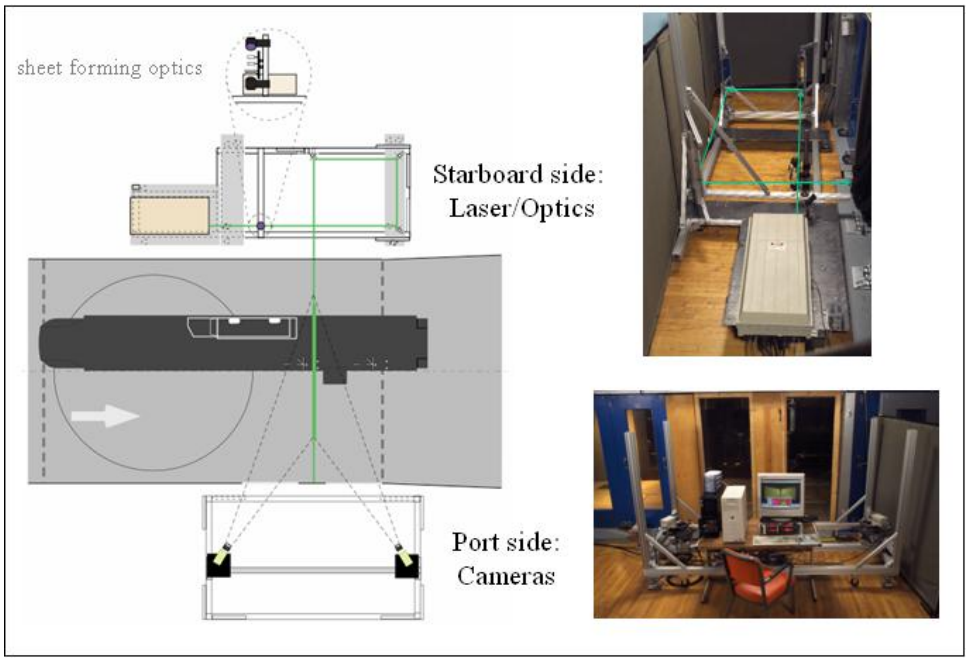

Figure 1.4: V-22/Ship/Helicopter Aerodynamic Interaction Phenomena (VSHAIP) PIV Setup.

The second phase of wind tunnel testing focused on the interactions between an on-deck V-22 and an upwind CH-53E and V-22, both believed to induce a greater ROD response than an H-1 or H-46 because of the higher disk loading and higher velocities inside the rotor wake from these aircraft (Ref. 4). Even though V-22 roll moment data was gathered while a model H-53 hovered at various upwind spots, no PIV data for the H-53 was gathered during the main VSHAIP testing periods (October 2001 through November 2003). Gathering such PIV data was the focus of the wind tunnel effort during November 2005, and the results were used in this thesis research to attempt to validate wake predictions made by the MFW and CHARM codes.

The ROD test effort, while successful, involved hundreds of engineers, took four years to solve, and costs millions of dollars. Through this effort, a better understanding of a helicopter's far wake characteristics and the interactions between

helicopters in a shipboard environment were obtained. The ROD phenomenon also generated a lot of increased interest within the aerospace community about the dynamic interface issue, and has helped motivate engineers to pursue development of a validated simulation tool that could accurately solve the fully coupled multi-aircraft, ship airwake problem. The technical challenges involved in creating such a tool are many and formidable. However recent research, an example being the ongoing work being conducted by Continuum Dynamics (Ref. 1) is showing some promise.

1.4 Formation Flight Wind Tunnel Testing

The other area where a helicopter's rotor wake strength and position are important to determine is in formation flight. As shown previously in Fig. 1.1, helicopters can operate in very close formation flight. There are special procedures and tactics that have been developed based upon years of flight test and user experience that explain to the pilot what flight formations are approved, as well as what are the required vertical and lateral separation distances for the trail aircraft(s). Similar procedures and tactics exist for fixed-wing aircraft. Because of the generally simpler nature of a fixed-wing aircraft's wake, those separation distances can be greatly reduced.

However the nature of the wake trailed downstream of a tiltrotor is less well understood. Wind tunnel tests conducted in the 7-by-10 foot wind tunnel at NASA Ames set out to determine the effects of forward airspeed, nacelle angle, flight-path angle, and rotor thrust coefficient on the lead ship's wake (Ref. 7). Also, the ability to safely recover from a wake encounter was studied in these tests by correlating the rolling moments generated on the trail aircraft to Differential Collective Pitch (DCP)

inputs, the primary lateral axis control used by the V-22 in helicopter mode flight. One of the main conclusions from one of the earliest wind tunnel tests was that at some point far downstream of the model tiltrotor, the wake resembles that of a fixed-wing aircraft, with two dominant rolled up vortices. Also, the rotor geometry was found to have little effect on the overall strength and location of the wake, the dependencies on advance ratio and thrust coefficient being the contributors to the primary effects that were seen (Ref. 7). The later tests conducted in 2004 and 2005 demonstrated that the V-22's wake did not weaken much with longitudinal downstream distance, and the vertical position of the wake was mostly dependent on nacelle angle and the flight path angle. The recommendation out of these tests was that the best way to avoid direct wake encounters, and the resulting roll-off, was to stay at least one wingspan laterally offset from the upwind aircraft (Ref. 8).

The work conducted to evaluate the V-22's wake structure focused primarily on helicopter mode operations at low speed with the nacelles pointed up almost vertically. The reason was that the models were of insufficient fidelity, being $1/48^{th}$ scale, to accurately account for the generation of wing lift at the higher airspeeds. These wind tunnel tests, as well as the complimentary flight test effort, were required to set the V-22's formation flight limitations. It is possible that had a validated analysis tool existed that could predict the size, strength, and position of the V-22's downstream wake, then a significant portion of the wind tunnel and flight test efforts would not have been necessary, saving both time and money.

1.5 Challenges in Modeling Rotor Wake

For a fixed-wing aircraft, the dominant feature of the far wake is a counter-rotating vortex pair originating from the wing tips (Fig. 1.5). For a helicopter, as speed is increased from the hover condition, the overall wake structure distorts and is skewed into an epicycloidal pattern behind the rotor. Interactions between the individual vortices trailed from the tips of each blade further distort the flow. At some speed, the individual vortex filaments roll up and form two so-called "super vortices" trailing from the edges of the rotor disk, and these resemble those generated from a fixed-wing aircraft.

Figure 1.5: Picture of fixed wing wake (Photo courtesy of airliners.net)

In Fig. 1.6, the downstream wake structure behind an SH-60 has been revealed from flares being ejected from the helicopter. It is interesting to note that the right vortex bundle, generated from the advancing side of the rotor disk has been convected farther down below the rotor than the left vortex bundle that has been generated by the retreating blades. Also, from examination of this picture, the cores

of both vortices (which are devoid of smoke) seem to grow as they age, but appear to reach more of a fixed size at later wake ages.

Figure 1.6: Downstream wake structure of a SH-60 helicopter.

In Fig. 1.7, the same type of downstream wake structure can be observed with the H-46, which shows that even for a dual rotor configuration at some point the wake also resembles the rolled up vortices that would be generated by a fixed-wing aircraft.

Figure 1.7: Downstream wake structure of a CH-46 helicopter.

For shipboard operations and formation flight, knowing the strength (circulation), size and position of the dual vortex cores and how they change over time is of the utmost importance for the downwind aircraft. Predicting those parameters is not easily undertaken though, because the helicopter rotor wake structure is a function of its advance ratio, thrust coefficient, collective and cyclic inputs to the rotor, tip path plane angle of attack, the presence of other rotors, and will also include aerodynamic effects associated with the tail rotor and the interference caused by the airframe (Refs. 2, 9).

A great deal of research has been conducted to determine essential wake parameters. The earliest recorded measurements using hot-wire anemometry of rotor tip vortices were in 1966 by Simons et al. (Ref. 10). Later research, as detailed in Ref. 11, postulated that the vortex core could be broken up into four distinct regions: a viscous core that is similar to the laminar sub-layer of a turbulent boundary layer, a

turbulent mixing region were the tangential velocity reaches its maximum at the outer edge, a transitional region where the turbulent inner core transitions into the outer inviscid region, and finally the outer irrotational region. This flow structure is depicted in Fig. 1.8.

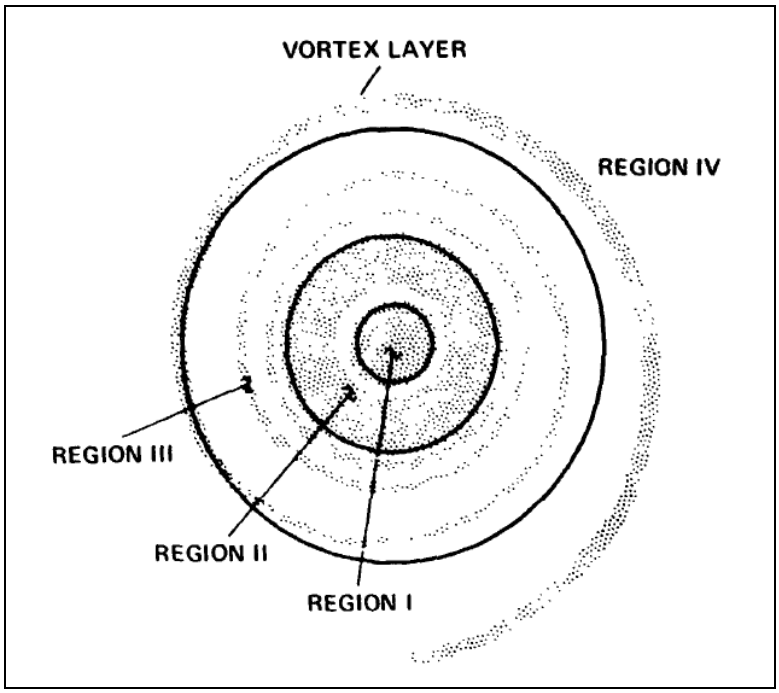

Figure 1.8: Vortex graphical depiction (Ref. 11)

The vortex structure, as depicted in Fig. 1.8, is similar than what is presented in Ref. 2. However in the work of Ref. 2, only the first three regions are described: a laminar core region, a transitional region and an outer turbulent region.

In 1972, Scully and Sullivan published the first tip vortex measurements made using laser Doppler velocimetery (LDV) (Ref. 12). This technique was a non-intrusive way to measure the rotor wake, and required the seeding of the flow with small particles and a way to illuminate the seed particles, in this case using a laser. However, there were several problems with this technique, such as the need to

uniformly seed the flow and the difficultly in getting the right optical access for the cameras to record the images. Work done much later by Martin, Bhagwat and Leishman in 1999 using LDV further documented how the vortex sheet from the blade and the tip vortex interact with each other (Ref. 13). The results from this test and others like it furthered the understanding of the rotor wake, allowing for the development and validation of more effective mathematical models of the vortex flow.

Research was conducted in 1984 by Bell Helicopter on full-scale aircraft using a light detecting and ranging (LIDAR) system developed by the Massachusetts Institute of Technology (MIT). The test aircraft used were the UH-1H and the CH-54. The LIDAR technique held great promise when the appropriate seeding technique was chosen. Results from these tests indicated that the measured vortex strengths from the two helicopters matched well to the results obtained using simple circulation theory for a fixed-wing when the rotor diameter was used in place of wing span (Refs. 14, 15).

The FAA conducted further research in 1985 and 1987, and concluded that the downstream rotor wake resembles that of a fixed-wing wake for airspeeds greater than about 40 kts. At speeds less than that, the wake vortex roll up mechanism diappears and the wake more closely resembles that of a skewed helix. Also the rolled up vortex on the advancing side of the disk was stronger than the one on the retreating side, and in general the stronger vortices decayed more quickly than the weaker ones (Ref. 16).

In 2000; Bell Helicopter went back and conducted further research using the LIDAR system with a XV-15, a V-22, and a 205B helicopter. This was the first full-scale test that measured the downstream wake trailing from tiltrotors. The work showed that the tiltrotor wake characteristics of a tiltrotor were similar to those of a fixed wing aircraft. In all cases investigated, both the XV-15 and V-22 aircraft were found to trail two main vortex bundles that were separated by an effective span distance. For helicopter mode, the effective span was the distance between outboard rotor tips, and for airplane mode it was the wing tips. In helicopter-mode flight, the vortices trailed from the inner (retreating) sides of the rotor disk appeared to cancel each other out, leaving just the outer blade tip generated vortices (Ref. 17).

1.6 Various Methods Available To Model the Rotor Wake

Wind tunnel, flight tests and photographic analysis have shown that both tiltrotor and helicopter wake resembles fixed-wing wake above a certain speed, where the roll-up mechanism exists to create the two "super vortices." As mentioned previously, accurately predicting the position, strength and size of these "super vortices" is extremely difficult. There are mathematical tools available, however, that can predict helicopter rotor wake but with varying degrees of accuracy. The tools can be divided into four main categories: Vortex Wake Models (VWM), CFD models, hybrid VWM/CFD models, and Vortex Transport Models (VTM).

The first category can be further divided into prescribed and free-vortex wake models. Prescribed wake models set the location of the helical vortex filaments based upon rigid (epicycloidal) wake equations combined with distortion functions derived from experimental measurements of wake displacements as functions of wake age.

While researchers such as Egolf and Landbrege (Ref. 18) and Beddoes (Ref. 19) have tried to develop very general forms of prescribed wake models to account for the primary wake distortion, the main disadvantages with these models are still that they are not fundamentally predictive in nature, and cannot accurately predict the wake roll-up and bundling of tip vortices that have been observed in experiments (Refs. 2, 9).

Free vortex wake models, which include the MFW and CHARM codes, solve for the wake geometry, location and strength directly through repeated application of the Biot–Savart law integrated over all vortex elements in the rotor wake. These methods do not rely on experimental data for formulation purposes, so are able to make predictions for flight regimes not already explored in experiments. The vortex filaments can be modeled as straight or curved lines, or three-dimensional vortex blobs. The MFW code uses contiguous segmented straight lines, while the CHARM code uses curved filaments. Lagrangian markers are affixed to the various vortex filaments and the governing equations are solved at these markers.

The free-vortex wake models can be further divided into relaxation and time-marching methods. Relaxation methods assume periodicity of the rotor wake. A relaxation parameter within the equations is modified until the wake markers do not change their positions appreciably between iterations. This method works well for most steady-state flight conditions, but for transient flight conditions, such as maneuvering flight or descents or some types of in-ground-effect conditions, a time-marching method is required.

The majority of free-vortex wake methodologies do not account for vortex core growth, viscous and turbulent diffusion, filament strain, and the merging of vortex cores, however as documented in Ref. 9 the MFW does attempt to model these effects based on various types of vortex models. Most free-vortex codes assume an arbitrary vortex core size to aid in the numerical stability of the program, although this is not a characteristic of the MFW. It is also important to account for filament strain because Helmholtz's third law requires the net strength of any vortex filament to remain constant, therefore, requiring that the product of the cross-sectional area and vorticity to remain constant. If a filament is stretched, as it inevitably is as it is convected inside the rotor wake, its cross-sectional area must decrease, increasing both the vorticity and local induced velocity. If filaments are in close proximity to each other, this stretching effect can have a substantial impact on the overall structure of the rotor wake (Ref. 20).

A limitation of free-vortex wake methods is that they cannot predict the creation of vorticity on the surface of the blades, so that they are incapable of modeling the entire life of a vortex filament. The free-vortex methods must rely on empirical and theoretical results for the initial condition of the tip vortex flow, and by coupling roll up models with classical forms of lifting line theory.

CFD methods, at least in principle, are capable of predicting the creation of vorticity on the surface of rotor blades, its convection into the vortex sheet, and the creation and roll up of the tip vortices. But these methods require very fine Eulerian grids to prevent numerical dissipation of the vortex structures (Ref. 9). The large number of grid points required to obtain an accurate vortex flow structure beyond one

or two rotor revolutions makes these methods computationally expensive, perhaps even impractical. Rotorcraft CFD methods can handle both the rotating and non-rotating components, unsteadiness in the flow field, can predict hovering rotor performance with a reasonable degree of accuracy, can handle advancing blade transonic flow, and can model fairly complex fuselage geometries. However as of yet, CFD cannot account for aerodynamic and dynamic blade coupling, trim such that all forces and moments are in balance, handle rotor-wake/fuselage interactions well, capture blade-vortex interactions, vibrations or acoustics, or account for separated flows as seen in rotating blade stall in practical rotor problems. While advances in the CFD field continue to be made, the deficiencies mentioned above may still yet require major advancements in computer hardware or the creation of new algorithimic approaches to fully solve them (Ref. 21).

Attempts have also been made to combine the best of the FVM and CFD. The first method is the Vorticity Transport Method (VTM). By assuming the rotor wake is incompressible, the governing equations are solved, not in the conservative variable form, but directly in terms of velocity and vorticity. By solving the equations this way, the problem of artificial numerical vorticity dissipation is avoided (Ref. 2). The second method is a hybrid FVM and CFD hybrid. One example of a hybrid method is the one contained in Ref. 22 where an inner Reynolds-averaged Navier–Stokes (RANS) code provides the circulation information to the outer vorticity embedding (VE) force-free vortex wake code. The wake geometry is then computed with this VE code. In turn, the velocity field information is used as the outer boundary for the RANS code. The solution is iterated until some convergence criteria is met.

Comparisons to available experimental hover performance data are favorable, but the current method cannot predict the performance limits of a rotor configuration because the RANS solver cannot properly model turbulence and flow separation (Ref. 22). It may not be necessary to model most of the near wake phenomenon using first principles, so a FVM methodology may be sufficient to capture the majority of the flow field characteristics in the far wake; CFD and hybrid solutions may not be required.

1.7 Outline of the Thesis

In this introductory chapter, the reasons for needing a validated mathematical model that can predict the size, strength and position of a helicopter's far wake were presented in Sections 1.1 and 1.2. The general challenges of helicopter rotor wake modeling were discussed in Section 1.3. A brief summary of available computational tools capable of modeling the wake, as well as their strengths and weaknesses, was also discussed in Section 1.4. The remaining sections of this thesis are divided into five chapters. The details of the wind tunnel test, including a description of the H-53 model, the PIV setup, and a discussion on how the data was gathered, is contained in Chapter 2. Chapter 3 is devoted to a discussion of the MFW and CHARM mathematical models. Chapter 4 documents the results of the validation effort using the available wind tunnel data, and the numerous challenges encountered during this effort. Chapter 5 summarizes the main conclusions of this work, and provides recommendations for future research on the problem.

Chapter 2

2 Description of Test

This chapter explains, in detail, the NASA wind tunnel test that was directly supported by this author during November 2005. PIV data for a 1/48th scale H-53 was gathered under a U.S. Navy funded effort. All data from the ROD testing and V-22 Formation Flight Wind Tunnel tests presented in this thesis has been previously cleared for public release. While there does not exist any publicly released reports on the H-53 wind tunnel testing, the author has obtained permission from NASA to use the wind tunnel data for the work conducted in this thesis.

Although the author participated in the November 2005 wind tunnel test, reduced and analyzed data from it, the overall scope and intent of the this test was determined by the Navy's representative, Mark Silva. The follow-on H-53 wind tunnel testing, scoped and subsequently conducted by Alan Wadcock of NASA, was done with the remaining funds from the Navy contract and had no direct Navy involvement. While the author has been given complete access to the data from the follow-on testing, the author was not involved with the actual test itself.

2.1 Justification for Model Scale

The U.S. Navy engineers involved in this wind tunnel test program postulated that the solution to the ROD phenomenon was a function of the ship's airwake, the WOD, the characteristics and position of the upstream helicopter, and the operating state of the on-deck V-22. This meant that to represent the full-scale ROD event with a sufficient degree of fidelity, the primary parameter was the ratio of the rotor-

induced velocity of the upwind helicopter to the free stream velocity, effectively its wake skew angle. This allowed for a fair amount of latitude in the model scale used. If the advance ratio and thrust coefficient of the upwind helicopter was representative of the full-scale helicopter, the basic structure of the wake should be captured. The fidelity of the fuselage was deemed to be less important because, at the low speeds planned for the wind tunnel test, the far downstream wake was unlikely affected by the fuselage aerodynamics

For these tests, a scale model of a LHA-class ship was constructed. The ship model was mounted to a turntable in the test section of the tunnel to allow for the ship to be yawed. This allowed for the simulation of port winds. The model could not be too big, however, before blockage effects in the working section would become large at the yaw angles planned for the test (Fig. 2.1).

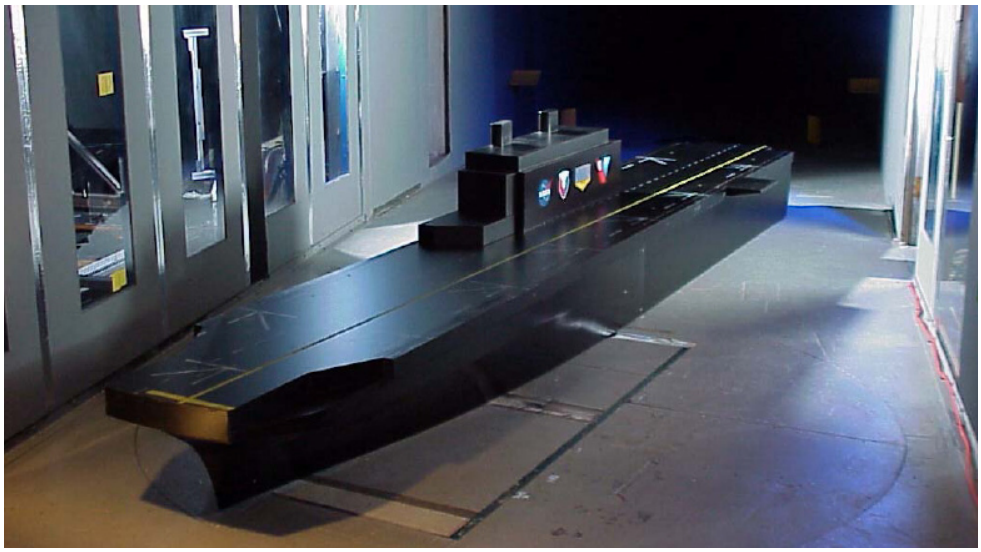

Figure 2.1: LHA Model in the 7 x 10 NASA Wind Tunnel Test Section.

There were also lower limits to the model size required for the wind tunnel tests. For all of the H-46, H-53 and V-22 models, one requirement was that there had

to be room for the six-component balance. This was especially true for the V-22 model, as it would be placed on the surface of the LHA model within the tunnel as the various models were positioned upwind; the primary data gathered for those points being rolling moment for the V-22.

The ability to set collective pitch on the rotors to obtain a certain thrust coefficient at a given RPM was also a requirement. While fully articulated rotors were desired, especially for the H-46 and H-53 models so as to be able to zero out the rolling moment when they were used as the upwind aircraft, this was not a requirement. After considering all the ship and helicopter model constraints, a $1/48^{th}$ scale was decided upon. An added bonus of picking this particular model scale was it allowed the test team to use commercially available model aircraft fuselages to provide some increase in model fidelity. For the test directly supported by this author, the ship model was not used but the H-53 model from the original VSHAIP testing was used instead.

Because of the performance limitations of the electric motors driving the rotors, the tip speed of the H-53 model was limited to 33% of its full scale value. To ensure that the proper advance ratio was obtained, the speed of the flow in the tunnel was set to 33% of the desired full-scale test condition (Ref. 6).

2.2 Wind Tunnel Facility and H-53 Model Description

The tests were conducted in the U.S. Army Aeroflightdynamics Directorate's 7-by-10 foot wind tunnel. This tunnel was located at the NASA Ames Research Center at Moffett Federal Airfield, Mountain View, California. The test section measured 7-ft high, 10-ft wide, and 15-ft long. In the return duct, four turbulence-

reducing screens were installed to ensure that the flow contained minimal turbulence, which would adversely affect the PIV results. The test section had a traverse system installed for the H-53 model, thereby allowing it to be positioned longitudinally, laterally or vertically anywhere in the tunnel. For the tests used in this thesis, the traverse was used to ensure the rotor wake was as close to in the center of the PIV laser sheet as possible (Refs. 6, 24).

The key full-scale geometric properties that were matched are given in Table 2.1 (Ref. 23).

Table 2.1: Full-scale Aircraft Dimensions.

	V-22 Osprey	CH-46	CH-53E
No. of rotors	2	2	1
No. blades per rotor	3	3	7
Rotor radius (in)	228.5	306.0	474.0
Blade tip chord (in)	22.00	18.75	29.28
Rotor solidity	0.105*	0.059†	0.138†
Rotor RPM (100%)	397	264	177
Tip speed (ft/s)	792	705	732
Blade tip Reynolds number	9.26×10^6	7.03×10^6	11.39×10^6

* Thrust weighted

† Geometric

In Table 2.2, the actual geometric properties of the model are listed. The data contained in Table 2.2 has been updated from what was contained in Ref. 23 to reflect the changes made to the model between the completion of testing in 2003, and the test event this author participated in during 2005. Low Reynolds number airfoils were used on the blades, and a linear twist distribution was used that very closely matched that of the full-scale rotor.

Table 2.2: Model-Scale Geometric Properties.

	Single Main Rotor Helicopter
No. of rotors	1
No. blades per rotor	5
Blade retention pin radius (in)	1.585
Blade root radius (in)	1.735
Blade root cut-out	0.176
Measured rotor radius (in)	9.875
Blade tip chord (in)	0.854
Rotor solidity	0.137†
1/48th-scale rotor radius (in)	9.875
Airfoil sections used	SD7032, MD5014, MD5518
Twist distribution	-15.9
Target tip speed (ft/s)	252
Target rotor RPM	2,831
Blade tip Reynolds Number	114,604

† Geometric

All of the models used rigid hubs and as mentioned before, only had collective pitch control. Commercially available radio-control (R/C) tail-rotor assemblies were used for the model hub and control systems. The H-53 model used one Cobalt-40 electric sport motor. Commercially available R/C transmitters, receivers, speed controls, governors and control servos were used in the H-53 model (Ref. 23). Figure 2.2 shows the major components of the H-53 model.

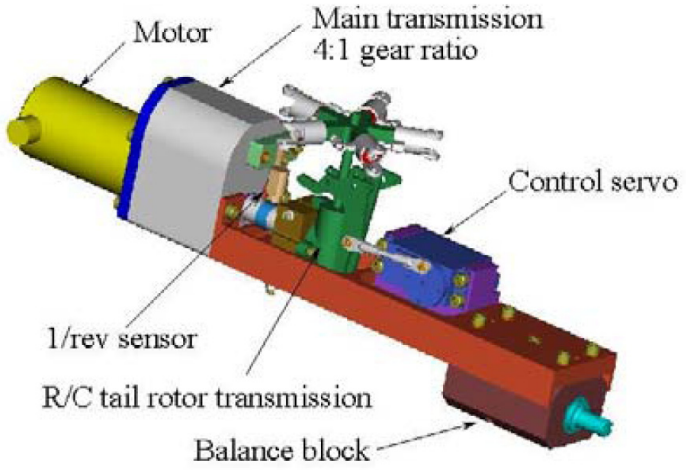

Figure 2.2: 3-D Graphical Depiction of the H-53 Model Major Components.

Figure 2.3 shows what the H-53 model looked like when installed in the test section of the wind tunnel.

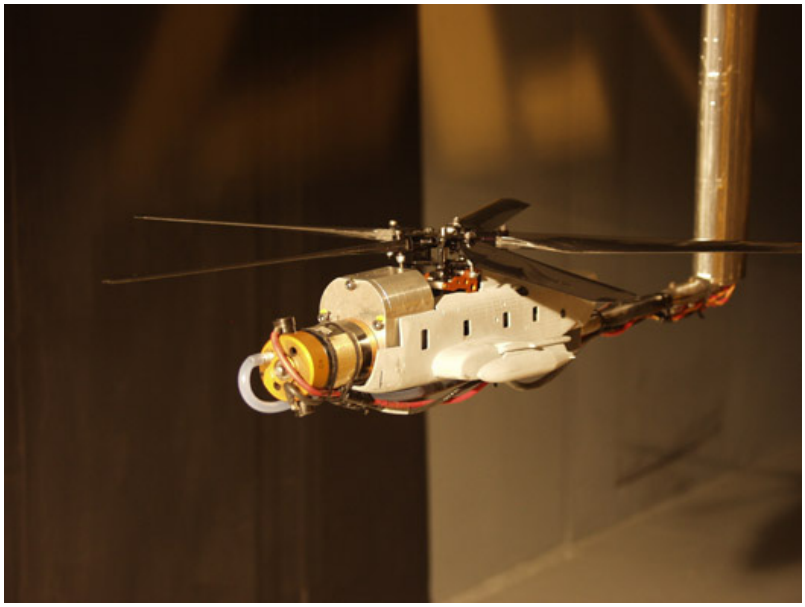

Figure 2.3: H-53 Model in the Wind Tunnel Test Section.

Figure 2.4 provides a good top view of the H-53 model, detailing the rotor hub, collective pitch links, and overall blade planform.

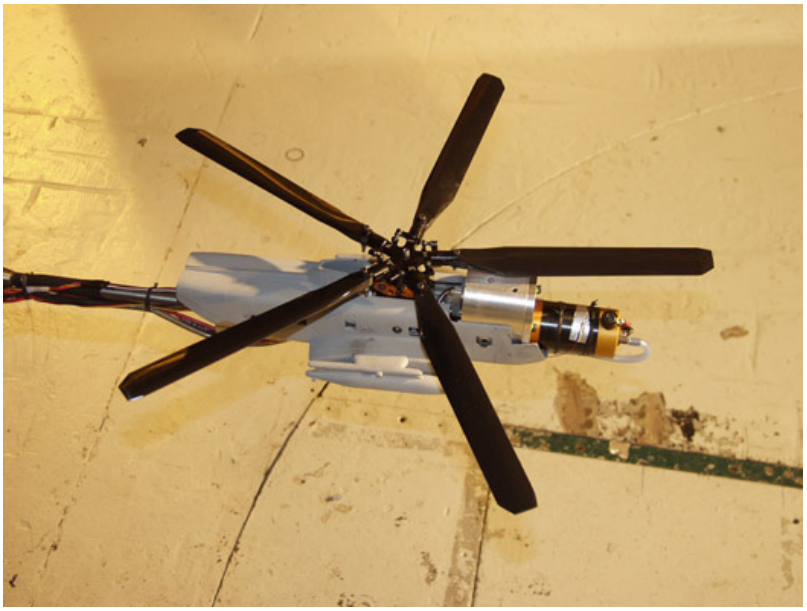

Figure 2.4: Top View of the H-53 Model.

2.3 PIV Installation

The PIV setup used for this test is shown in Fig. 1.4, without the ship model installed in the tunnel. The laser light sheet (LLS) was placed in a fixed location in the tunnel, and to obtain measurements at different downstream distances the H-53 was moved using the traverse. The PIV measurement plane was approximately 6-ft wide by 3-ft tall, centered in the center of the tunnel. The nominal thickness of the LLS was 6 mm.

The laser used in wind tunnel tests was a Spectra Physics PIV 400 dual-oscillator Nd:YAG laser with a 350 mJ/pulse at 532 nm wavelength. Sheet intensity variation from one side of the tunnel to the other was minimized by folding the LLS back on itself using mirrors. To ensure a sufficient resolution was obtained, two Kodak ES 4.0 2k-by-2k digital cameras were used. These two cameras, as detailed in Fig. 4, were offset 30 degrees from the PIV light sheet plane and outfitted with 50 mm f/1.4 Nikkor lenses. To seed the flow for this test, a single Corona Integrated

Technologies Vicount 5000 2.2 kW Series 180 mineral oil smoke generator was used. The seed particles were injected downstream of the model at the end of the test section (Refs. 24, 25). This author watched this process and observed NASA engineers at the beginning of each run taking multiple pictures of the flow field before starting the H-53 rotor, but after the wind tunnel had stabilized at the correct speed, to ensure a uniform distribution of the seed particles had occurred.

The maximum out-of-plane particle displacement allowed was just 25% of the nominal LLS thickness. The maximum in-plane displacement allowed was just 4 pixels. The data was processed with a 24-pixel cross-correlation window. This resulted in a spatial resolution of 0.8-in in the horizontal direction and 0.4-in in the vertical direction. Converted to full-scale, this resolution is equivalent to obtaining all three components of velocity every 3.4-ft horizontally and 1.7-ft vertically. The PIV data was gathered at a rate of 2 Hz. For each point, fifty sequential images were collected then ensemble-averaged for the processed wind tunnel image. No attempt was made to synchronize the images with the azimuthal position of the rotor blades, or correct for any aperiodicity of the wake as the intent of all the VSHAIP tests including this H-53 test was to obtain the time-averaged velocity field at specific points downstream of the rotor disk (Refs. 24, 25).

2.4 Summary

The results obtained from the first tunnel entry, Run 175, were used by V-22 engineers to validate their simulation tools and helped to better understand how the rotor wake from a H-53 compares to that from a V-22. The results from Run 176, while not used in support of the ROD effort, were extremely valuable as they show

how rotor wake changes with advance ratio and thrust setting. The results from both wind tunnel runs provide an excellent data set that can be used to validate the MFW and CHARM models. A brief summary of both models is provided in the following chapter.

Chapter 3

3 MFW and CHARM Free Wake Model Descriptions

3.1 MFW Model

As detailed in Ref. 9, the current version of the MFW model has various sub-components to handle the two main contributors to the free-vortex wake problem: the blade and its wake. These sub-components can be divided into four main models: the blade aerodynamic model, the blade flapping dynamics model, the free-vortex wake model, and the sub-models to handle the viscous and strain effects in the vortex filaments. The first two models are needed to determine the initial positions of the tip vortices and their circulation strengths, while the latter two are required to determine how the vortex filaments interact with each other as they age.

3.1.1 The Blade Aerodynamic Model

The blade aerodynamic model must, in general, incorporate a wide array of complicated aerodynamic phenomena, such as unsteady and dynamic stall effects, the spanwise variation of the blade's nonlinear lift and drag, and the bound circulation of the blade. In the current version of the MFW model, the user is able to specify the number of rotor blades. The only limitation for the numerical solution algorithm is that 360 degrees divided by the number of blades must be an integer number. This means that currently MFW is unable to model a seven-bladed rotor, for example. Each of the rigid, articulated blades modeled in MFW are allowed to flap freely,

independently from each other. The ability to lead and lag is not currently modeled but this effect is small compared to flapping.

Aerodynamically, each blade is modeled as a collection of horseshoe vortices. This Weissinger-L lifting surface model (Ref. 26) is graphically depicted in Fig. 3.1. The strength of the trailed vortex elements is determined using Helmholtz's laws of vorticity conservation (Ref. 27). The trailed vortex elements, as depicted in Fig. 3.1 are truncated after a short distance, typically $\Delta\psi = 30°$; afterwards only the tip vortices are carried into the far wake and used to calculate the induced velocity field. The strength of the bound circulation is a function of the free stream velocity, the additional velocities due to any flight maneuvers and the induced velocity of the wake. The nonlinear lift and drag characteristics needs to be modeled because each section of the rotor blade operates at different angles of attack, sometimes near stall, and at different Mach numbers. Beddoes' two-dimensional, nonlinear airfoil model is used to obtain the airloads on the rotor blade, separated into a normal and tangential force (Ref. 28) and corrected for compressibility effects using the Prandtl–Glauert correction factor. The unsteady aerodynamic forces, comprised of both circulatory and non-circulatory components, are calculated using the indicial response method of Leishman and Beddoes (Refs. 29, 30, 31). The normal and tangential forces are summed over all of the rotor blades to obtain the total rotor forces and moments at any given time.

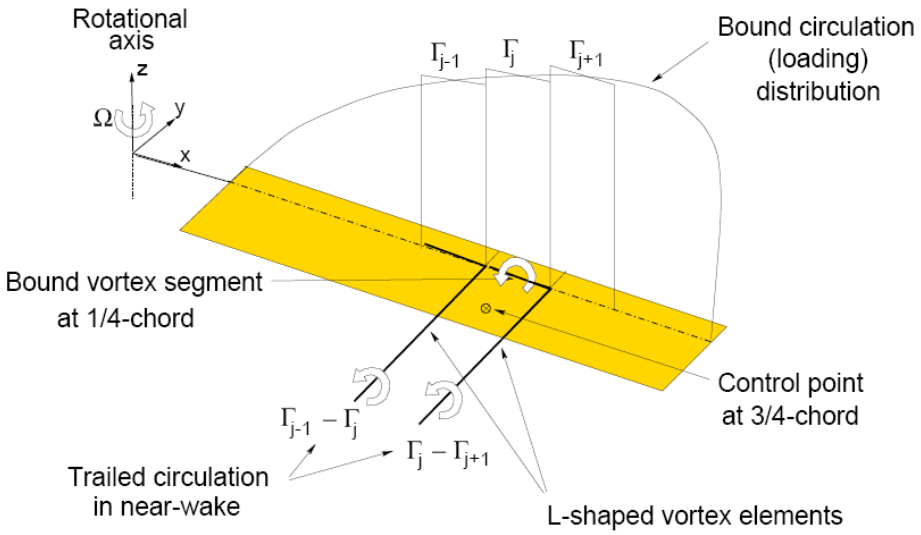

Figure 3.1: Weissinger-L Lifting Surface Model.

3.1.2 The Blade Flapping Model

Blade flapping affects not only each blade element's angle of attack but also must be known to determine the origination point of the tip vortex filament. Therefore, the blade flapping response and the rotor wake solution is coupled, and must be solved simultaneously.

3.1.3 Outline of Wake Calculation

Once the initial position and strength of the vortex filaments have been determined, how those two parameters change as a function of time now must to be calculated. As seen in Fig. 3.2, this is done first by placing Lagrangian markers on all the vortex filaments.

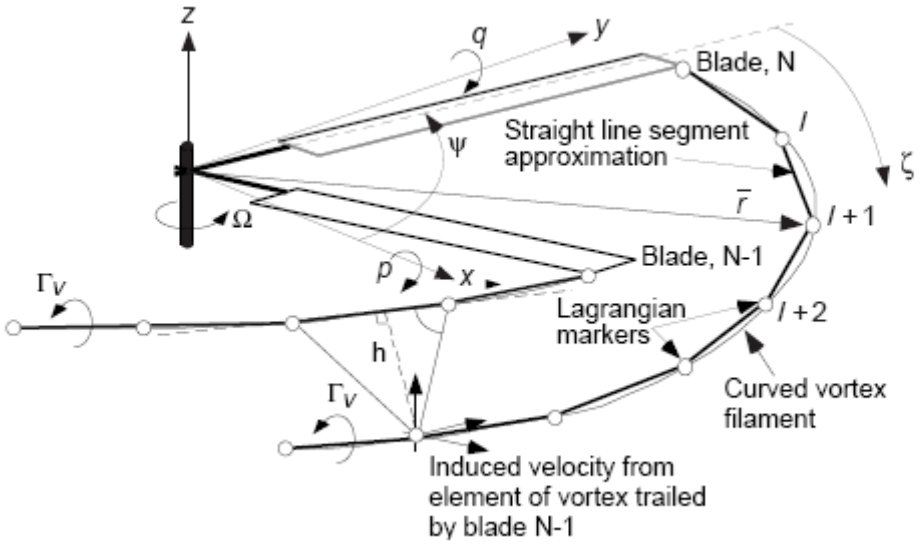

Figure 3.2: Representation of the Vortex Filaments.

The vortex filaments are allowed to convect to force-free positions and their movement is governed by the incompressible, Navier–Stokes equation written in velocity-vorticity form for each filament marker. In the current version of the MFW model, the vorticity is contained entirely within each vortex filament. The position of each filament is determined by solving the convection equation, of the form

$$\frac{\partial \mathbf{r}}{\partial \psi} + \frac{\partial \mathbf{r}}{\partial \zeta} = \frac{\mathbf{V}}{\Omega} \tag{1}$$

where Ω is the rotor angular velocity, and **V** is the total velocity at each marker. The wake position as seen in Eq. 1 is a function of the azimuthal position of the blade (ψ) and the age of the filament (ζ) relative to the time that it was deposited into the wake.

The terms on the left-hand side of Eq. 1 are approximated using finite differences. In the current version of the MFW model, a numerical scheme called a predictor-corrector, two-step backward (PC2B) scheme, proposed in Ref. 32, is used

to solve Eq. 1. This PC2B scheme is second-order accurate. The spatial derivative is approximated by a five-point central differencing scheme (Fig. 3.3).

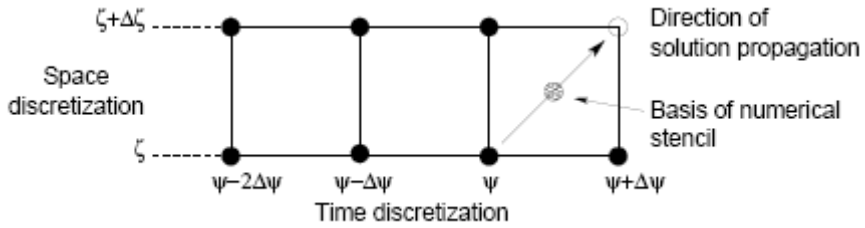

Figure 3.3: Graphical Representation of the PC2B scheme.

3.1.4 The Viscous and Filament Strain Effects

Equation 2 does not have any terms describing the viscous or filament strain effects. This may be sufficient for certain applications, but such effects need to be included for flight regimes where the vortex filaments are in close proximity to each other to model such phenomenon as wake roll up and vortex bundling. As depicted in Fig. 3.4, the viscosity and strain effects are handled separately, then the results of each sub-process is combined before moving on to the next iteration step.

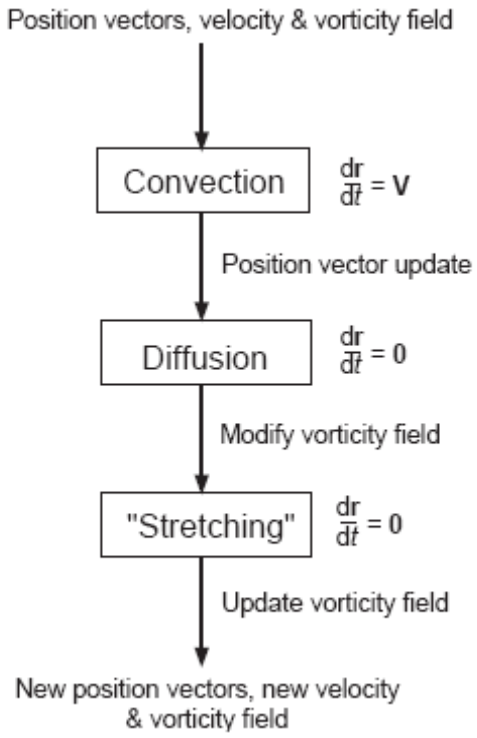

Figure 3.4: Depiction of viscosity and strain sub-processes.

The first step determines the location of the vortex filaments at the current time step after they have been influenced by their local velocity field. In the second step, the viscous core radius for each filament is calculated based upon its age relative to when it was released into the flow and is defined by

$$r_c(\zeta) = \sqrt{4\alpha\delta\nu\left(\frac{\zeta+\zeta_0}{\Omega}\right)} \equiv \sqrt{r_{c_0}^2 + \frac{4\alpha\delta\nu\zeta}{\Omega}} \tag{2}$$

where δ and ζ_0 are defined empirically (Ref. 33). The δ variable, referred to as the turbulent eddy viscosity coefficient or the apparent average eddy coefficient is a function of the vortex Reynolds number and is defined as

$$\delta = 1 + a_1\left(\frac{\Gamma_v}{\nu}\right) = 1 + a_1 Re_v \tag{3}$$

where a_1 is determined as an average from many different vortex measurements. As seen in Fig. 3.5, from Ref. 34, the value of a_1 differs greatly and picking an appropriate value for all applications, both at sub- and full-scale can be difficult.

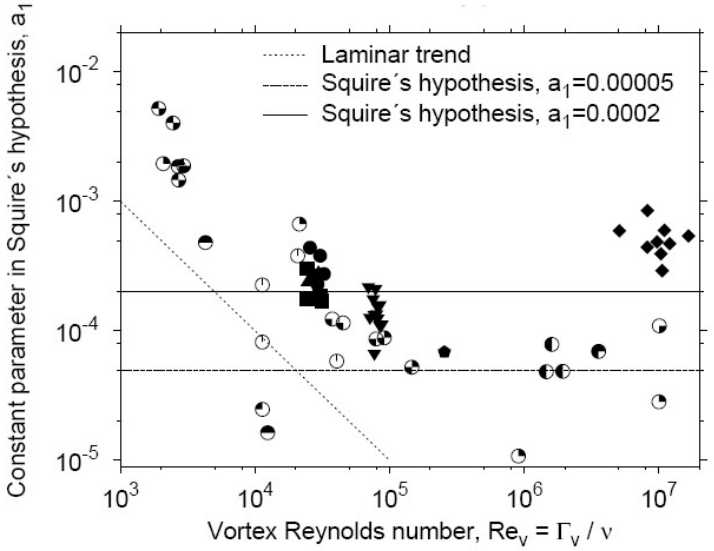

Figure 3.5: Squire's hypothesis constant parameter.

Filament strain, positive being filament stretching, causes the core area of the vortex filament to decrease, increasing its vorticity assuming the flow is incompressible and that the density remains essentially constant. This strain modifies Eq. 2 and the resulting viscous core growth equation with filament strain effect included now is of the form:

$$r_c(\zeta,\varepsilon) = \sqrt{r_{c_0}^2 + \frac{4\alpha\delta(Re_\nu)\nu}{\Omega}\int_0^{\zeta}(1+\varepsilon)^{-1}\,d\zeta} \tag{4}$$

where ε is defined as the change in filament length divided by the original length.

3.2 CHARM Model

CHARM, the free-vortex wake model formulated by CDI has been used for a few SBIR-funded efforts, one of which is documented in Ref. 1. The CHARM model, like the MFW model, is a coupled rotor and wake model with the capability to not only predict the development of the rotor wake, the wake-induced airloads, and the dynamic response of the blade in response to control inputs, but can also predict the effect that the airframe has on the flowfield. The main components of CHARM are: a full-span Constant Vorticity Contour (CVC) wake model, physics-based models used to predict the structure of the trailed "super-vortices," curved vortex elements with an analytical solution for the self-induced velocity effect, and the ability to incorporate fast hierarchical vortex methods.

3.2.1 The CVC Free Wake Model

The CVC model is comprised of both the trailed and shed vortex filaments, of equal and constant strength, from the full span of the rotor. So unlike the MFW code, the shed vortex filaments in the root and inboard portion of the blade are not truncated after some time. Also, the number of vortex filaments is determined by the user.

The CVC wake is divided into a primary circulation zone and a negative tip circulation zone if one is present. Similar to the MFW code, all the wake filaments are able to distort freely within the flowfield, and the filament positions are determined by integrating the Biot–Savart Law along each vortex filament. The initial vortex core radius is set to the average distance between filaments, which is typically about 1% of the blade radius. CDI claims that the use of curved vortex

filaments and fast vortex methods allow for a high fidelity wake solution with smaller CPU time compared to other full-span vortex lattice methods using straight line filaments because fewer curved filaments are required to fully characterize the rotor flow field.

3.2.2 Self-Induced Velocity Effect (SIVE) and Viscous Effects

CHARM has the option to use a refined vortex model that analytically determines the roll up of the vortices from the bound circulation distribution of the blade. It works, "by conserving circulation, vorticity centroid and the second moment of vorticity of the bound circulation distribution on a station-by-station basis as the vortex rolls up, the internal circulation profile of the vortex is known at all stages of the rollup process" (Ref. 35). The CHARM model also determines the induced velocity of a vortex element upon itself. This effect is important to model for analysis like hover performance. The vortex diffusion and filament straining methods documented in Ref. 35 are similar to those used in the MFW model.

Chapter 4

4 Results and Discussion

The following chapter is divided into four sections. The first section will detail the input file variable selection process and the results from that effort. Reasoning for each variable selection will be provided, and the effects encountered will be discussed. The second section will show what the effect of advance ratio has on the overall far rotor wake structure and strength. A comparison of the MFW predictions of the wake skew angle, and wake structure through the analysis of velocity field images, and the aperiodicity of the rotor far wake will be the primary focus of this section. How the baseline MFW configuration and wind tunnel test condition was chosen, and the results of that comparison, will also be mentioned. The third section of this chapter will go into further details on attempts to improve the correlation between the MFW and the wind tunnel results. This includes changing the wake growth parameter and various rotor parameters. The fourth and final section of this chapter will show how well the CHARM code compares to the wind tunnel results. Also in this section is a brief discussion on what CHARM input file parameters were changed and the reasons for changing them. A portion of the wind tunnel PIV figures and all of the MFW and CHARM velocity field images have an additional graph, located at the top of each figure, where the vertical in-plane velocity is plotted. On the lower half of each figure, there is a red and green line. They highlight where the right and left vortex is located vertically within the plane. The magnitude of the vertical velocity at the location highlighted by these two lines is shown in the graph located in the upper half of each figure. All PIV and velocity

field graphs have the same scale applied to the out-of-plane velocity to allow proper comparison between the various configurations.

4.1 Initial MFW setup and results

Upon completion of the NASA wind tunnel test and receipt of the MFW code, the effort to emulate the conditions observed in the wind tunnel began. As stated in Chapter 2, the NASA wind tunnel test was conducted using $1/48^{th}$ scale models. The tests documented in this thesis involved the H-53 model. The pertinent details of both test entries, the one supported by this author and the one undertaken shortly thereafter, are summarized in Table 4.1.

Table 4.1: NASA wind tunnel run summary.

Group	Run #	Acquisition #	Point #	Test Condition #	Target Full Scale V_∞ (kts)	C_T	RPM	ΩR (ft/sec)	V_∞ (ft/sec)	μ	x/R	Rationale
A	176	139	20	3D	20	0.00901	3054	263.21	11.636	0.044	1.1139	Variation with WOD speed
A	176	137	18	3B	20	0.00901	3064	264.03	11.652	0.044	2.1266	Variation with WOD speed
A	176	138	19	3C	20	0.00901	3061	263.76	11.561	0.044	3.6456	Variation with WOD speed
A	176	136	17	3A	20	0.00901	3056	263.38	11.71	0.044	6.6835	Variation with WOD speed
B	175	122	25	6	30	0.00674	3054	263.18	17.916	0.068	3.2279	Repeat of full scale flight test point
C	176	131	12	1B	30	0.00901	3059	263.57	17.396	0.066	1.1139	Variation with longitudinal distance
C	176	130	11	1A	30	0.00901	3056	263.33	17.448	0.066	2.1266	Variation with longitudinal distance
C	175	129	32	13	30	0.00901	3058	263.49	17.467	0.066	2.6398	Repeat of full scale flight test point
C	175	128	31	12	30	0.00901	3059	263.63	17.523	0.066	2.7459	Repeat of full scale flight test point
C	175	118	21	2	30	0.00901	3063	263.98	17.407	0.066	3.2279	Repeat of full scale flight test point
C	175	127	30	11	30	0.00901	3058	263.55	17.381	0.066	3.7099	Repeat of full scale flight test point
C	175	126	29	10	30	0.00901	3052	263.02	17.425	0.066	5.2981	Repeat of full scale flight test point
C	175	119	22	3	30	0.00901	3065	264.15	17.405	0.066	6.4937	Repeat of full scale flight test point
C	175	120	23	4	30	0.00901	3066	264.24	17.49	0.066	10.7342	Repeat of full scale flight test point
D	175	123	26	7	30	0.01089	3068	264.41	18.147	0.069	2.6398	Repeat of full scale flight test point
D	175	125	28	9	30	0.01089	3052	262.97	18.121	0.069	5.2981	Repeat of full scale flight test point
D	175	124	27	8	30	0.01089	3061	263.79	18.121	0.069	7.9563	Repeat of full scale flight test point
E	176	140	21	4A	30	0.01251	3063	263.92	17.351	0.066	1.1139	Variation with longitudinal distance
E	176	141	22	4B	30	0.01251	3053	263.07	17.362	0.066	2.1266	Variation with longitudinal distance
E	175	121	24	5	30	0.01251	3061	263.81	17.43	0.066	3.2279	53X max GW scenario on LHD
E	176	143	24	4D	30	0.01251	3058	263.54	17.461	0.066	3.6456	Variation with longitudinal distance
E	176	142	23	4C	30	0.01251	3055	263.23	17.415	0.066	6.6835	Variation with longitudinal distance
F	176	132	13	2A	45	0.00901	3058	263.55	26.157	0.099	1.1139	Variation with WOD speed
F	176	134	15	2C	45	0.00901	3063	263.93	26.212	0.099	2.1266	Variation with WOD speed
F	175	117	20	1	45	0.00901	3056	263.33	26.165	0.099	3.2279	Variation with WOD speed
F	176	135	16	2D	45	0.00901	3054	263.17	26.157	0.099	5.2658	Variation with WOD speed
F	176	133	14	2B	45	0.00901	3060	263.68	26.089	0.099	10.7342	Variation with WOD speed

The wind tunnel cases have been grouped by tunnel free stream velocity then by rotor thrust coefficient. The points gathered during Run 175 were the ones from the first tunnel entry in November 2005. These cases primarily focused on matching previously obtained full-scale data from the ship-based test effort conducted in

parallel to this wind tunnel testing, and is discussed in Chapter 1. The primary thrust coefficient from Run 175 corresponded to a gross weight of 61,000 lbs, which is the maximum mission representative gross weight of a CH-53E. The distances in Run 175, when converted to full scale, approximate the distances between the rotor hubs of an upwind CH-53E hovering directly over various LHA/LHD-class ship spots in front of an on-deck V-22. Points 30 and 31 from Run 175 were added to the matrix to investigate how the upwind helicopter's rotor wake changes over the rotors of a V-22. The downstream distance for Point 31 is one V-22 rotor radius shorter than Point 21 while Point 30 is one radius greater.

The points from Run 176 focused on quantifying what affect WOD (Groups A and F in Table 4) and thrust coefficient (Group E) had on the upwind helicopter's wake structure. Two points from that run, Points 11 and 12, were obtained to help tie in with previous test points from Run 175. At the time the analysis in support of this thesis began, the points from Run 176 had not been obtained. This left the WOD 30 kts and thrust coefficient equal to 0.00901 configuration as the only one with enough points to sufficiently validate the MFW code.

Once the appropriate flight condition had been selected, it became the basis of the four main MFW input files used to best simulate the wind tunnel tests. The four main input files are: flight.input, user.input, geometry.input, and rotprop.input. The flight.input file sets up the particular flight condition, defining such parameters as advance ratio, pitch/roll rates and the initial operating state of the rotor. The geometry.input file defines such aspects of the blade geometry as the number of blades, the radius, location of the flap hinge, chord length, twist and rotational

frequency. The rotprop.input file sets the blade mass and flapping hinge spring constant. The last file, user.input, sets the method used, whether it is relaxation or time-marching, sets the trim routine as well as the number of iterations that are to be performed, and how long the filaments are retained in the calculation before being truncated.

Issues arose immediately in the effort to match the wind tunnel parameters. For the flight.input file, advance ratio and rotor thrust were known from the wind tunnel test log, however all the initial rotor states were not. The initial collective angle was not recorded during the test. A rotary potentiometer controlling the collective servo was simply turned until the appropriate thrust, as measured by the model's sting balance, was obtained. Also the wind tunnel model did not have cyclic pitch control and lacked a flap hinge. Because the model rotors were also quite rigid, flapping was deemed negligible.

The parameters within the geometry.input file were easier to obtain with the exception of the flap hinge location. Due to the model rotor's geometry, an intial value of '–1.0' corresponding to a teetering rotor, was selected. Within the rotprop.input file the blade mass was known but the value of the flap hinge spring was not. An arbitrarily high value was therefore chosen.

For the final input file, user.input, a large number of iterations had to be chosen to ensure that the initial wake transient progressed outside the bounds of the solution before steady state data could be obtained. The low advance ratio of 0.0660 further exasperated this issue, requiring over 20 rotor turns worth of iterations. At the

set azimuthal resolution of 12 degrees, this meant over 100 iterations would be required before data could be used to compare with the wind tunnel results.

Further compounding the problem, was the location of the queried planes of interest. In Table 4.1, the downstream positions for the PIV point ranged from just over one rotor radius downstream from the rotor to over ten. Again, because of the low advance ratio of this condition, this necessitated the number of "free turns" of the wake to be large. The input files from the first believable wake structure are shown in Table 4.2.

Table 4.2: Input file variables for the first case with a believable wake structure.

flight.input

Paramter	Value
mu	0.15
muc	0.0
pbar	0.0
qbar	0.0
ct0	0.08989
t0_0	15.0
t1c0	0
t1s0	0
b0_0	0.1
b1c0	0
b1s0	0
cttol	0.002
fltol	1.0e-8
altitude	0.0

(a)

geometry.input

Paramter	Value
nr	1
nb	5
ns	32
asr0	0.0
rad	0.25083
flph	-1.0
rcout	0.324
crd	0.0282
twt	-10.65
om	320.77
taperst	1.0
taper	0.0
rotgeo	0

(b)

rotprop.input

Paramter	Value
bmass	0.08372
kbeta	1.0
betap	1.0

(c)

user.input

Paramter	Value
nw	1
pw	0
nfw	150
nk	1
ft	15
bct	0
dp	12
dz	12
rcb	0.05
dcy	0.0002
trm	y
lin	0.0
li	0.0
method	t
initial	b

(d)

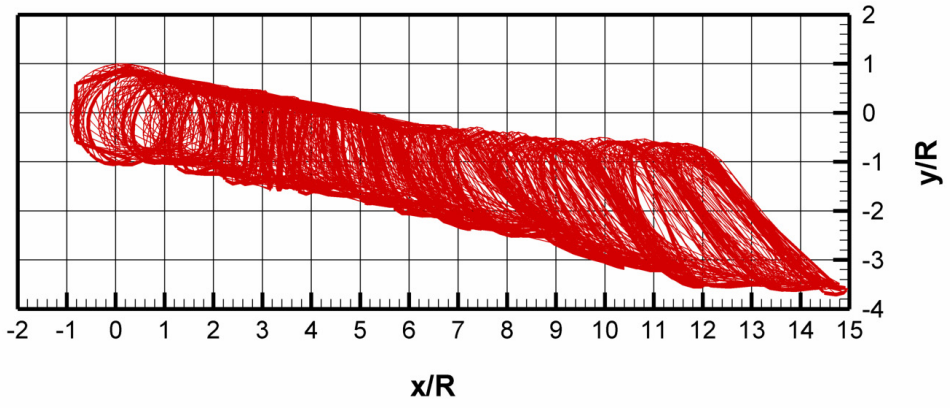

(a) Top View

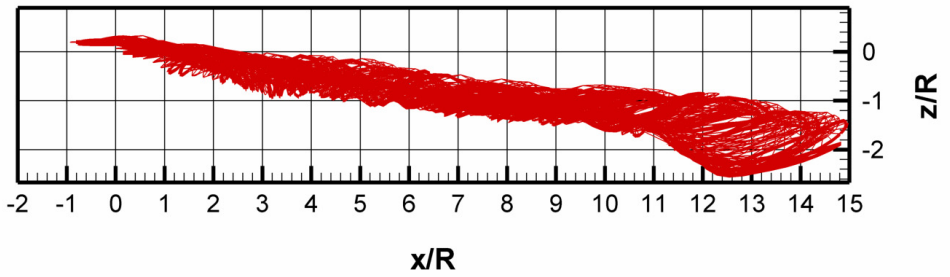

(b) Side View

Figure 4.1: Top and side wake geometry views for an advance ratio = 0.15.

With the encouraging results observed in Fig. 4.1, it was determined that the best way to get a usable solution at an advance ratio of 0.066 was to march down, in very small increments, from 0.15 to 0.066. The MFW code would be run at a given advance ratio, then the wake geometry output files would be used as the initial condition for the next case at a slightly lower advance ratio. The reasoning being that if the step down in advance ratio was small enough that the start-up transient would be small and wake geometries would be well behaved.

4.2 Effect of advance ratio on wake structure

The first cases generated were run on dated hardware, which resulted in cases taking six or more hours to solve, because of the high number of filaments retained and the large number of iterations required for each solution. As a result, the MFW code was run on more current hardware. The results are shown in Figs. 4.2 through 4.4.

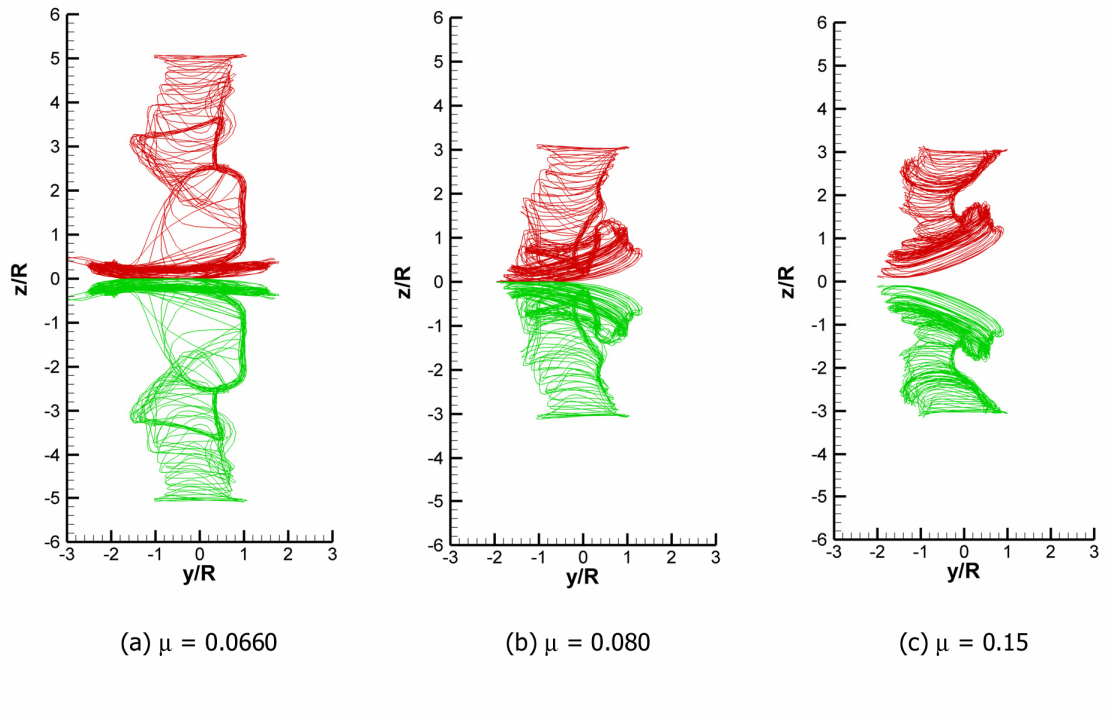

Figure 4.2: Rear view of the advisor generated wake geometries.

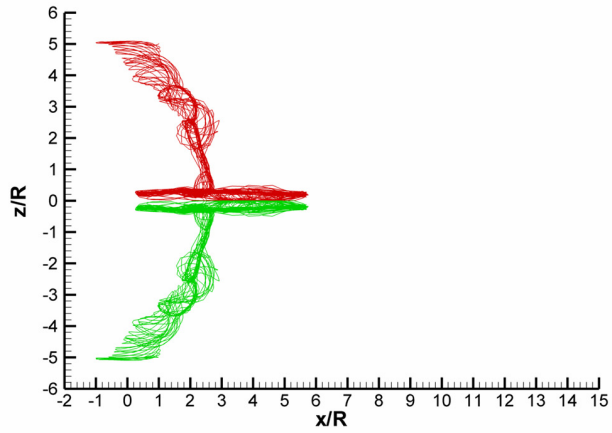

(a) μ = 0.0660

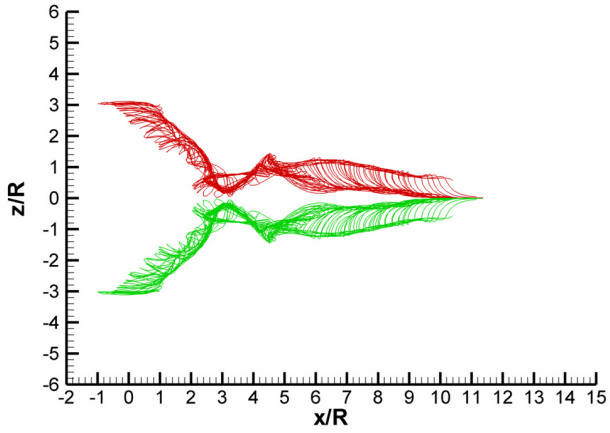

(b) μ = 0.080

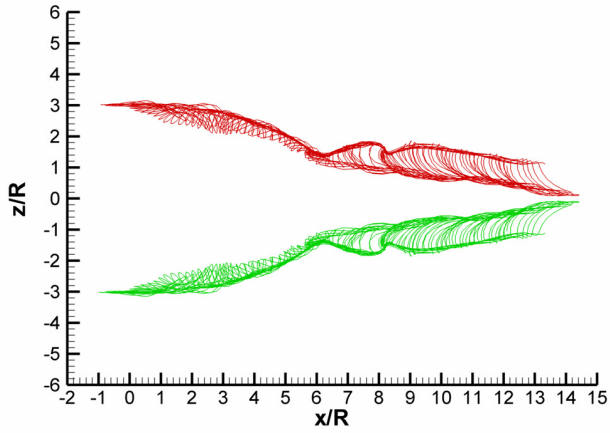

(c) μ = 0.15

Figure 4.3: Side view of the advisor generated wake geometries.

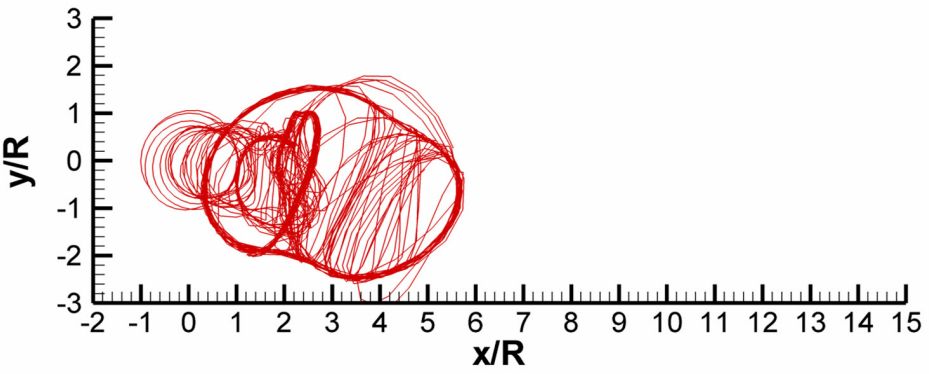

(a) μ = 0.0660

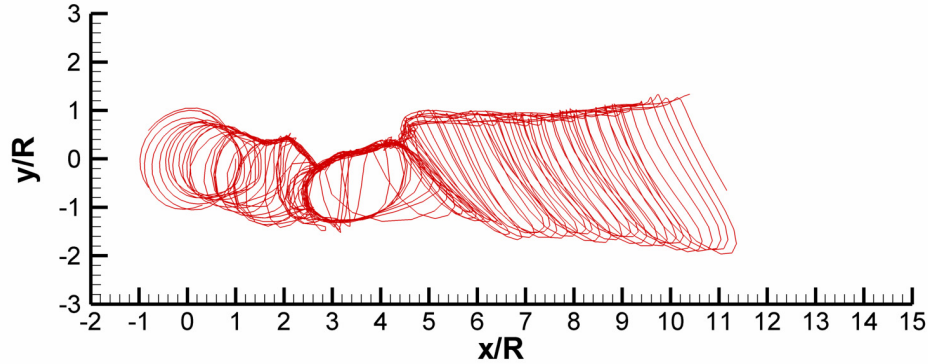

(b) μ = 0.080

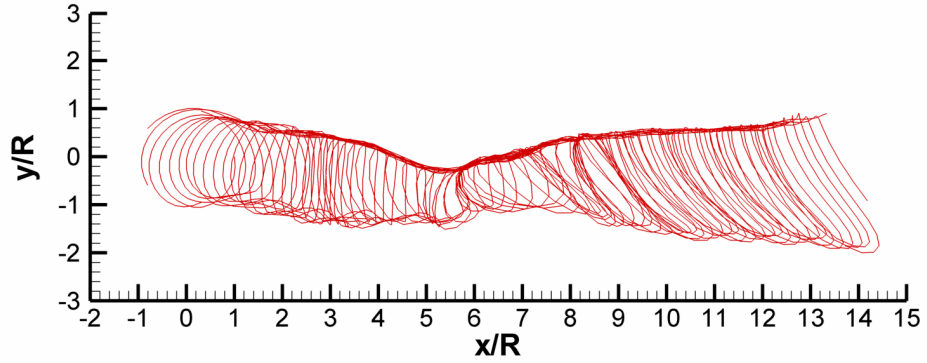

(c) μ = 0.15

Figure 4.4: Top view of the advisor generated wake geometries.

This version of MFW was set up to handle In Ground Effect (IGE) problems and as such had the mirrored wake seen in Fig. 4.2 and 4.3. The mirror wake was not shown in Fig. 4.4 for simplicity sake as it would not have added any additional information to the figure. The main point in Figs. 4.2 and 4.3 is that for an advance ratio of 0.066, the MFW code predicts an approximately 45 deg wake skew angle for some vortex age then the skew angle decreases resulting in the wake almost becoming vertical. The same happens for an advance ratio of 0.08 as seen in Fig. 4.3(b). The wake impacts the ground plane approximately three rotor radii downstream of the rotor hub which itself was three rotor radii from the ground plane. Even for the highest advance ratio of 0.15, the solution could no longer be considered an Out of Ground Effect (OGE) problem much past six rotor radii downstream.

Such results required in an immediate review of the gathered NASA wind tunnel data, which at that time only consisted of the runs obtained at an advance ratio of 0.066 from Run 175. The individual Group C PIV images taken at the positions outlined in Table 4.1 are shown in Figs. 4.5 through 4.13 and summarized in Figs. 4.14 through 4.16. The distances have been non-dimensionalized by dividing them by rotor radius and the in-plane and out-of-plane velocities have been divided by tip speed. The black bar, with its center at (0,0) and a radius of one rotor radii, is a graphical representation of the model rotor.

There are quite a few interesting things to note about the wind tunnel PIV images. First, the wake geometry asymmetry between the left and right sides of the rotor disk is clear. This is because of the model rotor's inability to flap, and its lack of cyclic controls. These two factors combine to create a significant lift asymmetry

across the disk; the advancing side of the rotor disk generates greater lift than the retreating side. Because vortex structure and position are driven by the lift generated by the blade, the advancing side vortex convects farther down than the vortex trailed from the retreating side, and has a net core structure with the out-of-plane velocities being slower than free-stream, as seen in Figs. 4.9 through 4.12. As Fig. 4.16 shows, for an advance ratio of 0.066 the wake skew angle is much greater than that shown in Fig. 4.3(a). It is important to note though that the wake geometries depicted in Figs. 4.2 through 4.4 are from a single iteration time step from the MFW code while the wind tunnel images presented in Figs. 4.5 through 4.16 are phase averaged over 25 seconds. The aperiodicity of the wake in the wind tunnel test and that predicted by the MFW code will be further discussed later on in this chapter. In the wind tunnel test, as Fig. 4.16 shows, the vortices have only moved two rotor radii downward at over ten rotor radii downstream of the rotor.

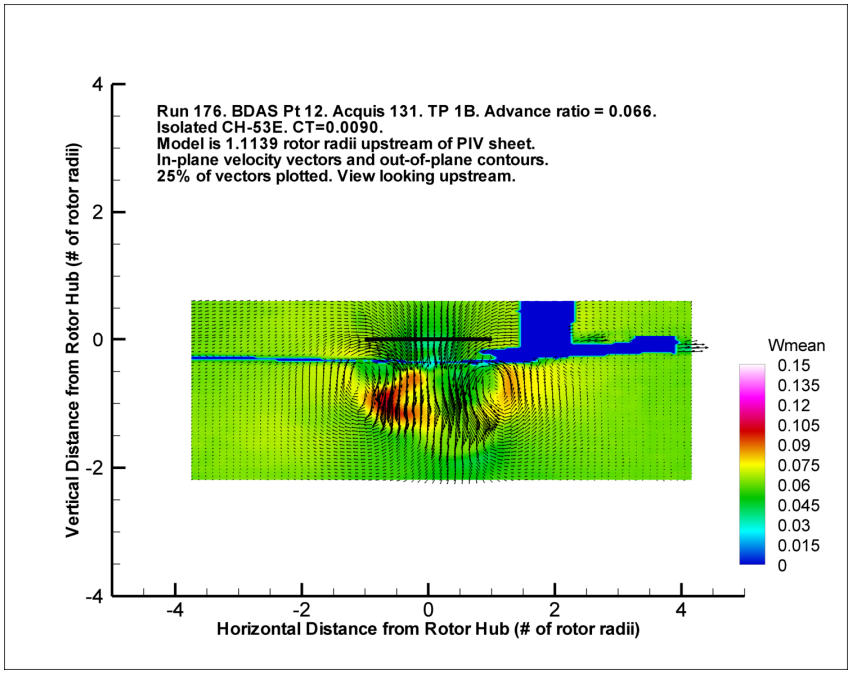

Figure 4.5: NASA PIV Image. Thrust coefficient = 0.009. Advance ratio = 0.066. PIV image captured 1.1139 rotor radii downstream of the rotor.

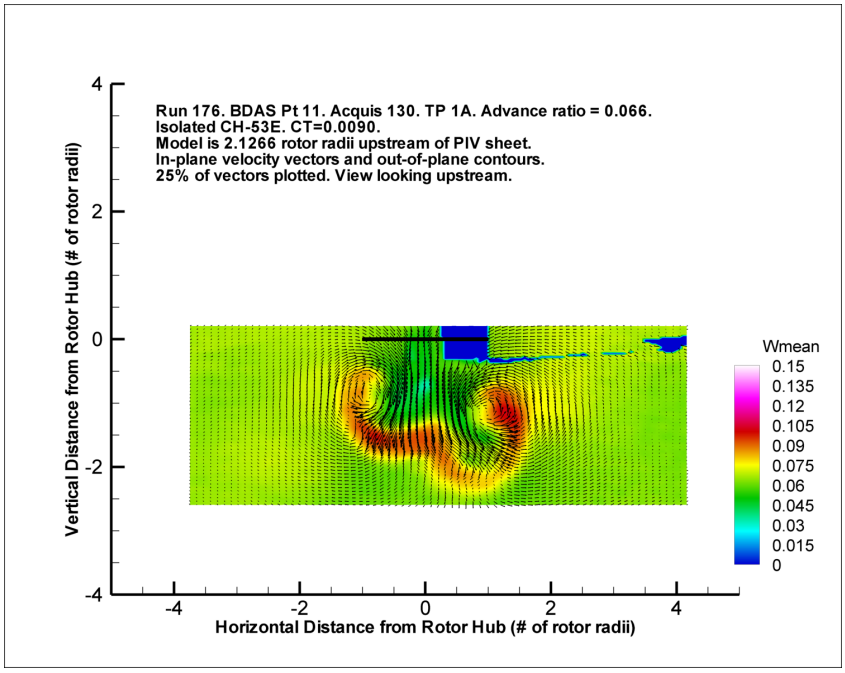

Figure 4.6: NASA PIV Image. Thrust coefficient = 0.009. Advance ratio = 0.066. PIV image captured 2.1266 rotor radii downstream of the rotor.

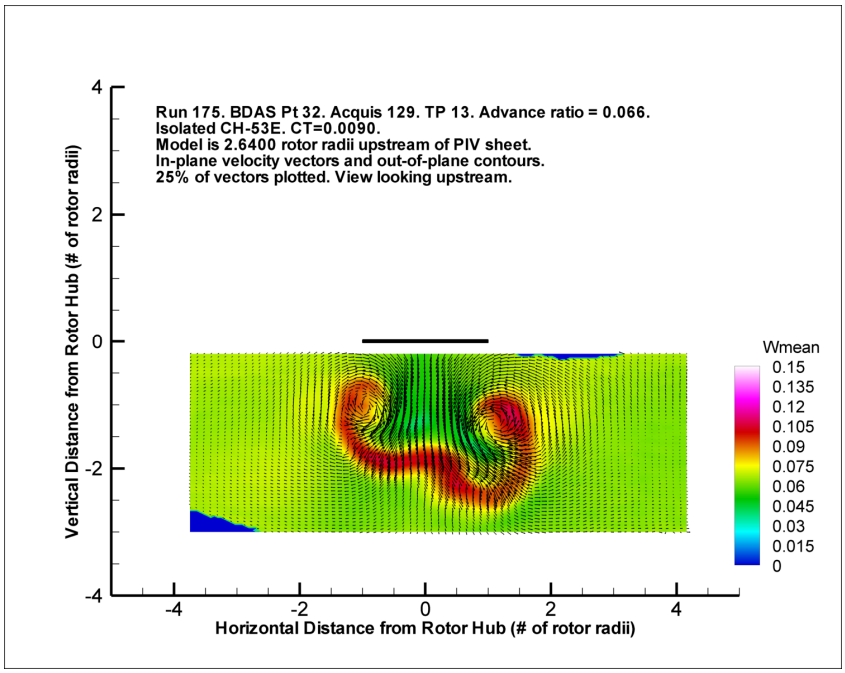

Figure 4.7: NASA PIV Image. Thrust coefficient = 0.009. Advance ratio = 0.066. PIV image captured 2.6400 rotor radii downstream of the rotor.

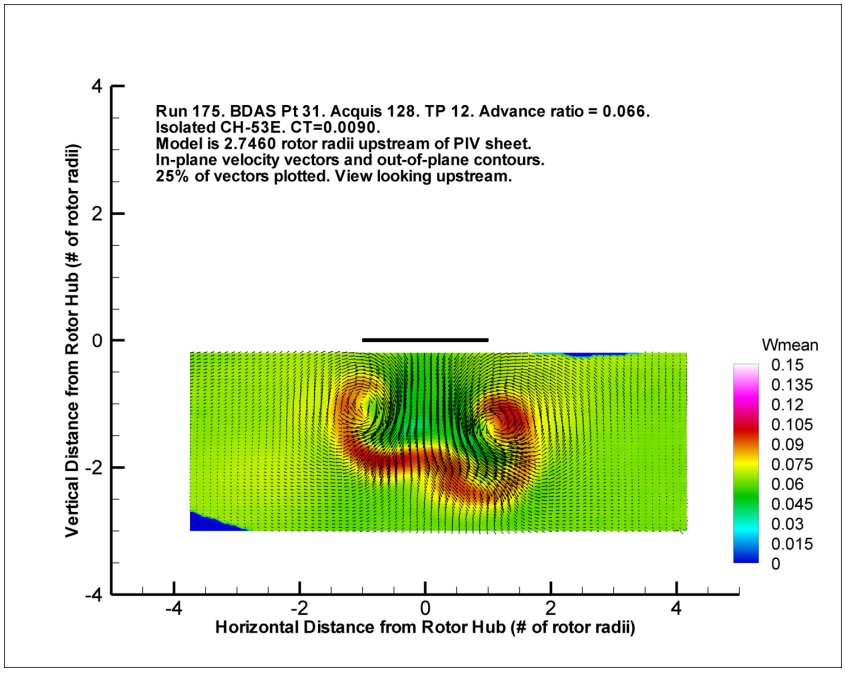

Figure 4.8: NASA PIV Image. Thrust coefficient = 0.009. Advance ratio = 0.066. PIV image captured 2.746 rotor radii downstream of the rotor.

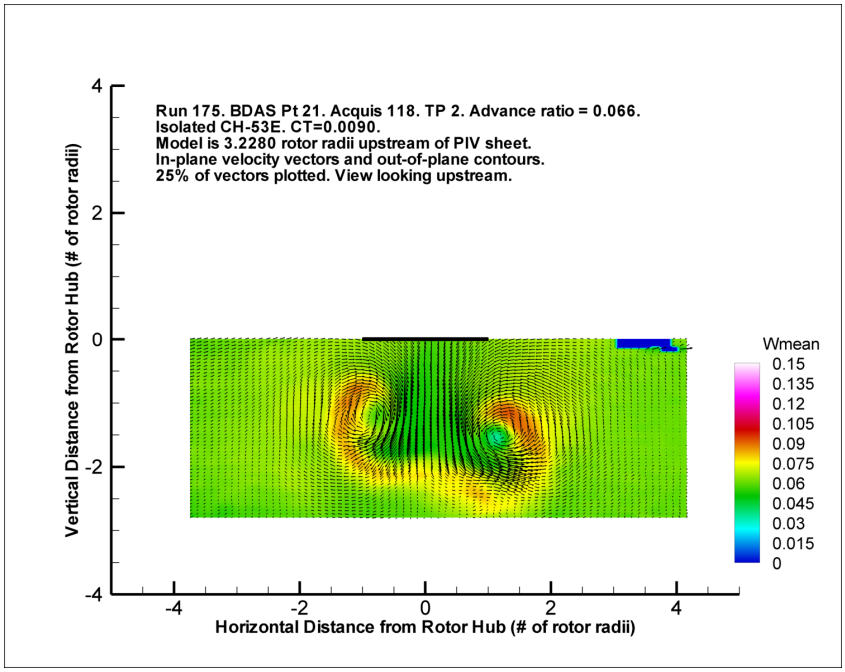

Figure 4.9: NASA PIV Image. Thrust coefficient = 0.009. Advance ratio = 0.066. PIV image captured 3.2280 rotor radii downstream of the rotor.

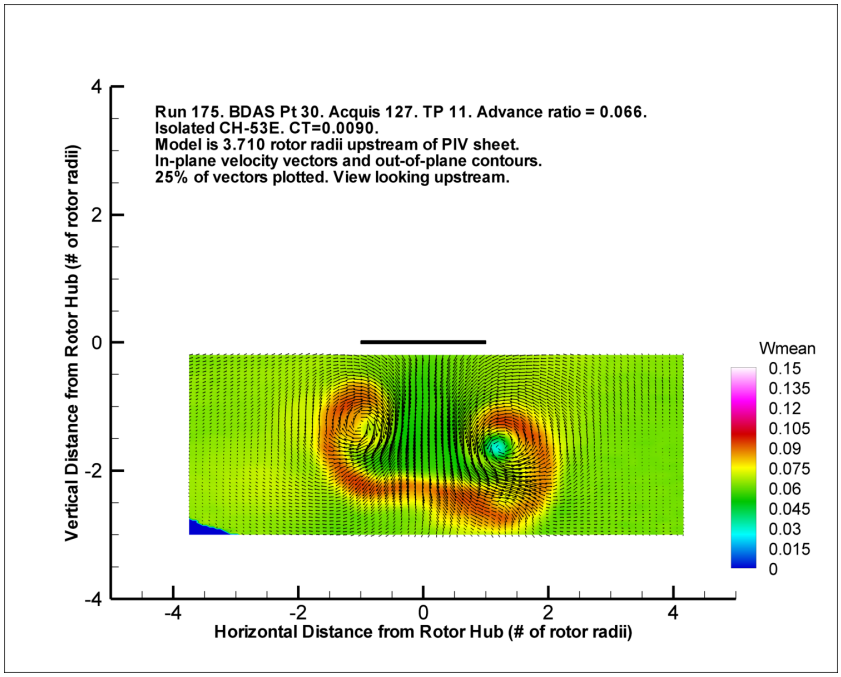

Figure 4.10: NASA PIV Image. Thrust coefficient = 0.009. Advance ratio = 0.066. PIV image captured 3.710 rotor radii downstream of the rotor.

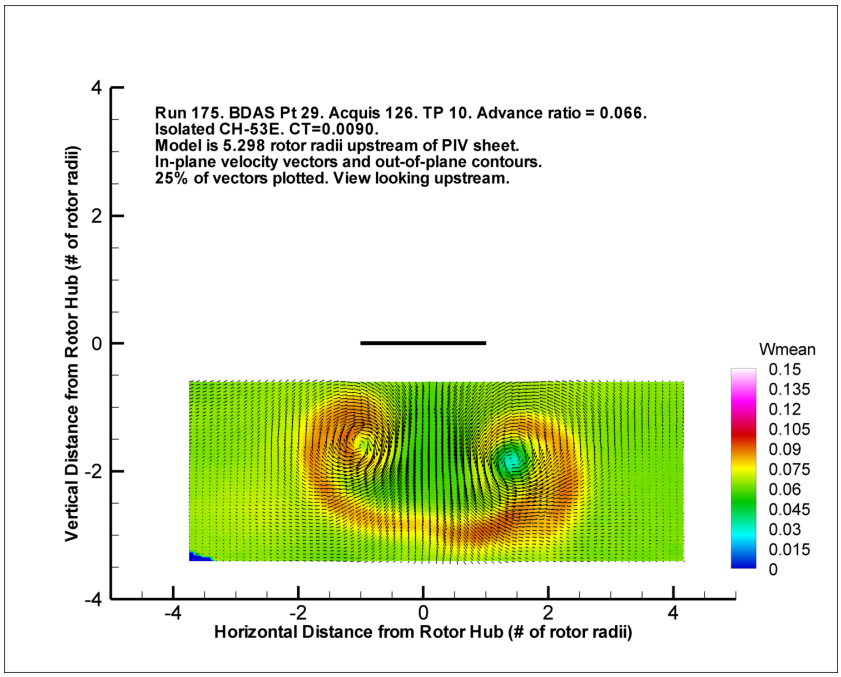

Figure 4.11: NASA PIV Image. Thrust coefficient = 0.009. Advance ratio = 0.066. PIV image captured 5.298 rotor radii downstream of the rotor.

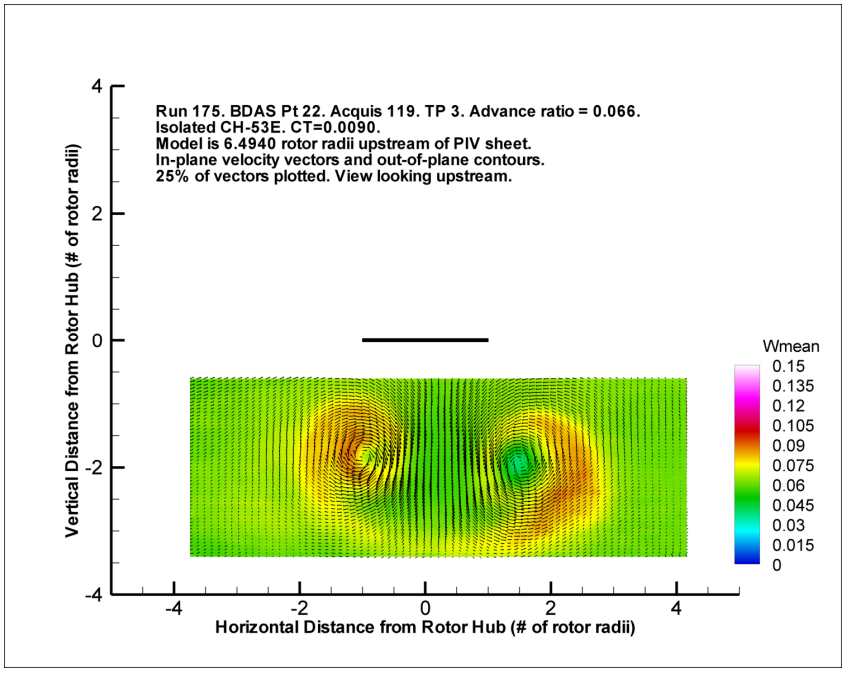

Figure 4.12: NASA PIV Image. Thrust coefficient = 0.009. Advance ratio = 0.066. PIV image captured 6.494 rotor radii downstream of the rotor.

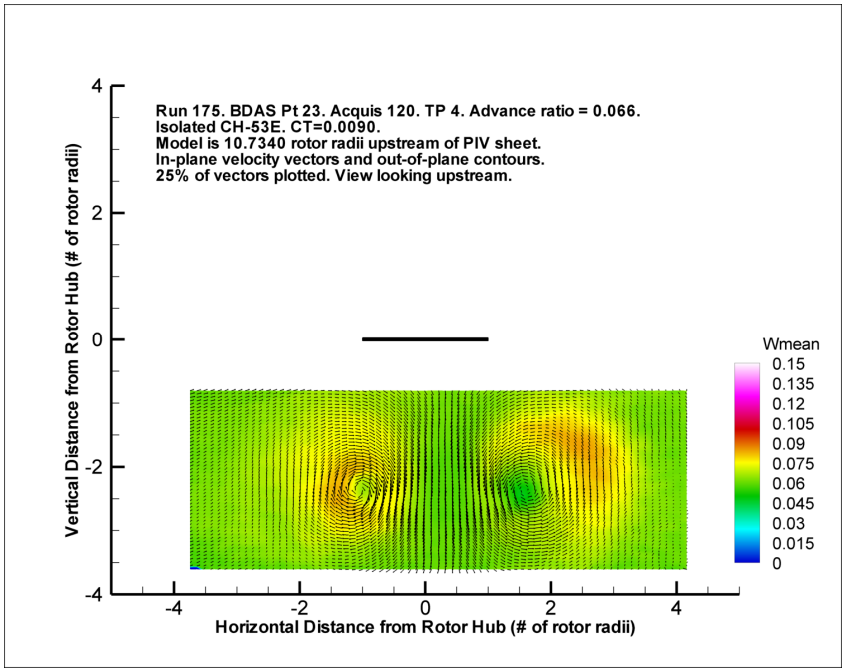

Figure 4.13: NASA PIV Image. Thrust coefficient = 0.009. Advance ratio = 0.066. PIV image captured 10.734 rotor radii downstream of the rotor.

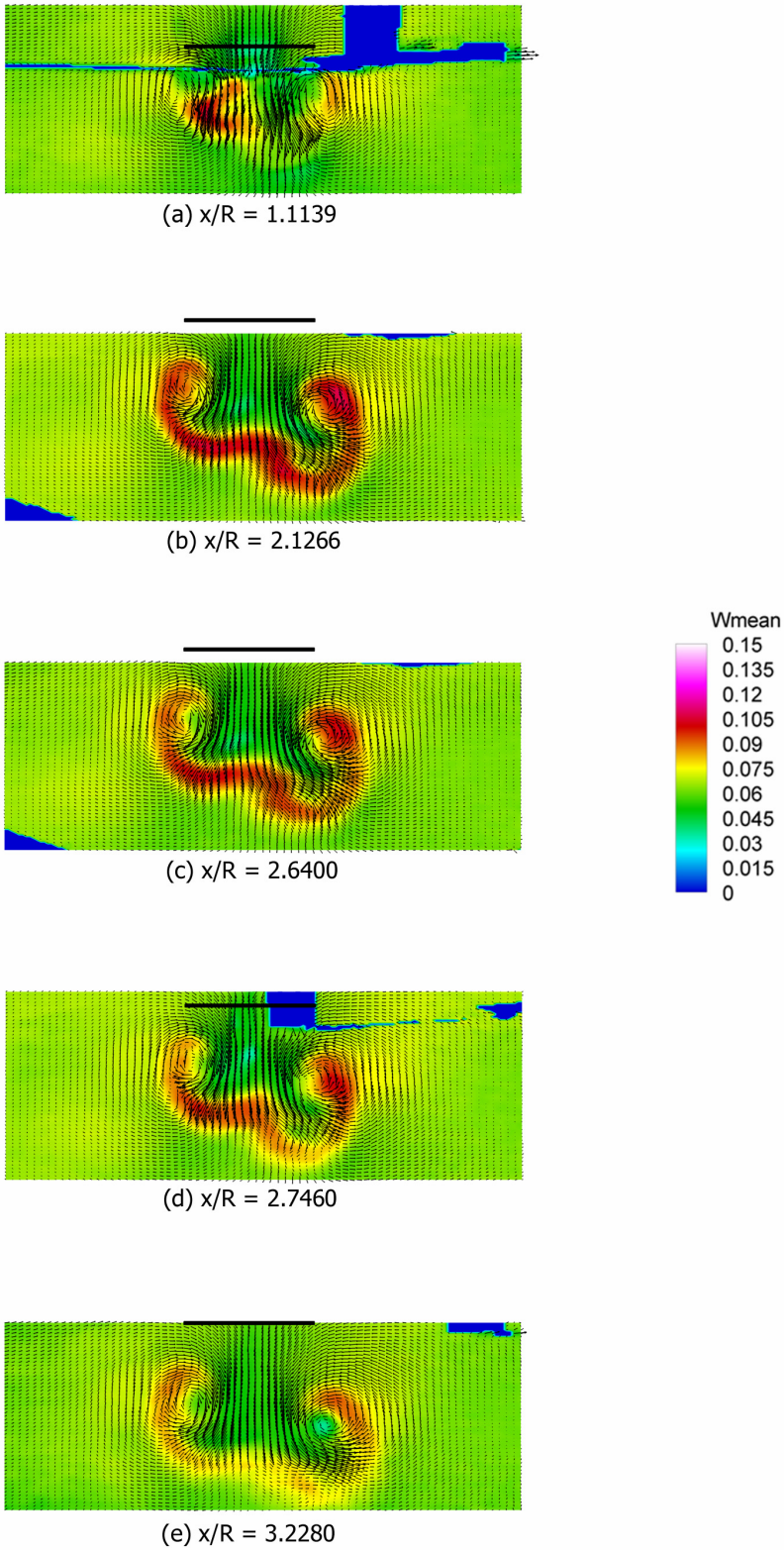

Figure 4.14: NASA PIV Images. Thrust coefficient = 0.009. Advance ratio = 0.066. PIV images captured 1.1139 – 3.2280 rotor radii downstream of the rotor.

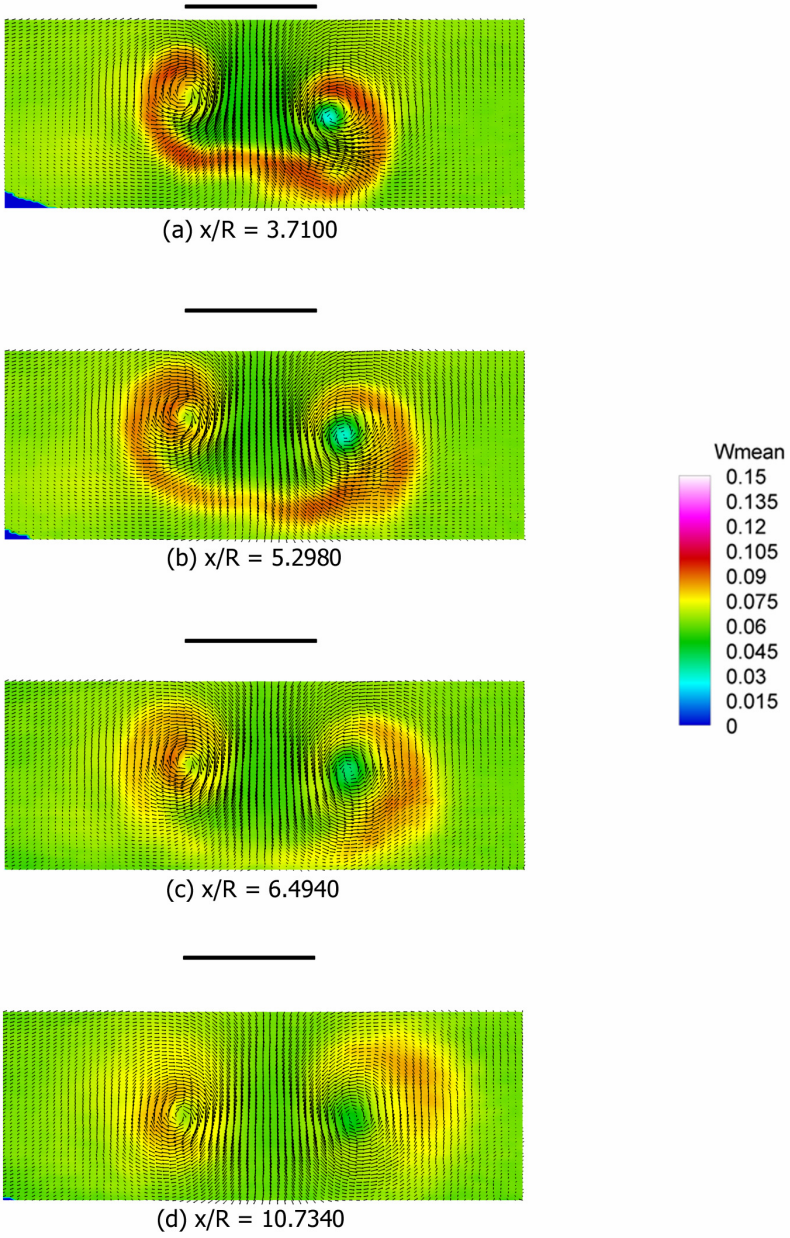

Figure 4.15: NASA PIV Images. Thrust coefficient = 0.009. Advance ratio = 0.066. PIV images captured 3.640 – 10.7340 rotor radii downstream of the rotor.

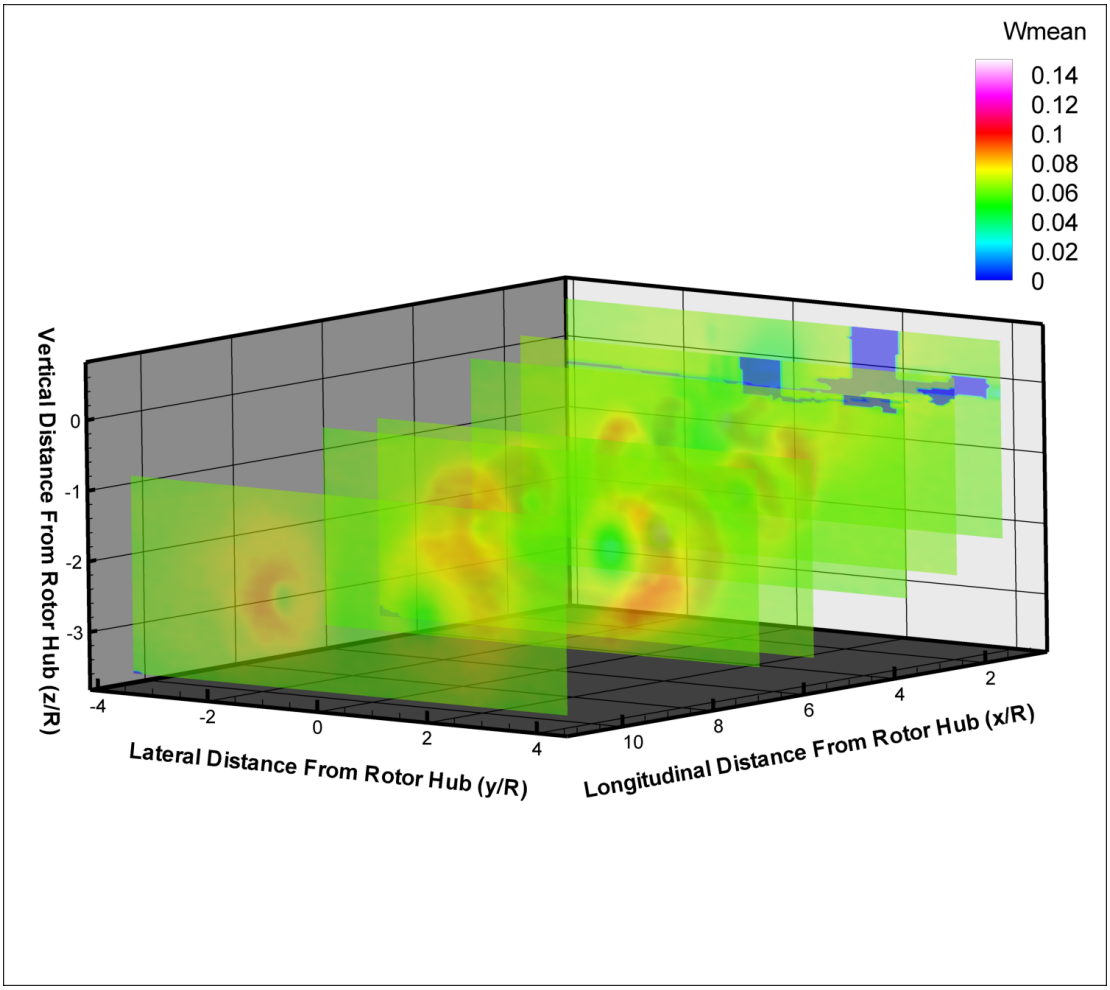

Figure 4.16: Isometric view of the NASA Wind Tunnel PIV images accurately placed in space to help visualize the rotor wake structure.

A verification effort was undertaken with a different version of the MFW code halfway through the validation effort due to the results from MFW not agreeing with the wind tunnel results. Using the input files provided with this different version of the MFW code, a successful verification effort was accomplished. The wake structure for the full-scale H-60 verification test case looked much more periodic than the results obtained so far trying to match the sub-scale wind tunnel tests that a quick case was run with a greater iteration number and increasing the value of the variable that controlled how many turns of the rotor filaments were kept before being

discarded. The exact variable values are depicted in Table 4.4 and the wake geometry images can be seen in Figs. 4.17 and 4.18. The particular iteration numbers were picked for specific reasons. Figures 4.17(a) and Fig. 4.18(a) show that this condition was started from a prescribed wake solution. Figs. 4.17(b) and 4.18(b) show the initialization transient half-way through the wake while Figs. 4.17(c) and 4.18(c) show it just prior to leaving the wake solution. In both cases, the wake upstream contracts in response to the transient. This tighter bundled section of the wake, as it ages, becomes more and more aperiodic. For the full-scale case shown in Figs. 4.17 and 4.18, this phenomenon damps out and a quasi-steady state solution is reached by the 160th iteration (Figs. 4.17(d) and 4.18(d)).

Table 4.3: Input file variables for the full-scale H-60 investigation.

flight.input	
Paramter	Value
mu	0.100
muc	0.0
pbar	0.0
qbar	0.0
ct0	0.00566
t0_0	14.00
t1c0	0
t1s0	0
b0_0	2.754
b1c0	0
b1s0	0
cttol	1.0e-8
fltol	1.0e-8
altitude	0.0

(a)

geometry.input	
Paramter	Value
nr	1
nb	4
ns	32
asr0	3.0
rad	8.18
flph	0.046
rcout	0.046
crd	0.5340
twt	-16.0
om	27.0
taperst	1.10
taper	0.0
rotgeo	0

(b)

rotprop.input	
Paramter	Value
bmass	14.19
kbeta	0.0
betap	0.0

(c)

user.input	
Paramter	Value
nw	1
pw	0
nfw	160
nk	1
ft	6
bct	2
dp	10
dz	10
rcb	0.05
dcy	0.0002
trm	y
lin	0.0
li	0.0
method	t
initial	n

(d)

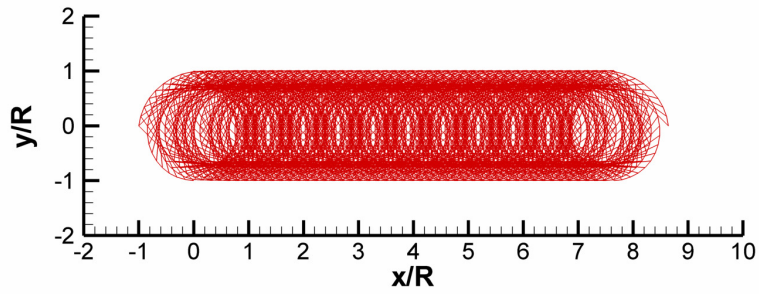

(a) Iteration = 0

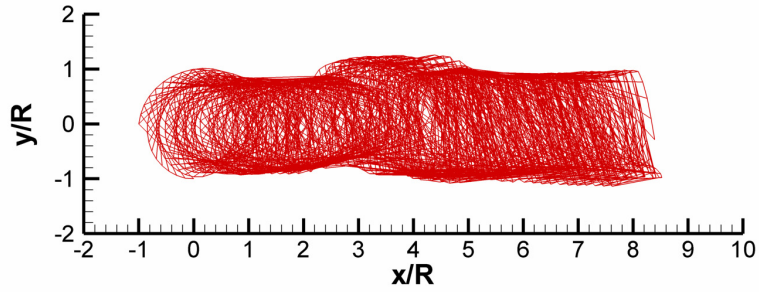

(b) Iteration = 28

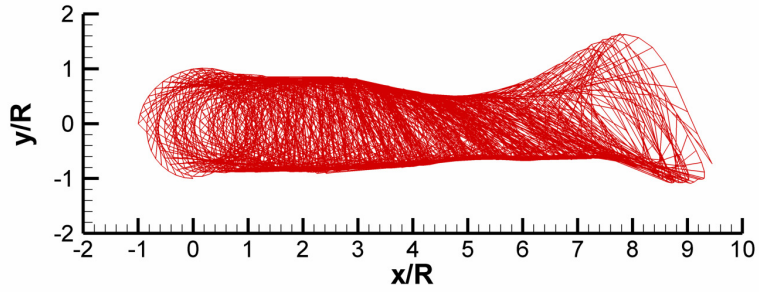

(c) Iteration = 65

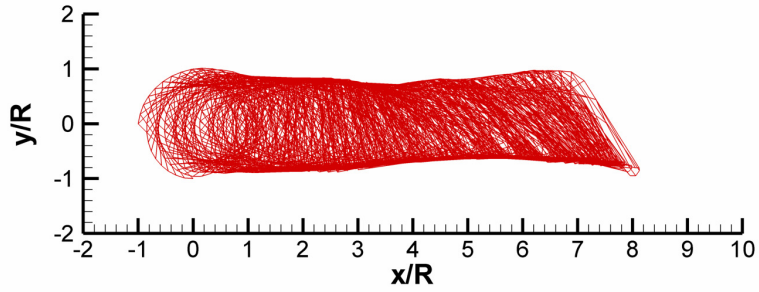

(d) Iteration = 160

Figure 4.17: Top view of MFW code generated wake geometry images for a full-scale H-60 at an advance ratio of 0.1

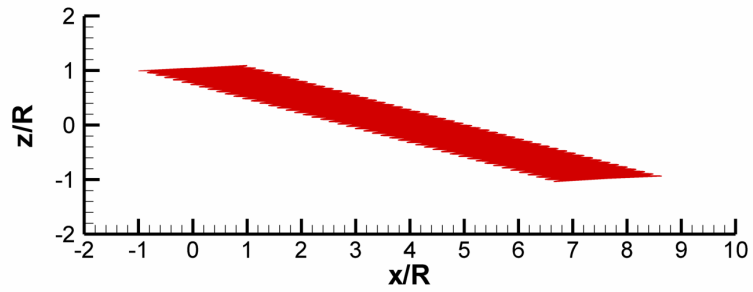

(a) Iteration = 0

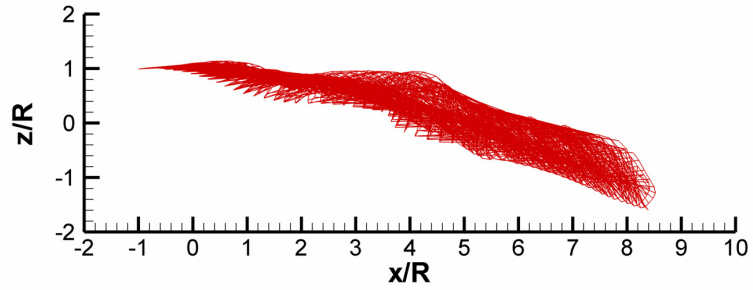

(b) Iteration = 28

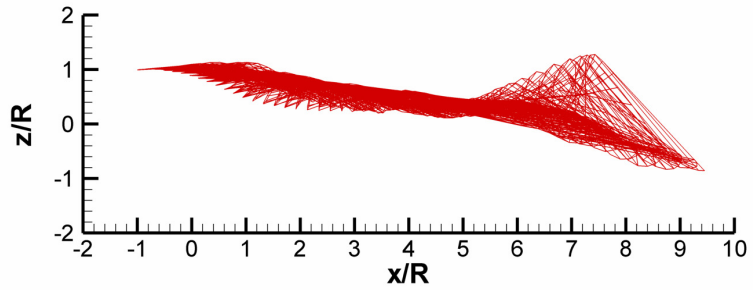

(c) Iteration = 65

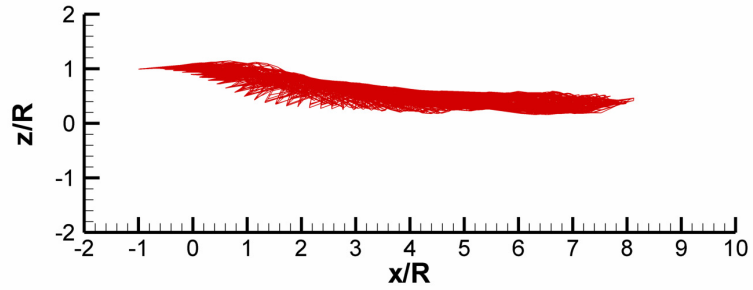

(d) Iteration = 160

Figure 4.18: Side view of MFW code generated wake geometry images for a full-scale H-60 at an advance ratio of 0.1

Encouraged by the results obtained from the full-scale H-60 investigation, another look at the two advance ratios tested in Run 175 (0.0660 and 0.0997) was undertaken. The input variable values are shown in Table 4.5 for the 0.0660 advance ratio case and in Table 4.6 for the 0.0997 advance ratio case. The wake geometry images are shown in Figs. 4.19 through 4.22.

Table 4.4: Input file variable values for an advance ratio = 0.0660 run.

flight.input	
Paramter	Value
mu	0.0660
muc	0.0
pbar	0.0
qbar	0.0
ct0	0.00901
t0_0	15.0
t1c0	0
t1s0	0
b0_0	0.10
b1c0	0
b1s0	0
cttol	1.0e-8
fltol	1.0e-8
altitude	0.0

(a)

geometry.input	
Paramter	Value
nr	1
nb	5
ns	32
asr0	0.0
rad	0.25083
flph	-1.0
rcout	0.324
crd	0.02819
twt	-10.65
om	320.77
taperst	1.0
taper	0.0
rotgeo	0

(b)

rotprop.input	
Paramter	Value
bmass	0.8373
kbeta	1.0
betap	1.0

(c)

user.input	
Paramter	Value
nw	1
pw	0
nfw	300
nk	1
ft	10
bct	2
dp	12
dz	12
rcb	0.05
dcy	0.0002
trm	y
lin	0.0
li	0.0
method	t
initial	n

(d)

Table 4.5: Table 8: Input file variable values for an advance ratio = 0.0997 run.

flight.input	
Paramter	Value
mu	0.09970
muc	0.0
pbar	0.0
qbar	0.0
ct0	0.00901
t0_0	15.0
t1c0	0
t1s0	0
b0_0	0.10
b1c0	0
b1s0	0
cttol	1.0e-8
fltol	1.0e-8
altitude	0.0

(a)

geometry.input	
Paramter	Value
nr	1
nb	5
ns	32
asr0	0.0
rad	0.25083
flph	-1.0
rcout	0.324
crd	0.02819
twt	-10.65
om	320.77
taperst	1.0
taper	0.0
rotgeo	0

(b)

rotprop.input	
Paramter	Value
bmass	0.08372
kbeta	1.0
betap	1.0

(c)

user.input	
Paramter	Value
nw	1
pw	0
nfw	175
nk	1
ft	4
bct	2
dp	12
dz	12
rcb	0.05
dcy	0.0002
trm	y
lin	0.0
li	0.0
method	t
initial	n

(d)

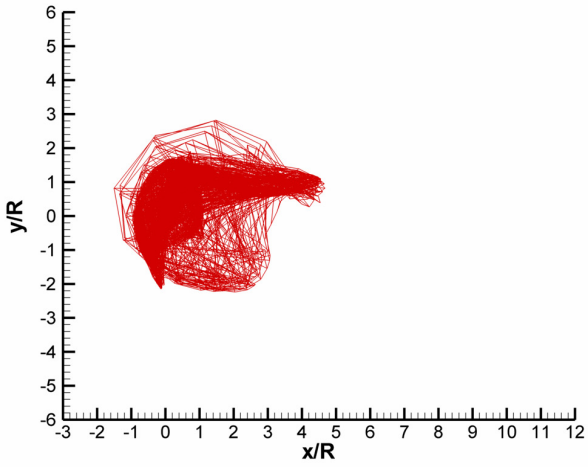

(a) Iteration = 200

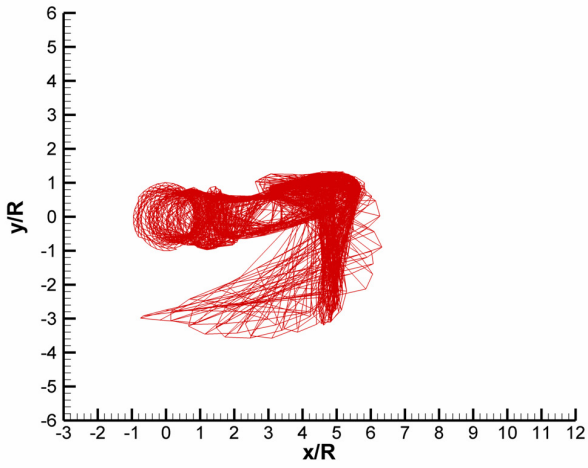

(b) Iteration = 250

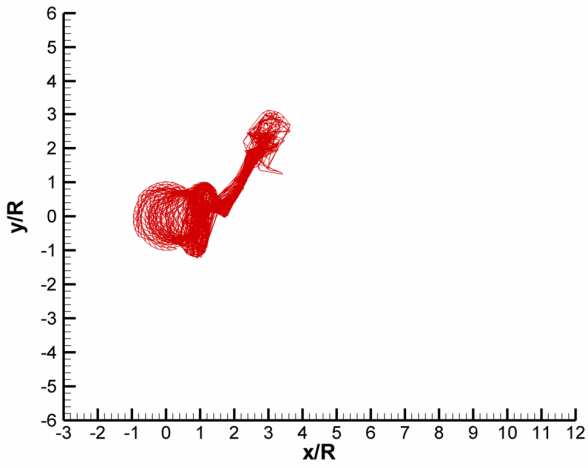

(c) Iteration = 300

Figure 4.19: Top view of MFW generated wake geometry images for an advance ratio = 0.066.

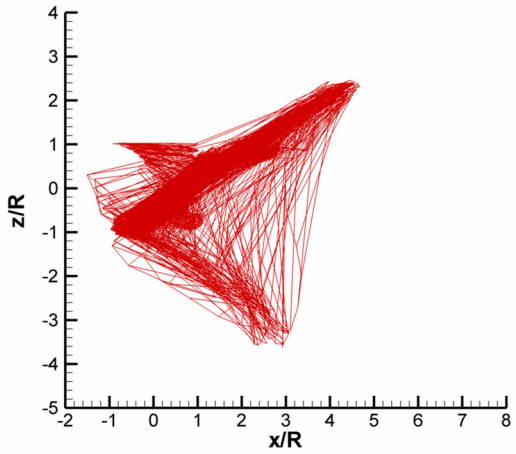

(a) Iteration = 200

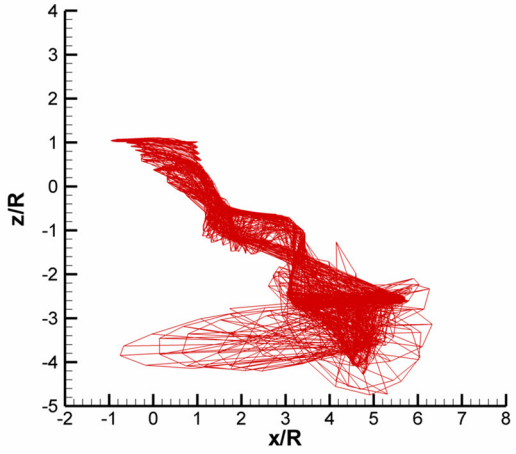

(b) Iteration = 250

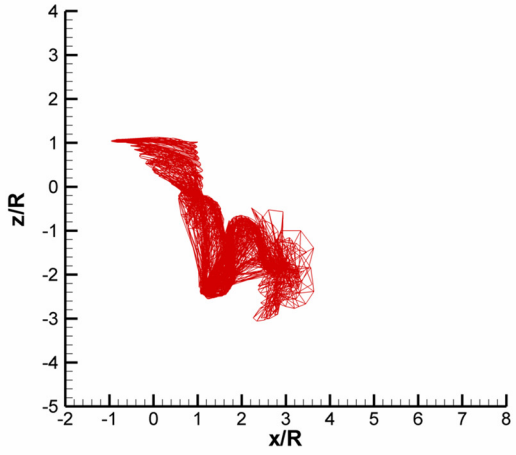

(c) Iteration = 300

Figure 4.20: Side view of MFW generated wake geometry images for an advance ratio = 0.066.

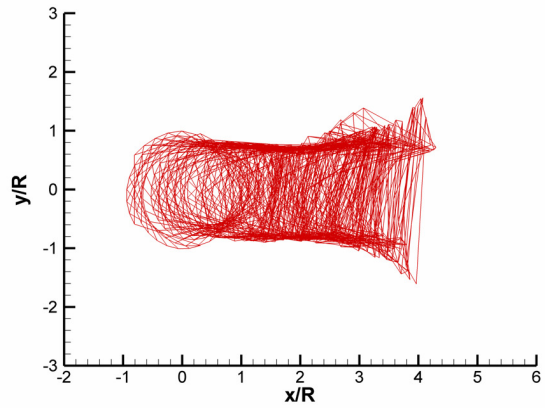

(a) Iteration = 145

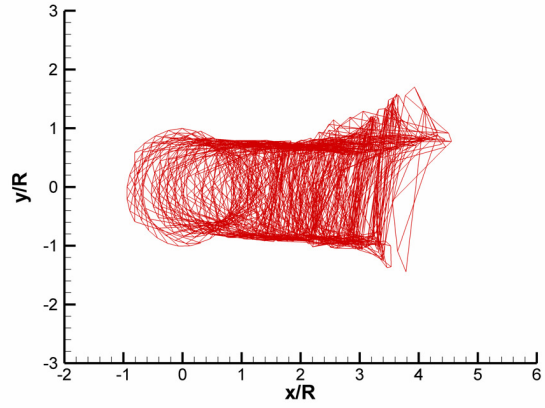

(b) Iteration = 165

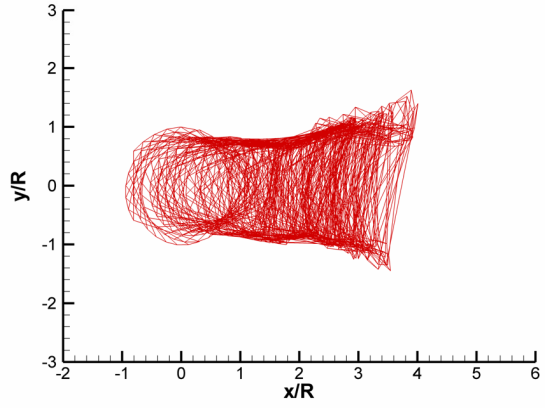

(c) Iteration = 175

Figure 4.21: Top view of MFW generated wake geometry images for an advance ratio = 0.0997.

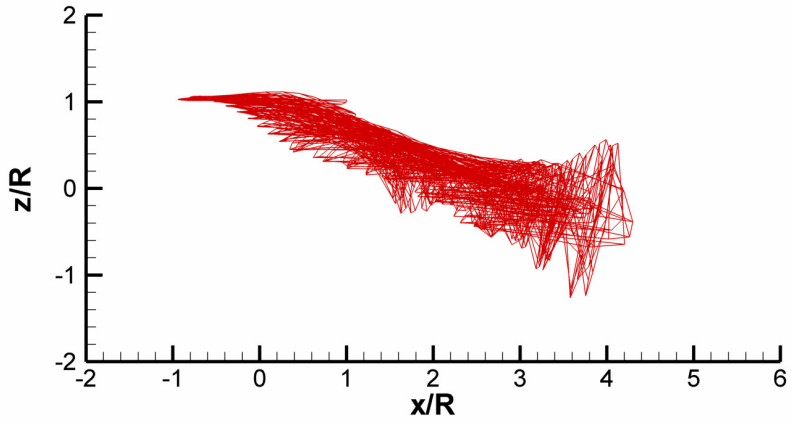

(a) Iteration = 145

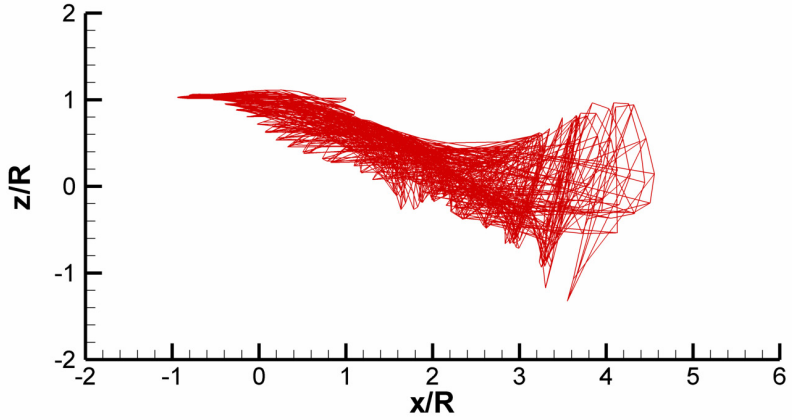

(b) Iteration = 165

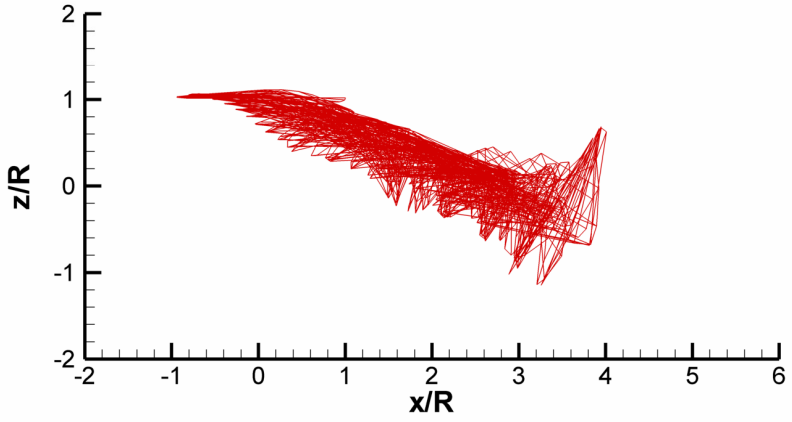

(c) Iteration = 175

Figure 4.22: Side view of MFW generated wake geometry images for an advance ratio = 0.0997.

The effort met with limited success. As seen in Figs. 4.19 and 4.20, there exists great wake aperiodicity regardless of what iteration number is examined. The wake exhibits some of the same tendencies as observed for the full-scale H-60 test case however for this particular case those tendencies do not damp out. The wake appears to exhibit a sort of an aperiodicity at a sub-harmonic of the rotor frequency. Instabilities in the far wake do not seem to diffuse, but in fact seem to strengthen as those portions of the wake age. These areas of tightly bundled vortex filaments interact with each other and adversely affect the wake geometry upstream.

There are periods of relatively quiescent wake activity, however. As the last of the far wake instability is convected out of the solution the wake is relatively behaved for the first few rotor radii as seen in Figs. 4.19(b) and 4.20(b), compared to the other two iteration steps plotted in Figs. 4.19 and 4.20. However as the instability leaves, it contracts the wake upstream, forcing the filaments closer together and as these new groups of filaments age, their self-induced effects do not dissipate, causing more wake aperiodicity, and the wake once again exhibits some very interesting behavior, as seen in Figs. 4.19(c) and 4.20(c). If the filaments are not given the time to exhibit aperiodic tendencies and adversely affect the flow upstream, a much more believable wake structure is obtained and is shown in Figs. 4.21 and 4.22. The number of rotor turns before filaments are discarded is relatively low and the advance ratio is higher than that from Figs. 4.19 and 4.20. These two factors combined keep the wake from going aperiodic to the degree seen in the case at an advance ratio of 0.066. In fact, there is relatively no difference in the various iteration time steps presented in Figs. 4.21 and 4.22.

After obtaining a well behaved wake solution for the advance ratio = 0.0997 case, an attempt was made to generate some velocity field images from the wake geometry files to match those obtained from the NASA wind tunnel test. The last 30 iteration steps were averaged to obtain the velocity field images as seen in Figs. 4.23 and 4.24. The velocity field images show two clear vortices, with the out-of-plane velocities within the vortex cores being very high. For Fig. 4.23, the non-dimensional velocities (essentially λ), were 0.19 while for Fig. 4.24 they were 0.188. The reason the contour scales were not adjusted was a λ of 0.15 was the highest value observed in all 27 NASA WT test cases. If the range were increased to encompass the large MFW predicted out-of-plane velocities, detail of this component of velocity would be lost.

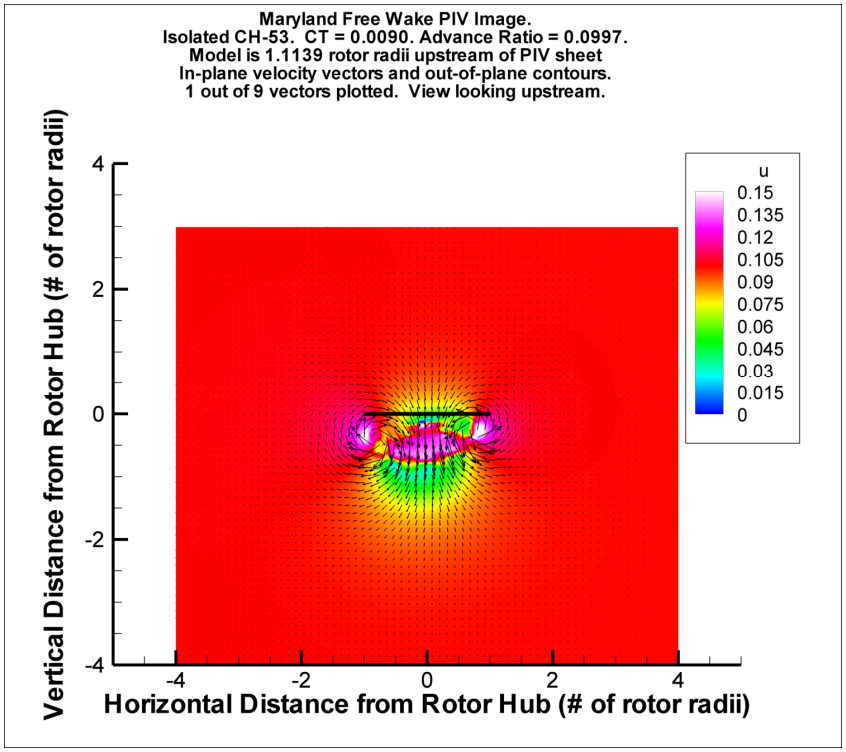

Figure 4.23: MFW PIV image. Model is 1.1139 rotor radii upstream of plane. Advance ratio is 0.0997.

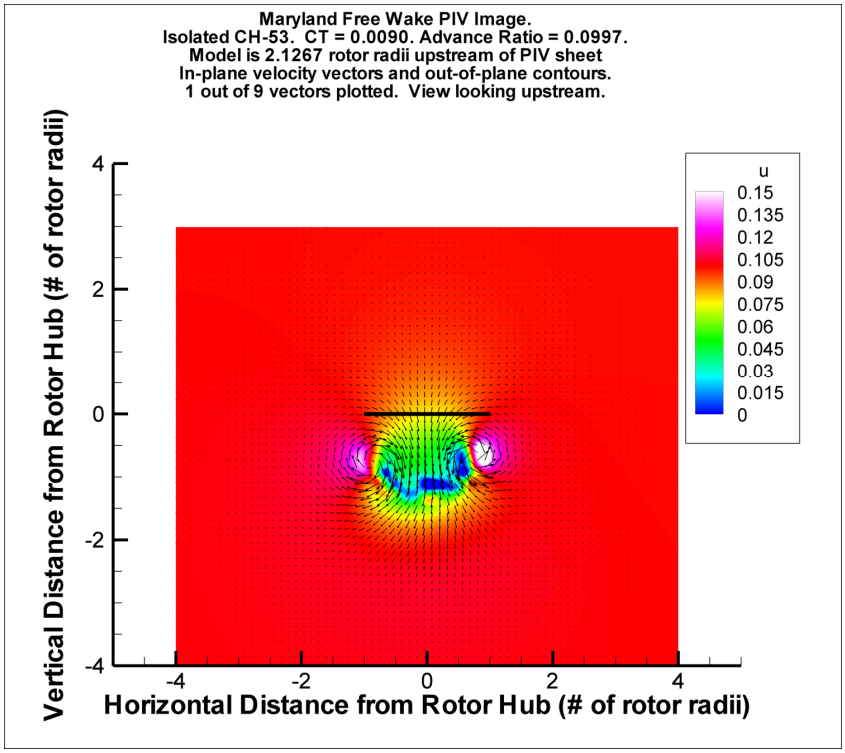

Figure 4.24: MFW PIV image. Model is 2.1267 rotor radii upstream of plane. Advance ratio is 0.0997.

In fact, the out-of-plane velocities in Fig. 43 have a minimum of minus 0.035, implying that the flow has actually reversed direction in the area between the two vortices. Because these two velocity field images were obtained for an advance ratio of 0.0997, the corresponding NASA wind tunnel images must now be discussed as well. Figures 4.25 through 4.29 show the individual phase-averaged PIV images obtained from both Run 175 and 176 of the NASA wind tunnel test. As was done for the Group C images, the full-scale equivalent 45 kts, Group F images are summarized in Figs. 4.30 and 4.31.

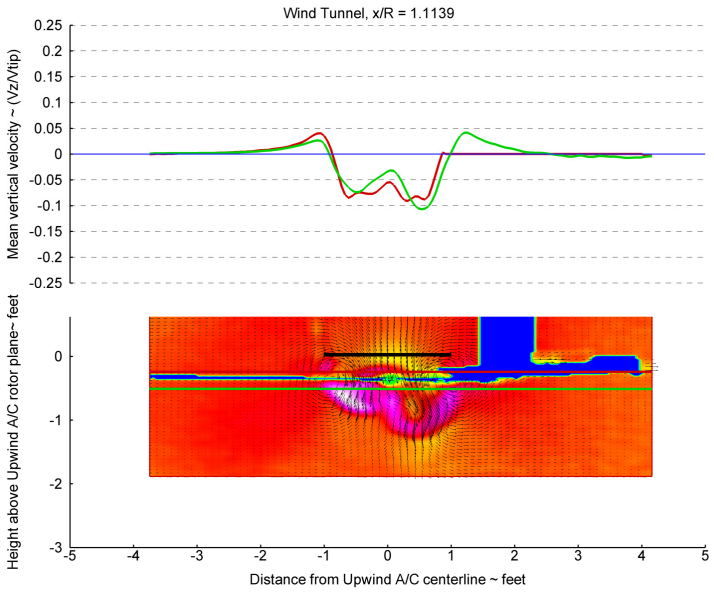

Figure 4.25: NASA PIV Image. Thrust coefficient = 0.009. Advance ratio = 0.0997 PIV image captured 1.1139 rotor radii downstream of the rotor.

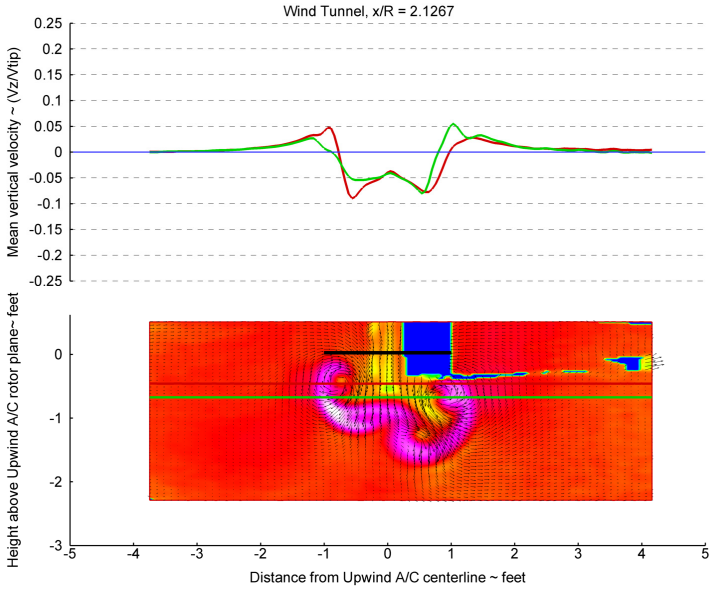

Figure 4.26: NASA PIV Image. Thrust coefficient = 0.009. Advance ratio = 0.0997 PIV image captured 2.1267 rotor radii downstream of the rotor.

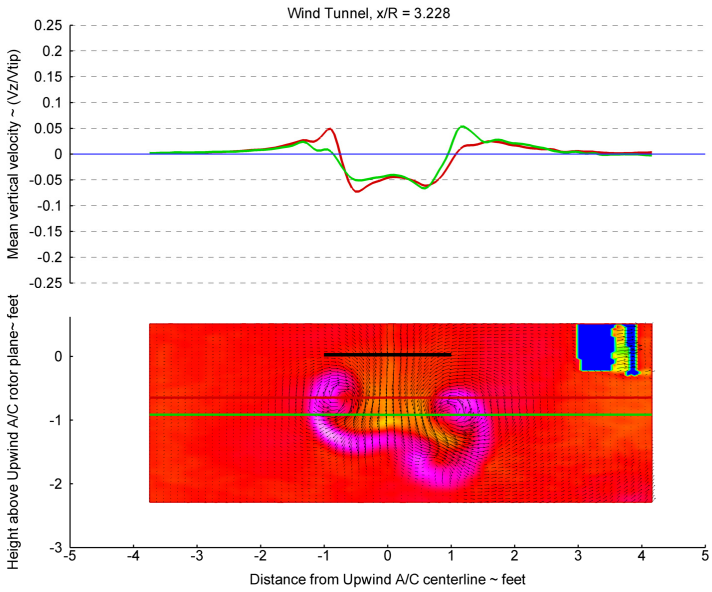

Figure 4.27: NASA PIV Image. Thrust coefficient = 0.009. Advance ratio = 0.0997 PIV image captured 3.228 rotor radii downstream of the rotor.

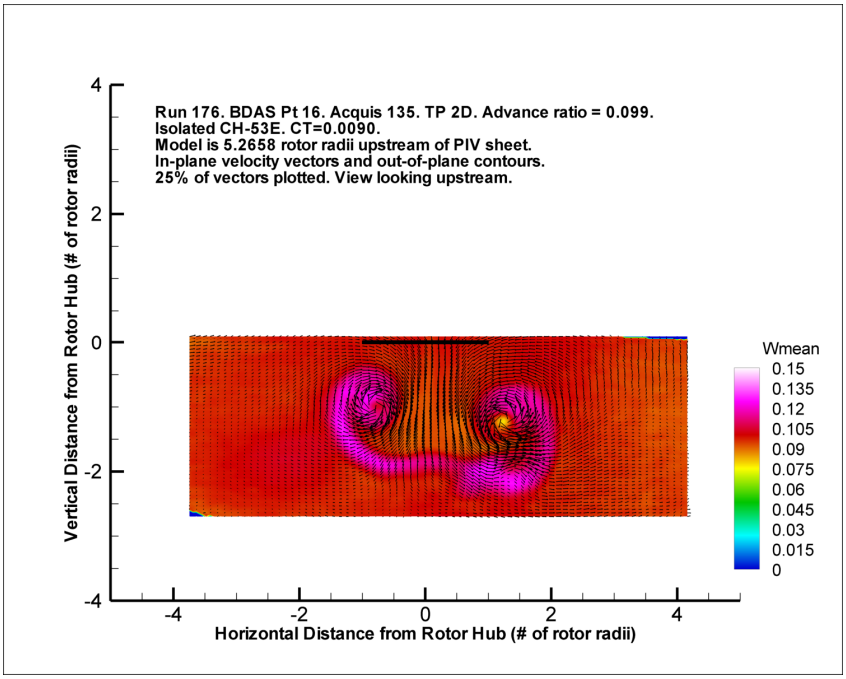

Figure 4.28: NASA PIV Image. Thrust coefficient = 0.009. Advance ratio = 0.0997 PIV image captured 5.2456 rotor radii downstream of the rotor.

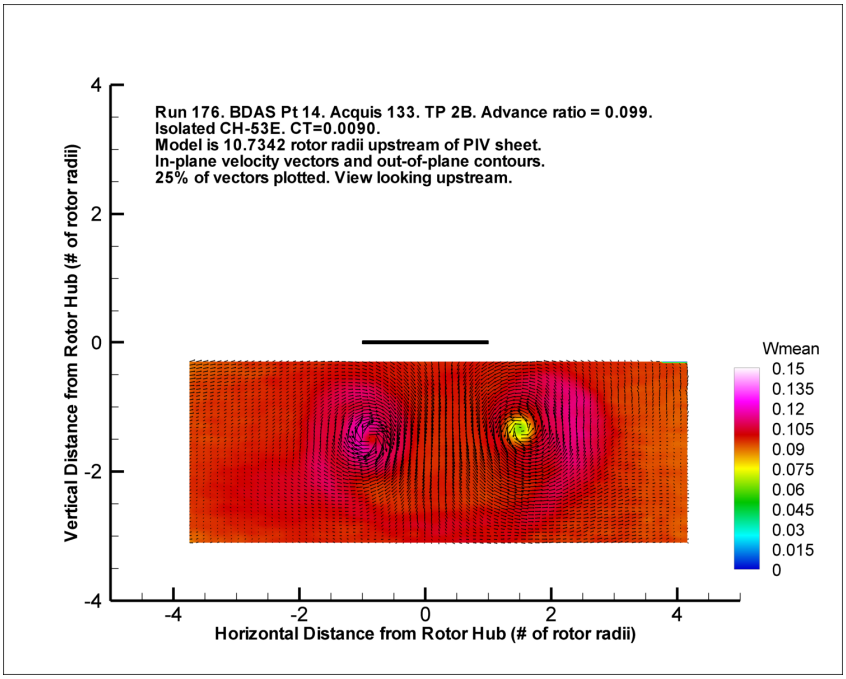

Figure 4.29: NASA PIV Image. Thrust coefficient = 0.009. Advance ratio = 0.0997 PIV image captured 10.7342 rotor radii downstream of the rotor.

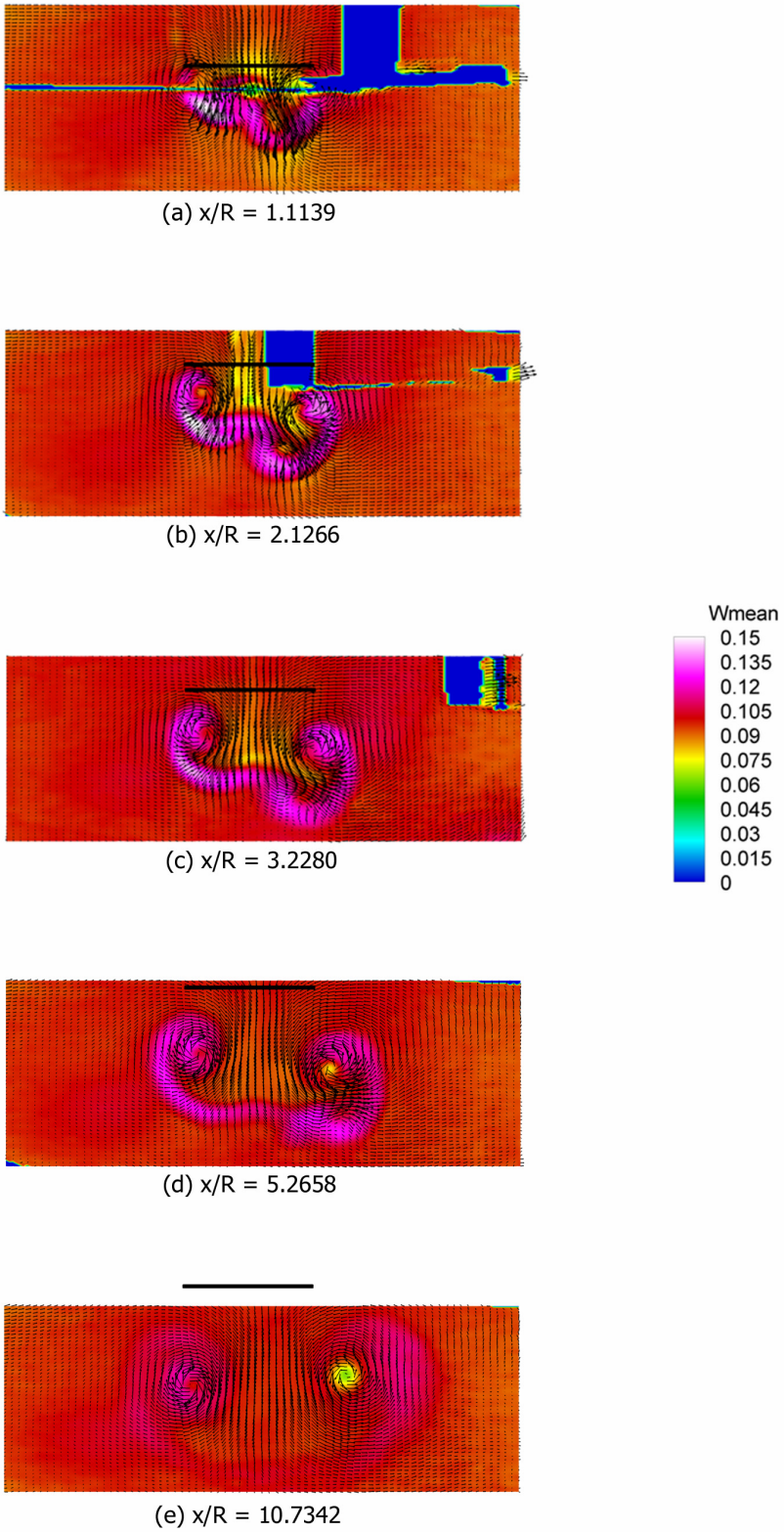

Figure 4.30: Collection of NASA PIV images. Thrust coefficient = 0.009. Advance ratio = 0.0997. PIV images captured 1.1139 - 10.7342 rotor radii downstream of the rotor.

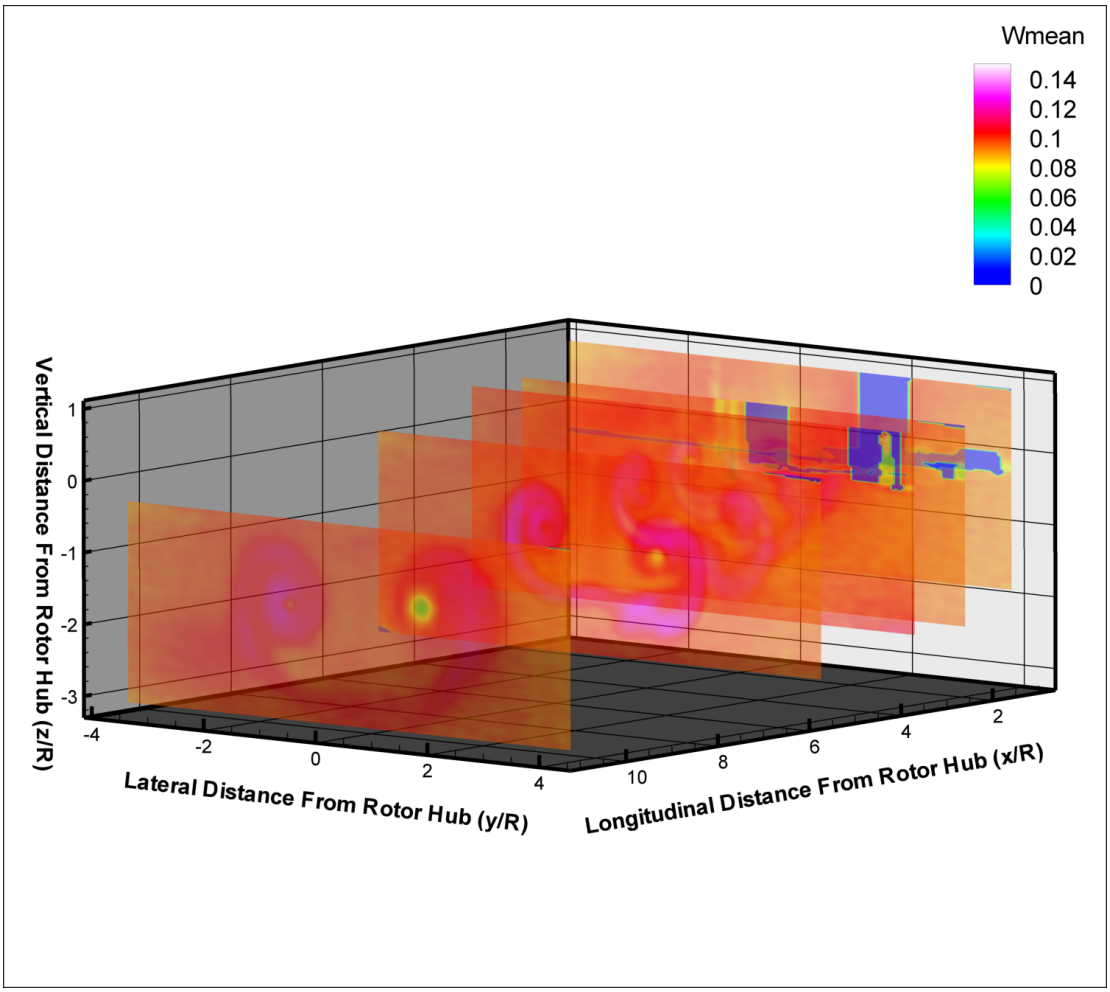

Figure 4.31: Isometric view of the NASA Wind Tunnel PIV images accurately placed in space to help visualize the rotor wake structure for the full-scale WOD 45 case.

In general, there is relatively good agreement between the MFW and wind tunnel results comparing Fig. 4.23 with 4.25 and Fig. 4.24 with 4.26 understanding that the wind tunnel rotor system characteristics could not be faithfully reproduced in the MFW code input files. The position, both laterally and vertically of the bundled left vortex correlates well between the free wake code and the wind tunnel results. The most degraded match is the out-of-plane velocities. The magnitudes predicted by

the MFW code are much higher than was observed in the wind tunnel. The exact reason for the over-prediction is unclear, and warrants further study.

The differences between the MFW results, and those obtained in the wind tunnel necessitated an advance ratio sensitivity study using the MFW code. As documented in Ref. 16, full-scale rotorcraft wake resembles that of a low aspect ratio fixed wing wake at speeds above 40 kts. In the NASA wind tunnel test the wake roll-up mechanism appears to be in place at a lower advance ratio. Instead of simply discarding the wake geometry files from the intermediate cases used to slowly march down to the target 0.0660 advance ratio, the wake geometry files were saved and plotted in an attempt to better understand the MFW code. In an attempt to better mimic the wind tunnel model rotor configuration, flapping was suppressed by increasing the rotor mass ten times. The input file variables for the entire set of advance ratio sweep cases are shown in Table 4.7.

Table 4.6: Input variables used for the advance ratio sensitivity analysis.

flight.input	
Paramter	Value
mu	Variable
muc	0.0
pbar	0.0
qbar	0.0
ct0	0.00901
t0_0	15.0
t1c0	0
t1s0	0
b0_0	0.10
b1c0	0
b1s0	0
cttol	1.0e-8
fltol	1.0e-8
altitude	0.0

(a)

geometry.input	
Paramter	Value
nr	1
nb	5
ns	32
asr0	0.0
rad	0.25083
flph	-1.0
rcout	0.324
crd	0.02819
twt	-10.65
om	320.77
taperst	1.0
taper	0.0
rotgeo	0

(b)

rotprop.input	
Paramter	Value
bmass	0.83724
kbeta	1.0
betap	1.0

(c)

user.input	
Paramter	Value
nw	1
pw	0
nfw	150
nk	1
ft	10
bct	2
dp	12
dz	12
rcb	0.05
dcy	0.0002
trm	y
lin	0.0
li	0.0
method	t
initial	n

(d)

The first case examined was for an advance ratio equal to 0.15. The wake geometry files are shown in Figs. 4.32 and 4.33. The wake is started from a prescribed solution as shown in Fig. 4.32(a) and 4.33(a). At the 40^{th} iteration, which corresponds to eight rotor turns of wake age, the start up transient is approximately six rotor radii downstream of the hub. The wake, as observed previously in the full-scale H-60 case, Fig. 4.17(c), contracts laterally upstream of the transient in Fig. 4.32(c) but this transient convects quickly out of the solution before its effects cause large amounts of aperiodicity. By the 110^{th} iteration, the solution has obtained a steady state condition. Bundles of filaments start to form in the far wake after about eight rotor radii, but they do not adversely affect the solution.

The second case was for an advance ratio of 0.14. The input files for this case remain the same as for the previous case. The only difference being the lower advance ratio set in the flight.input file. The wake geometry can be seen in Figs. 4.34 and 4.35.

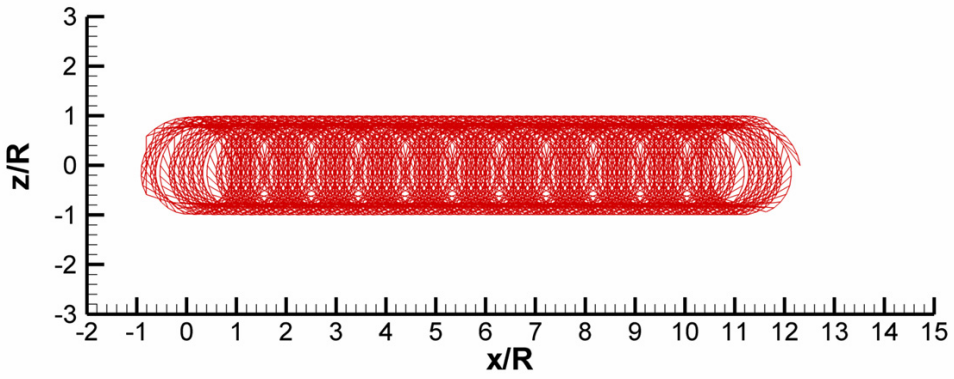

(a) Iteration = 0

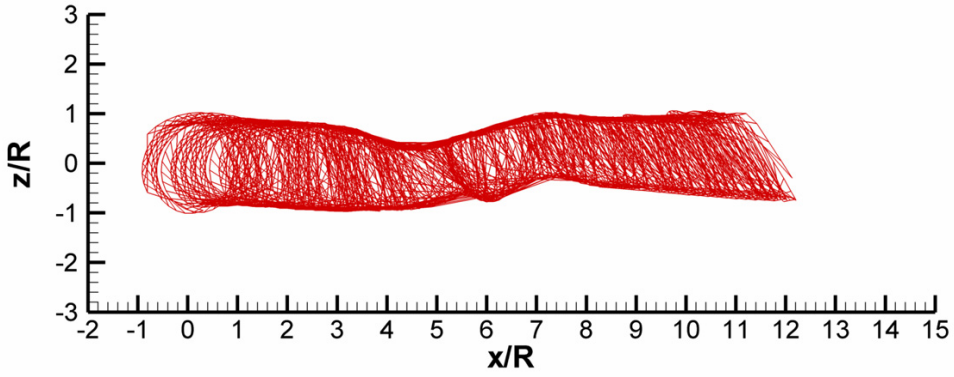

(b) Iteration = 40

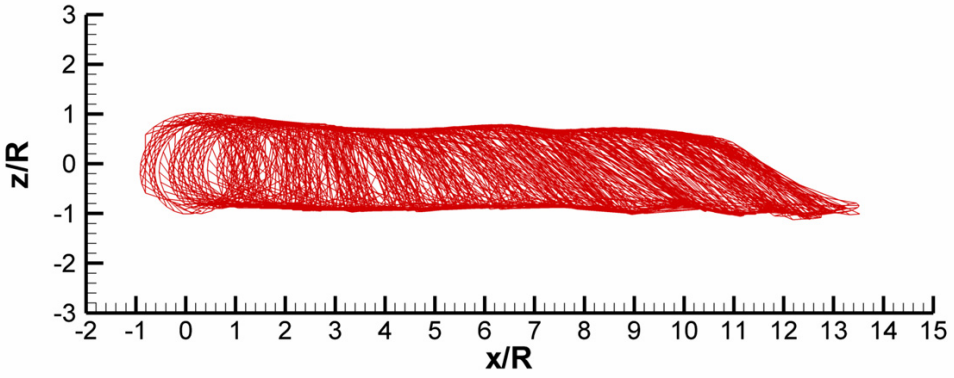

(c) Iteration = 110

Figure 4.32: MFW code generated wake geometry visualization for an advance ratio = 0.15. Top view.

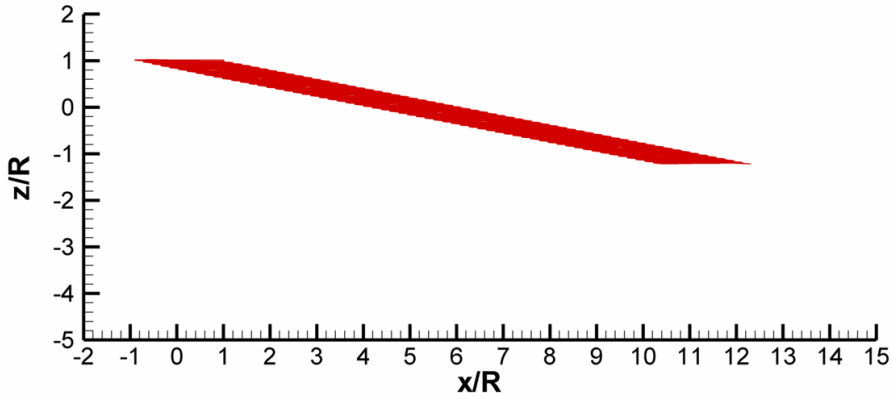

(a) Iteration = 0

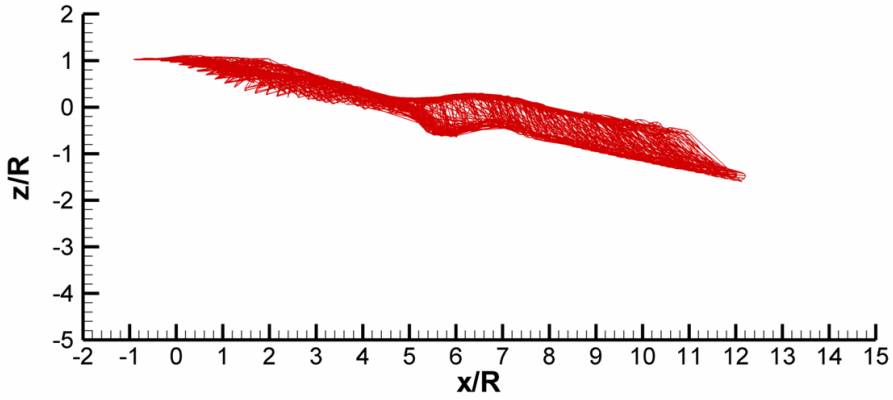

(b) Iteration = 40

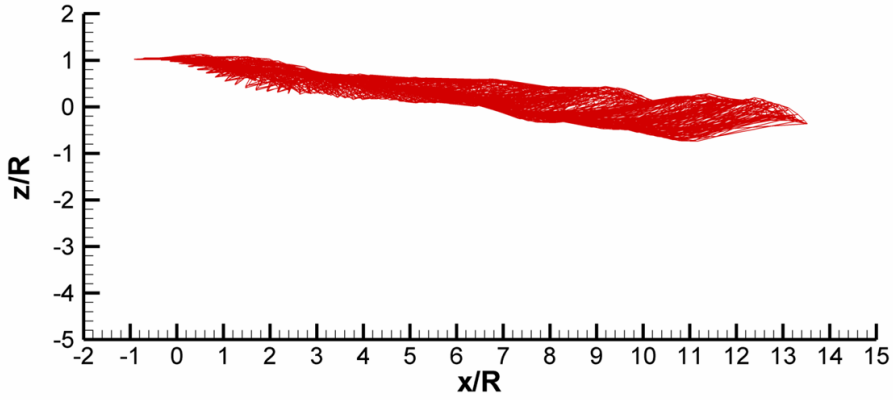

(c) Iteration = 110

Figure 4.33: MFW code generated wake geometry visualization for an advance ratio = 0.15. Side view.

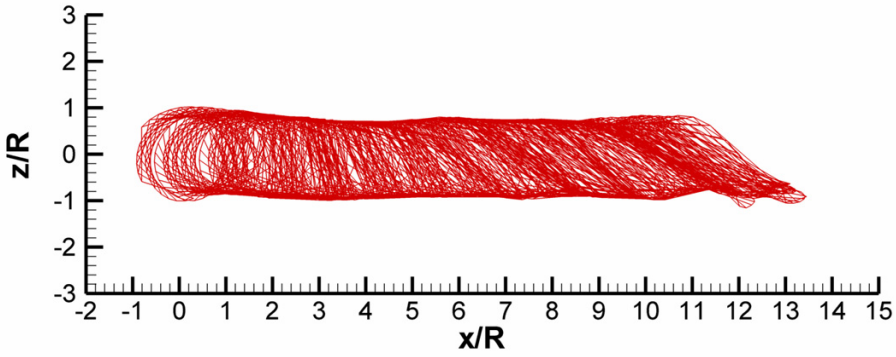

(a) Iteration = 0

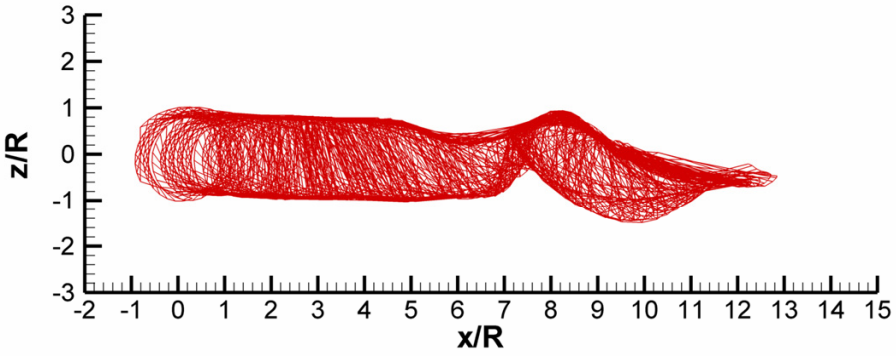

(b) Iteration = 60

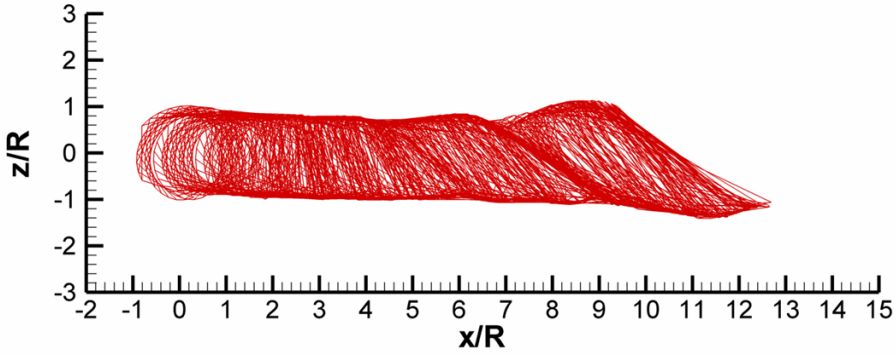

(c) Iteration = 130

Figure 4.34: MFW code generated wake geometry visualization for an advance ratio = 0.14. Top view.

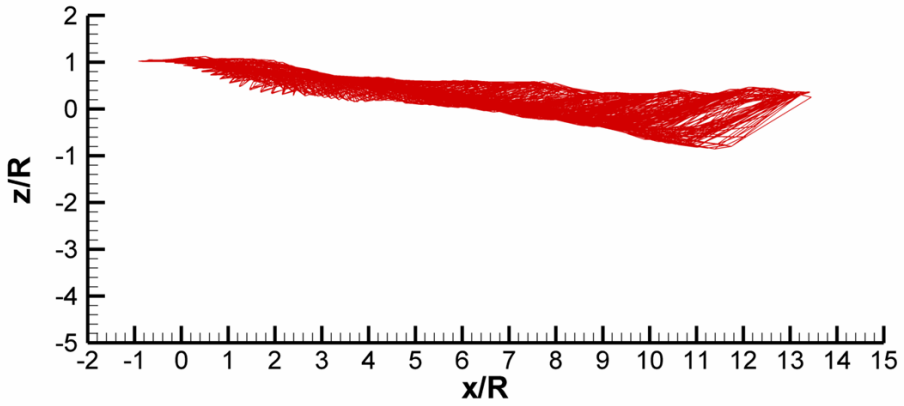

(a) Iteration = 0

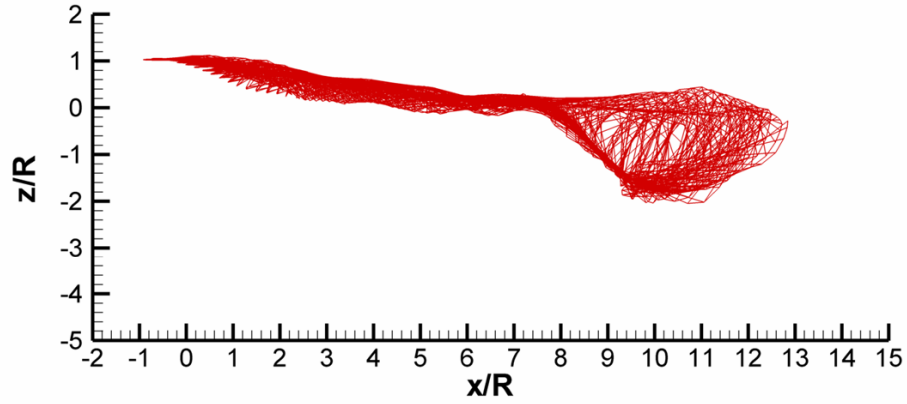

(b) Iteration = 60

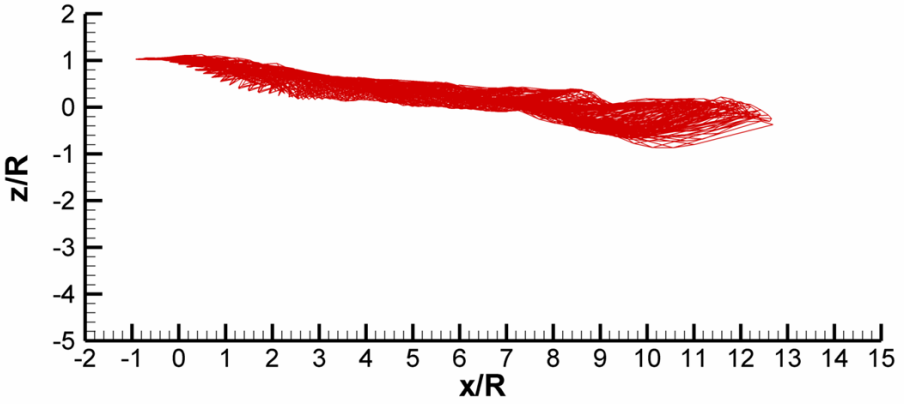

(c) Iteration = 130

Figure 4.35: MFW code generated wake geometry visualization for an advance ratio = 0.14. Side view.

As shown in Figs. 4.34(a) and 4.35(a), the last case's final iteration was used as the initial wake solution. Despite only decreasing the advance ratio by 0.01, the resulting transient caused some measurable effect on the overall wake geometry. In Fig. 4.34(b), the start up transient at seven rotor radii downstream laterally contracts the wake structure upstream and causes the filaments downstream to spread out, most notably in the vertical direction, as can be seen in Fig. 4.35. The wake still achieves a steady state prior to the last iteration step of 150, as seen in Figs. 4.34(c) and 4.35(c). The filament bundles in the far wake are more pronounced, and show up in waves with a set period but do not cause the wake to act erratically.

Marching down to an advance ratio of 0.13 did not change the wake structure appreciably, as seen in Figs. 4.36 and 4.37. The last iteration wake geometry solution from the previous case was used as the starting wake solution for this case. As the start up transient moved downstream the same contraction upstream, expansion downstream phenomenon occurred. This "whip effect" in the far wake was slightly more pronounced than the previous cases with a higher advance ratio, but the wake was still able to stabilize well before the final iteration step.

For an advance ratio of 0.12 the far wake, filament ring and the "whip effect" phenomenon become more pronounced, as seen in Figs. 4.38(b) and 4.39(b). The vortex filaments still roll up, and a nearly 90 degree wake skew angle is achieved. What is interesting is the stair step structure of the wake in Fig. 4.39(c), which is after the start-up transient has left the solution. There are three distinct portions of the wake, one from the hub to three rotor radii, the second from three to six radii, and the

third past six. The first and third section share the same approximate skew angle but the middle section is horizontal.

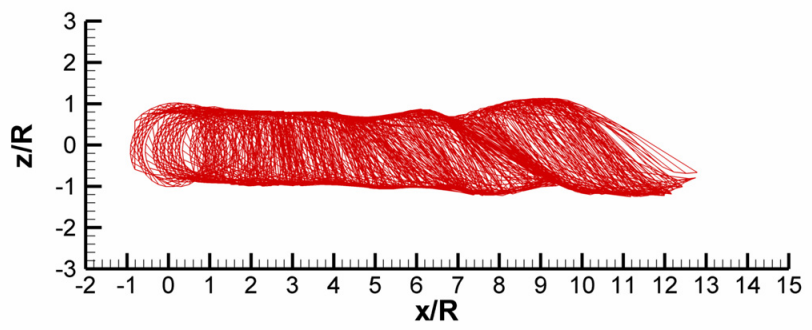

(a) Iteration = 0

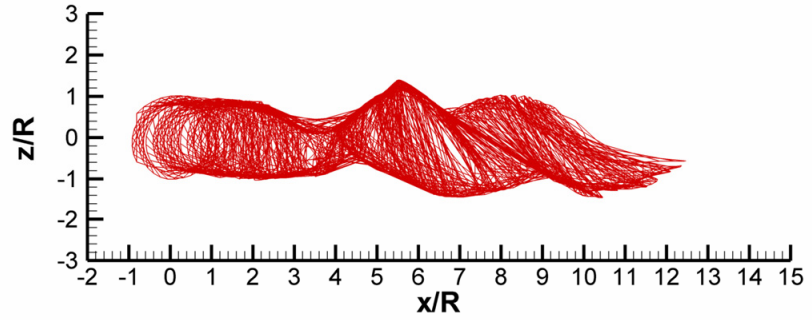

(b) Iteration = 40

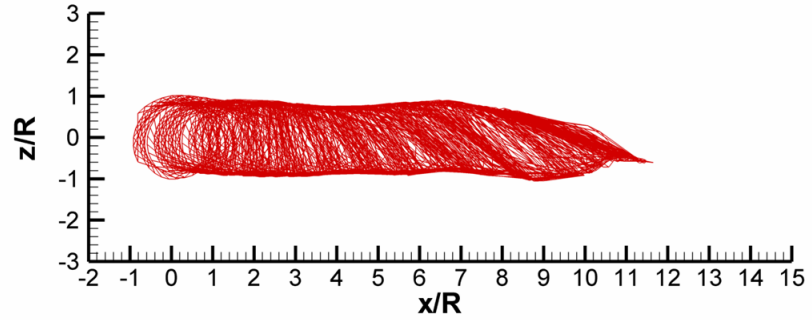

(c) Iteration = 122

Figure 4.36: MFW code generated wake geometry visualization for an advance ratio = 0.13. Top view.

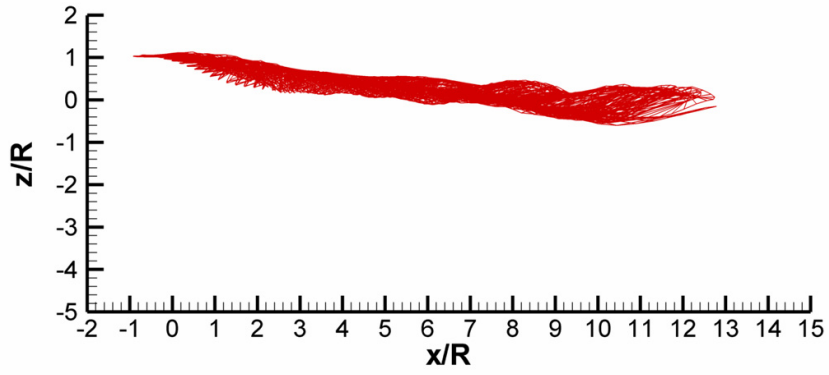

(a) Iteration = 0

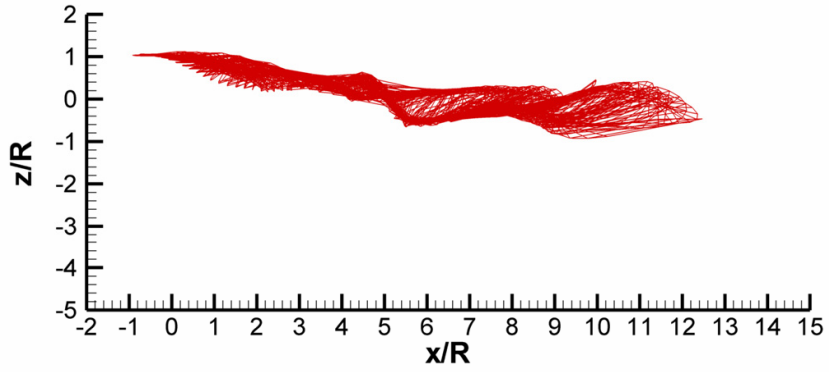

(b) Iteration = 40

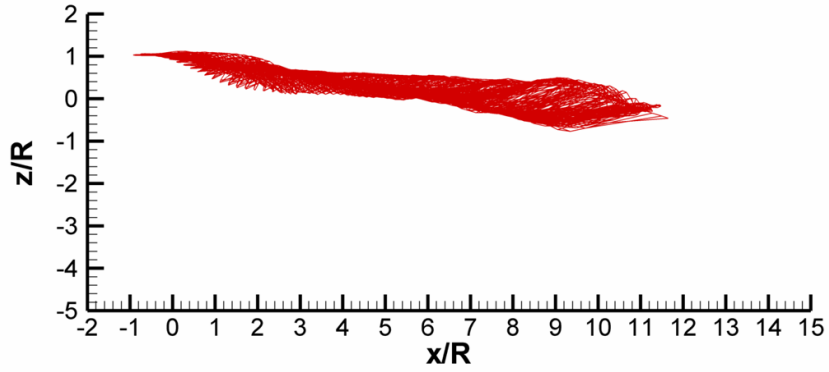

(c) Iteration = 122

Figure 4.37: MFW code generated wake geometry visualization for an advance ratio = 0.13. Side view.

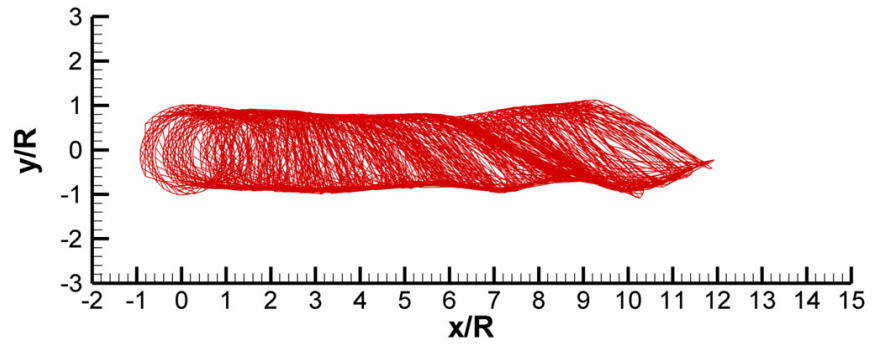

(a) Iteration = 0

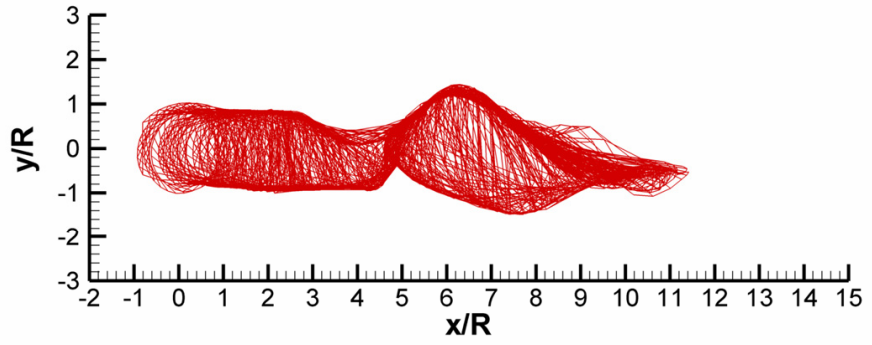

(b) Iteration = 50

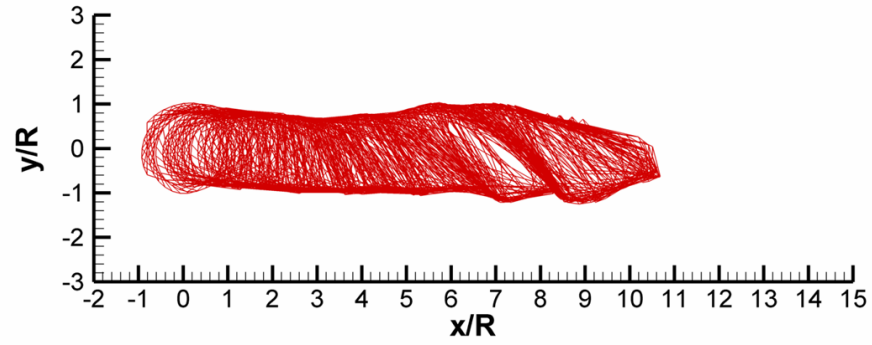

(c) Iteration = 100

Figure 4.38: MFW code generated wake geometry visualization for an advance ratio = 0.12. Top view.

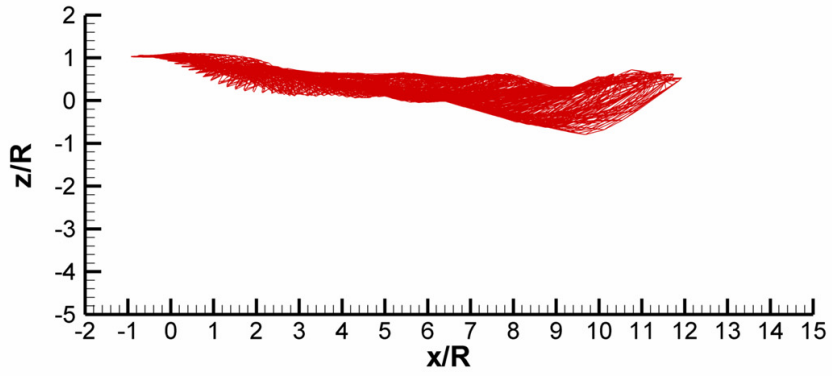

(a) Iteration = 0

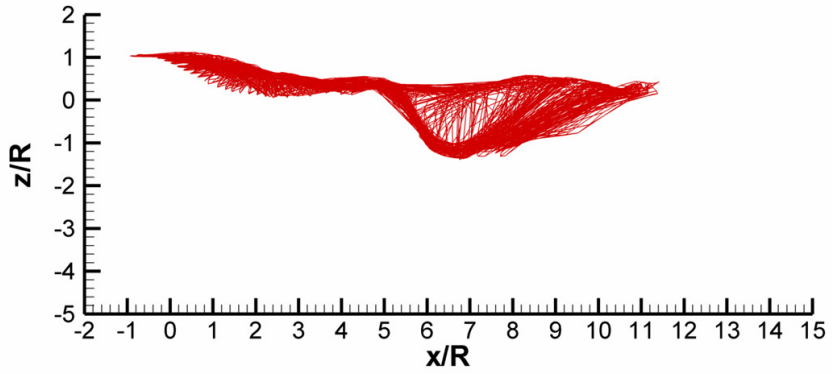

(b) Iteration = 50

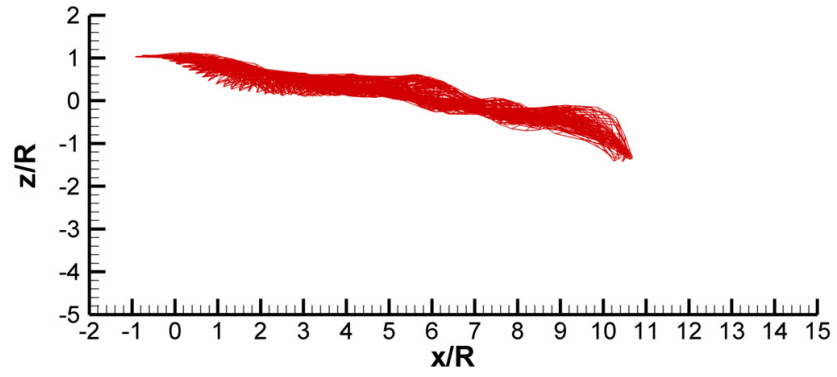

(c) Iteration = 100

Figure 4.39: MFW code generated wake geometry visualization for an advance ratio = 0.13. Side view.

Using the ending solution from the case with an advance ratio of 0.12 for the initial wake solution for the case with an advance ratio of 0.11, letting everything else remain constant, resulted in the wake geometries presented in Figs. 4.40 and 4.41.

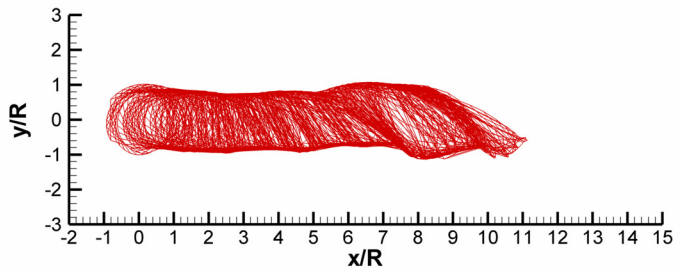

(a) Iteration = 0

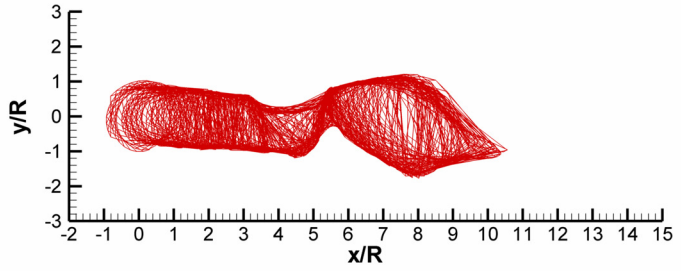

(b) Iteration = 60

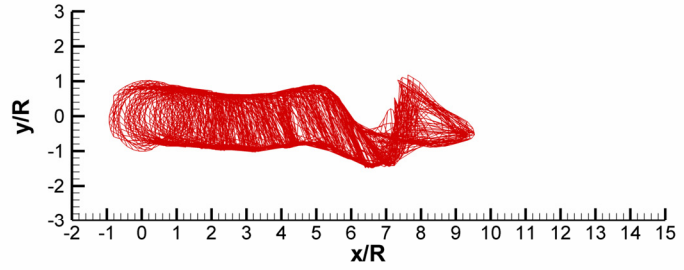

(c) Iteration = 89

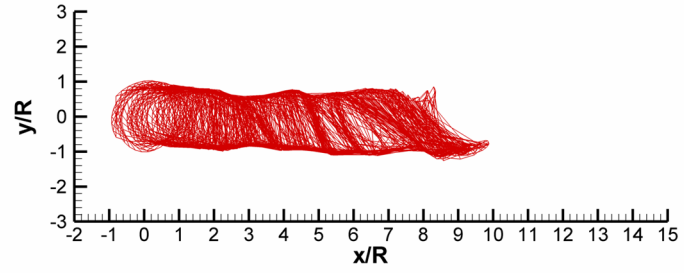

(d) Iteration = 125

Figure 4.40: MFW code generated wake geometry visualization for an advance ratio = 0.11. Top view.

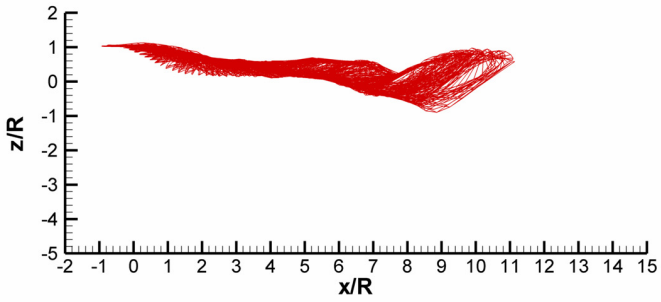

(a) Iteration = 0

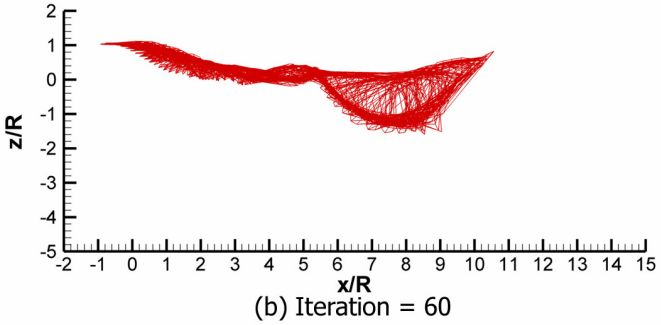

(b) Iteration = 60

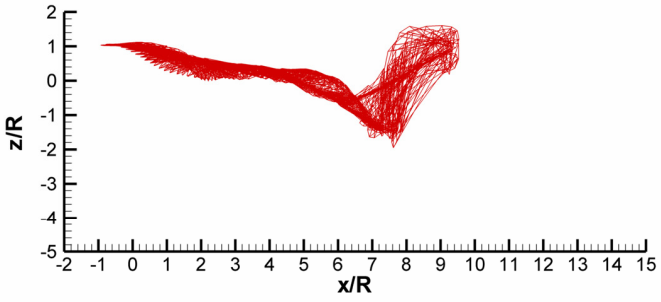

(c) Iteration = 89

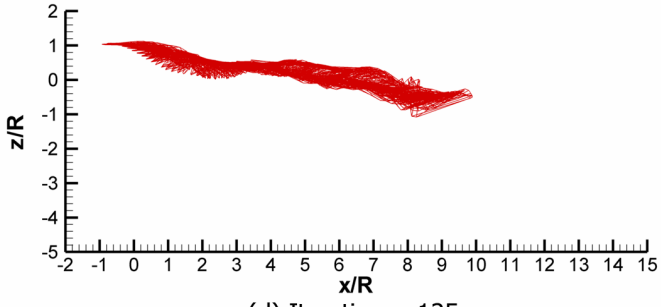

(d) Iteration = 125

Figure 4.41: MFW code generated wake geometry visualization for an advance ratio = 0.11. Side view.

The previously mentioned phenomenon exist for this case, but as seems to be the trend as advance ratio is lower, the magnitude of the effects are increased. At the 60^{th} iteration, the start up transient is halfway through the solution domain and by the 89^{th} iteration has almost left but its departure causes a large amplitude expansion of the wake vertically and a contraction of the wake laterally, as seen in Figs. 4.40(c) and 4.41(c). What's interesting to note is the advance side of the wake is the side that translates laterally and joins up with the retreating side. The close proximity of all those filaments, and their effect on each other, drives the wake to respond the way it does.

From an advance ratio of 0.15 down to 0.11, the start-up transient has caused some disturbance in the far wake. For each case though, the transient effects eventually disappear and the wake becomes quasi-steady. As shown in Figs. 4.42 and 4.43, this is not the case for an advance ratio of 0.0997. The solution is started from the last iteration solution from the previous case at an advance ratio of 0.11. The start-up transient moves downstream, and as those filaments shed at the first iteration step age, they begin to affect the flow both downstream and upstream as seen in Figs. 4.42(b) and 4.43(b). The wake behaves in a similar way as the higher advance ratio cases, where the wake contracts upstream of the transient and expands downstream of it.

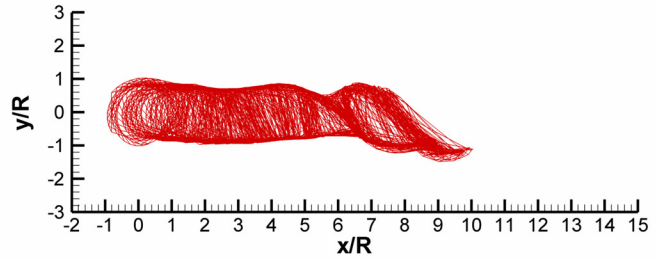

(a) Iteration = 0

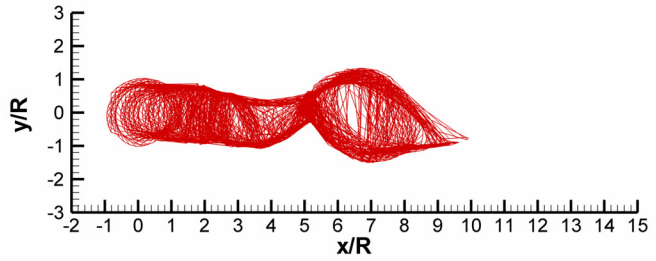

(b) Iteration = 60

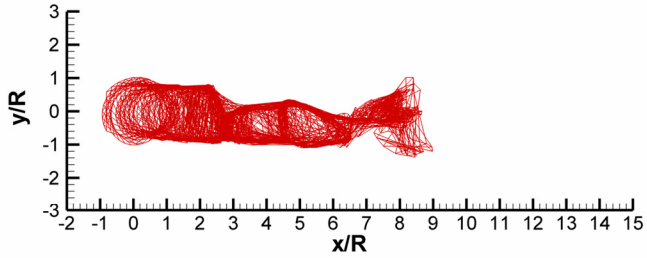

(c) Iteration = 85

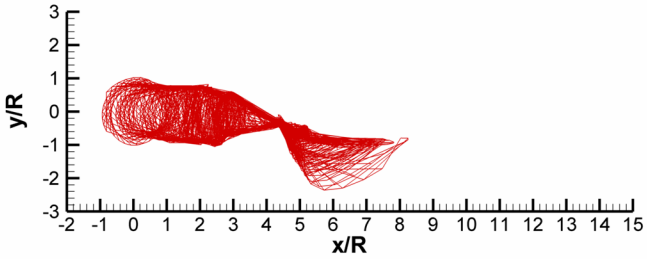

(d) Iteration = 140

Figure 4.42: MFW code generated wake geometry visualization for an advance ratio = 0.0997. Top view.

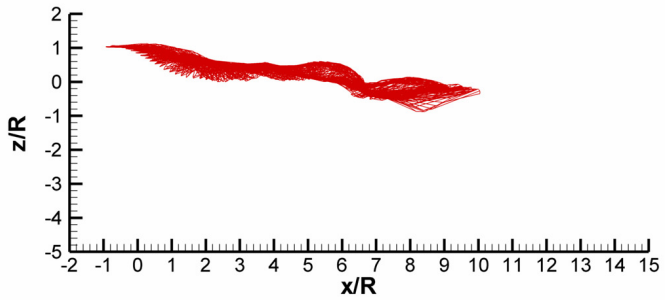

(a) Iteration = 0

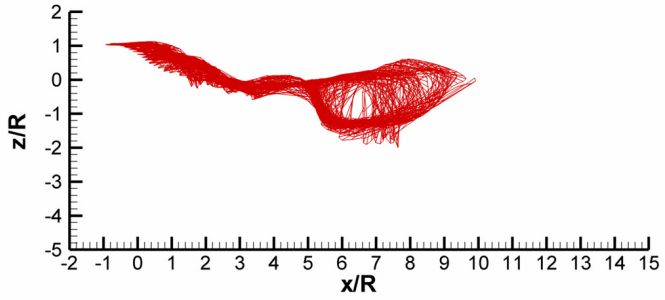

(b) Iteration = 60

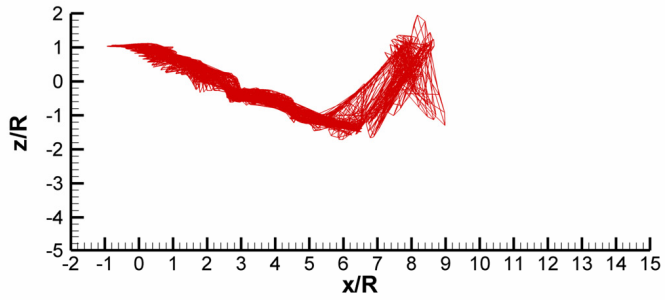

(c) Iteration = 85

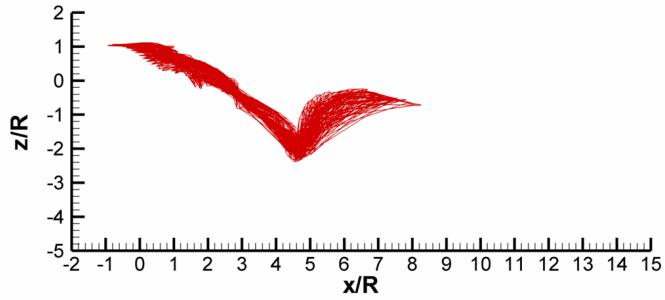

(d) Iteration = 140

Figure 4.43: MFW code generated wake geometry visualization for an advance ratio = 0.0997. Side view.

As the transient moves out the range of the solution, the wake has one constant skew angle unlike at the higher advance ratios, as seen in Figs. 4.43(c). It appears as if the MFW code predicts that the wake roll-up mechanism breaks down and a much smaller wake skew angle is predicted. As shown in Fig. 4.31, the wind tunnel results show that for the 0.0997 advance ratio condition, the wake is convected down just two rotor radii at over ten rotor radii downstream of the hub. If the aperiodicity is ignorned in Figs. 4.42 and 4.43 and the wake is extrapolated out to ten rotor radii, the predicted wake convects nearly four rotor radii down. And unlike the previous advance ratios investigated, the aperiodicity induced by the start-up transient does not dampen out. As shown in Figs. 4.42(d) and 4.43(d), well after the transient has been convected beyond the truncation point, aperiodicity in the wake still exists and is most prevalent beyond about three rotor radii downstream.

To see if this phenomenon ever damps out, a case was run using 120 revolutions of the rotor. Given the RPM of the model rotor, this equated to approximately two seconds of total time. The results in Figs. 4.44 and 4.45 confirm that the aperiodicity phenomenon does not damp out with time. At the 80^{th} iteration step, the start-up transient is leaving the solution. However, there are already wake aperiodicity drivers showing up in the wake, namely the wake constriction slightly past two rotor radii and the vortex filament ring between four and six rotor radii downstream. These phenomenon keep the aperiodicity from dampening out, and even at 570 iterations the wake solution is unusable much past two rotor radii. The initial conditions for this case can be seen in Table 4.8.

Table 4.7: Input file parameters for the MFW case with an adance ratio of 0.0997 and the number of iterations set to 600.

flight.input	
Paramter	Value
mu	0.0997
muc	0.0
pbar	0.0
qbar	0.0
ct0	0.00901
t0_0	15.0
t1c0	0
t1s0	0
b0_0	0.100
b1c0	0
b1s0	0
cttol	1.0e-8
fltol	1.0e-8
altitude	0.0

(a)

geometry.input	
Paramter	Value
nr	1
nb	5
ns	32
asr0	0.0
rad	0.25083
flph	-1.0
rcout	0.324
crd	0.02819
twt	-10.65
om	320.77
taperst	1.0
taper	0.0
rotgeo	0

(b)

rotprop.input	
Paramter	Value
bmass	0.83724
kbeta	0.0
betap	0.0

(c)

user.input	
Paramter	Value
nw	1
pw	0
nfw	600
nk	1
ft	10
bct	2
dp	12
dz	12
rcb	0.05
dcy	0.0002
trm	y
lin	0.0
li	0.0
method	t
initial	b

(d)

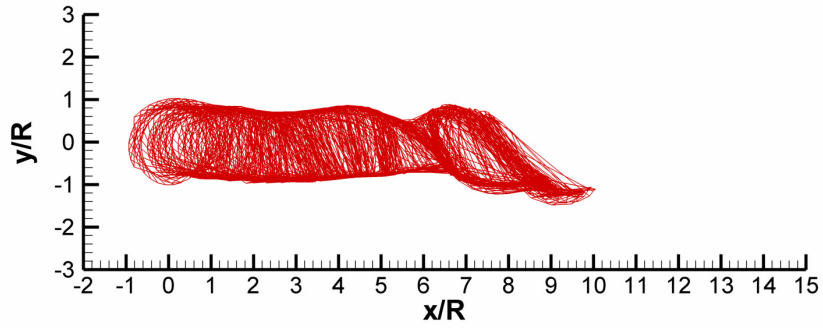

(a) Iteration = 0

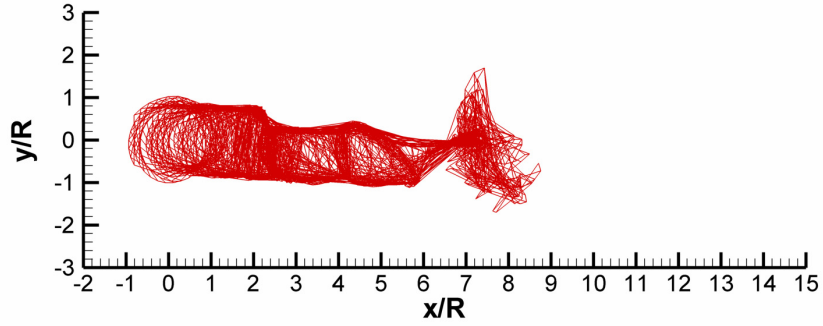

(b) Iteration = 80

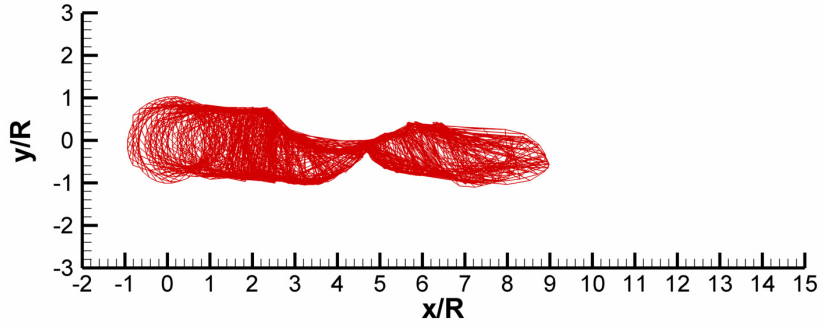

(c) Iteration = 100

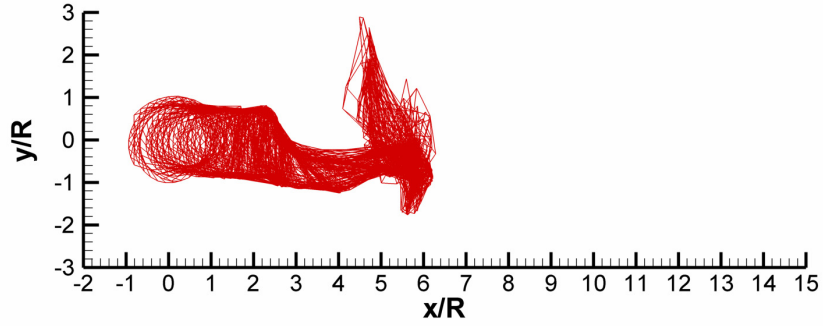

(d) Iteration = 570

Figure 4.44: MFW code generated wake geometry visualization for an advance ratio = 0.0997. Top view. nfw = 600.

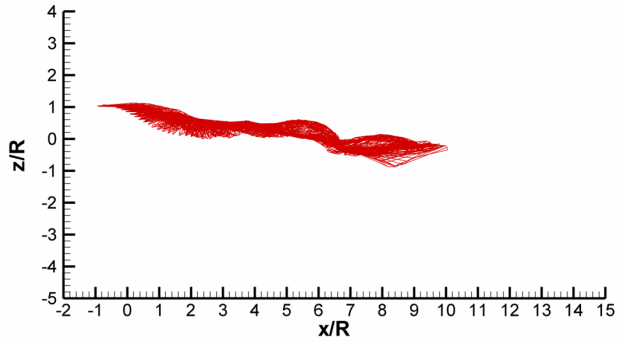

(a) Iteration = 0

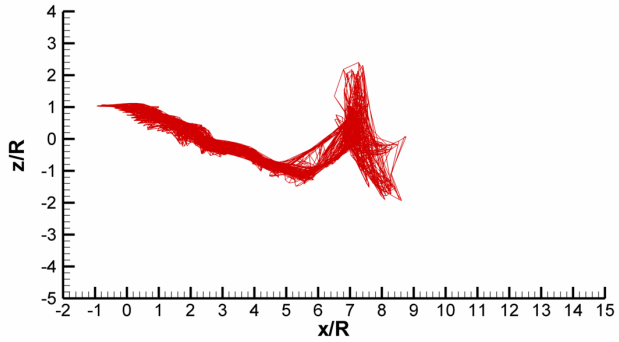

(b) Iteration = 80

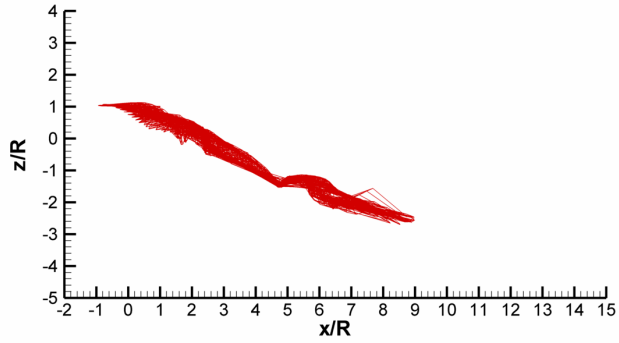

(c) Iteration = 100

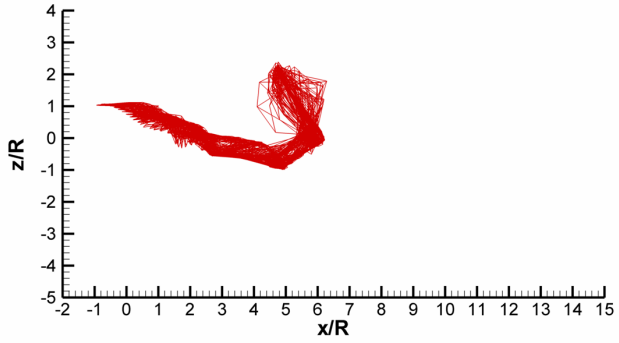

(d) Iteration = 570

Figure 4.45: MFW code generated wake geometry visualization for an advance ratio = 0.0997. Side view. nfw = 600.

The other advance ratio of interest was 0.0660. To arrive at this target advance ratio, the advance ratio was increased in increments of 0.01 from a hover. This was done in hopes of avoiding the area of high wake aperiodicity at an advance ratio of 0.0997. The results of this advance ratio sweep can be seen in Figs. 4.46 to 4.52. In a hover the vortex filaments bundle into filament rings, as seen in Fig. 4.46(b). However, in later iterations instabilities in the wake develop. It begins with one of the filament rings not remaining completely horizontal and equally spaced from the adjacent filament rings. This quickly destabilizes the entire far wake causing the geometry seen in Fig. 4.46(c). Because of the large amount of rotor turns that the filaments are kept in the solution, these unstable vortex filament rings do not go away quickly and in every advance ratio examined from hover to 0.06, drive the solutions unstable.

This degree of aperiodic wake behavior predicted by the MFW code is not supported by the data gathered from the NASA wind tunnel test. In Figs. 4.53 through 4.58, the results from the Group A testing is presented. This testing was accomplished at an advance ratio of 0.044. While these images are phase averaged and the wake geometries from the MFW code shown in Figs. 4.53 through 4.58 are instantaneous snapshots of the wake evolution, the coherent structure of the two, super vortices are clear in the NASA wind tunnel figures. This implies that the degree of aperiodicity predicted by the MFW code and shown in Figs. 4.50 and 4.51, is not supported by the wind tunnel data. It is also interesting to note that even at this low advance ratio the rotor wake still exhibits a weak roll-up mechanism. Two very diffused, and quite large vortices still form downstream from the rotor. These are not

nearly as organized or strong as the ones seen at advance ratios of 0.0660 and 0.0997, but they do exist.

The original data submission from NASA contained just the phase averaged data files from the two wind tunnel runs. The aperiodicity of the flow within the wind tunnel was unknown. The original PIV images that were used to generate the averaged images from the Group F points were obtained and analyzed. Only the Group F points up to and including 5.228 rotor radii downstream of the hub, were requested because points slower, farther downstream or both, when run in the MFW code, yielded unusable results. The individual frames of data were examined and while there is variation between images, as seen in Figs. 4.60 and 4.62, it is relatively small compared to that predicted by the MFW code as shown in Figs. 4.44 and 4.45.

To further help visualize the wake structure, the out-of-plane component of vorticity was calculated from the original PIV data files for two points downstream of the rotor hub: 3.228 and 5.266 rotor radii as seen in Figs. 4.59 and 4.61. These two locations were picked because the aperiodicity at the advance ratio of 0.0997 did not really become evident till after three rotor radii downstream. It has been shown previously in Figs. 4.23 through 4.26, that the MFW code and the wind tunnel results agree relatively well for 1.114 and 2.1266 rotor radii downstream of the rotor. These vorticity images contained in Figs. 4.59 and 4.61, show that the vortex cores do not move, or change strength a great deal over the 25 second window that data is gathered.

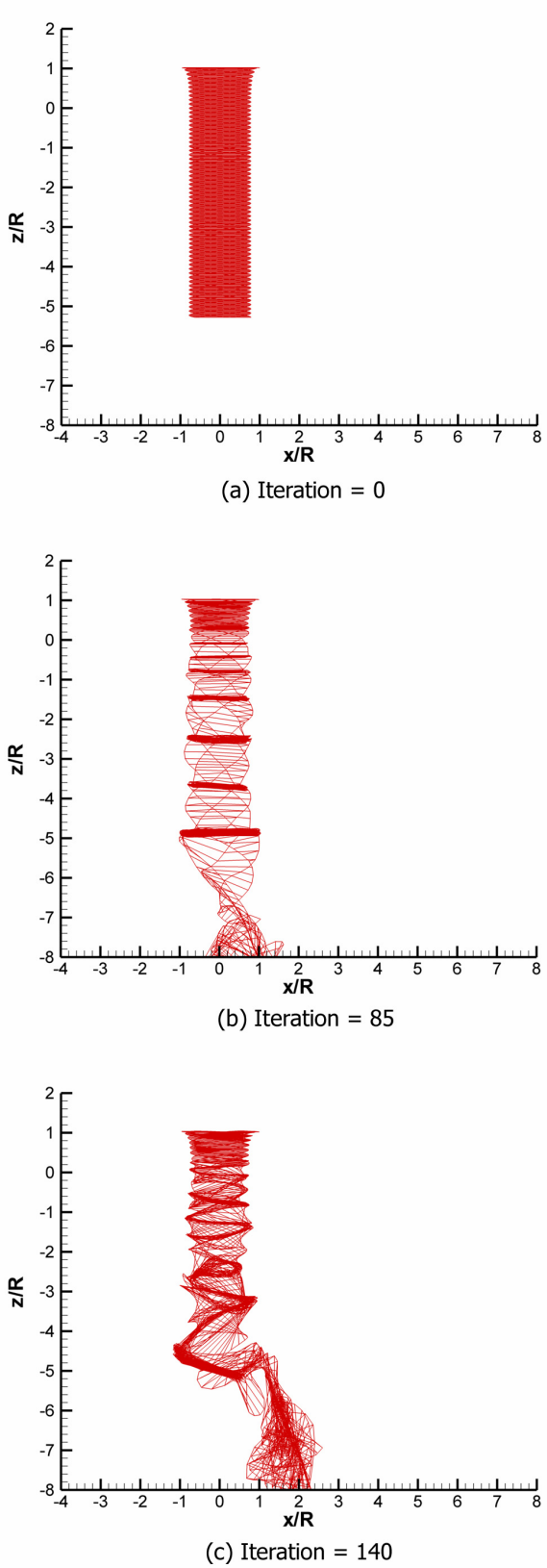

Figure 4.46: MFW code generated wake geometry visualization for a hover. Side view.

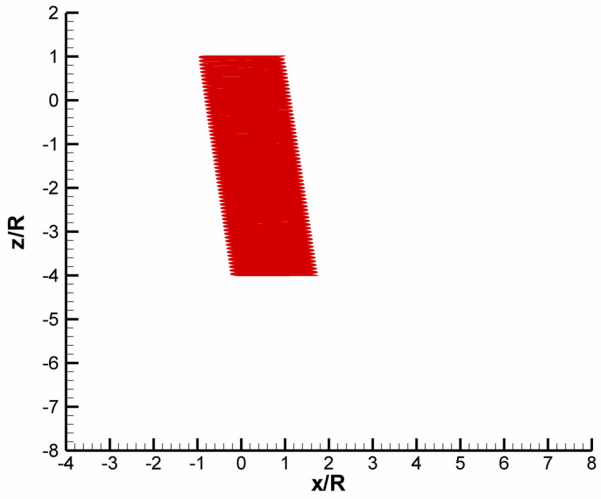

(a) Iteration = 0

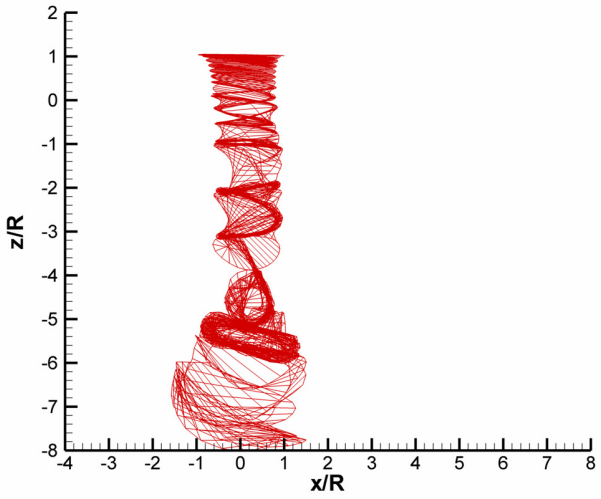

(b) Iteration = 111

Figure 4.47: MFW code generated wake geometry visualization for an advance ratio = 0.01. Side view.

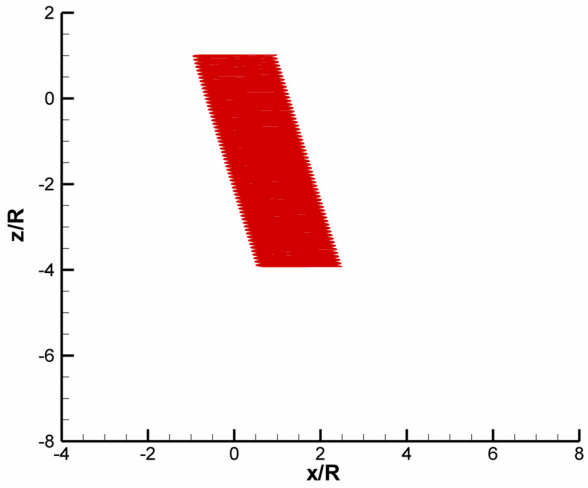

(a) Iteration = 0

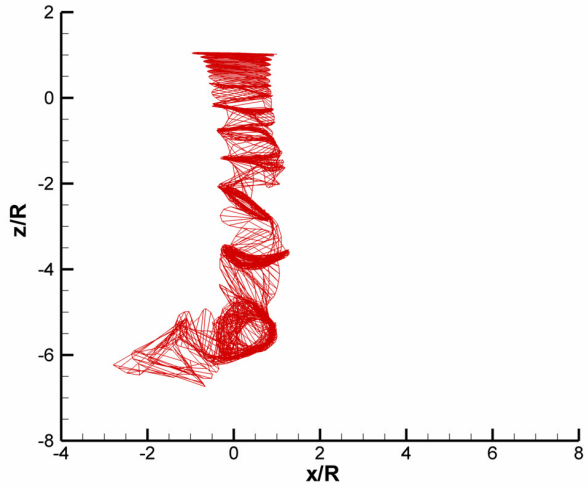

(b) Iteration = 150

Figure 4.48: MFW code generated wake geometry visualization for an advance ratio = 0.02. Side view.

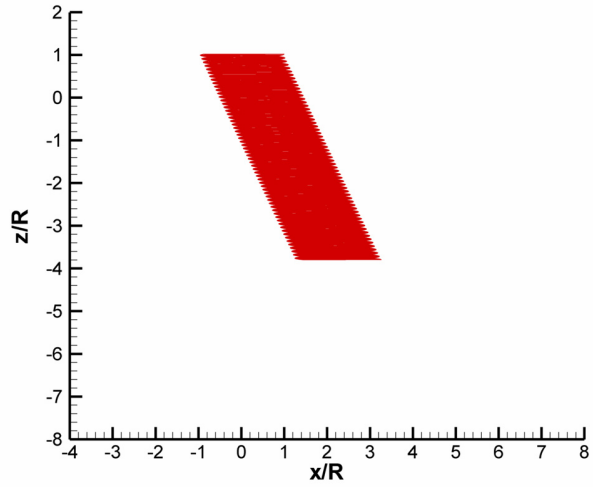

(a) Iteration = 0

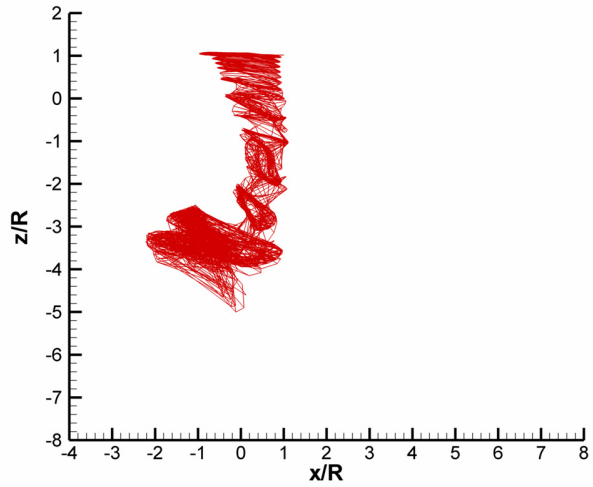

(b) Iteration = 120

Figure 4.49: MFW code generated wake geometry visualization for an advance ratio = 0.03. Side view.

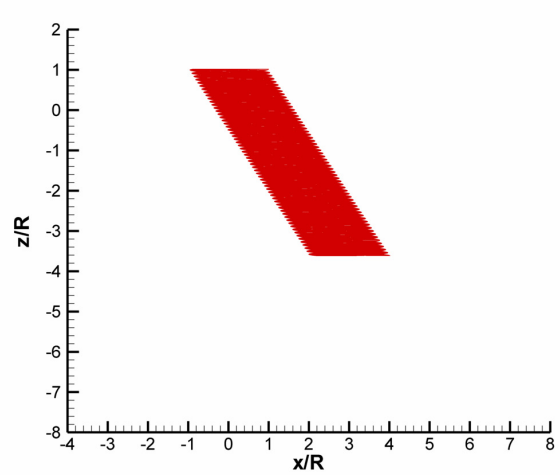

(a) Iteration = 0

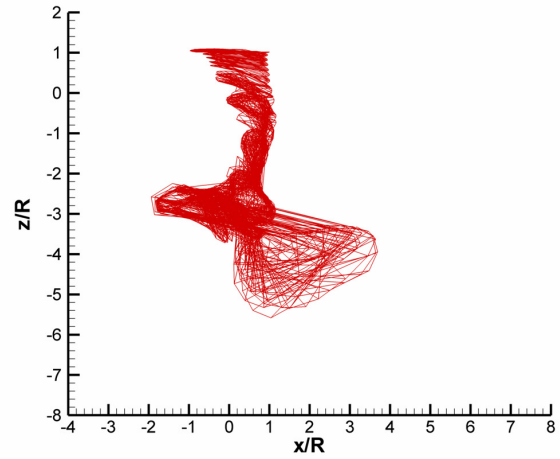

(b) Iteration = 75

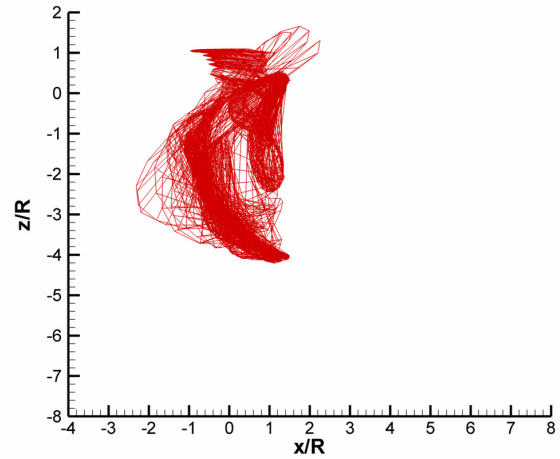

(c) Iteration = 150

Figure 4.50: MFW code generated wake geometry visualization for an advance ratio = 0.04. Side view.

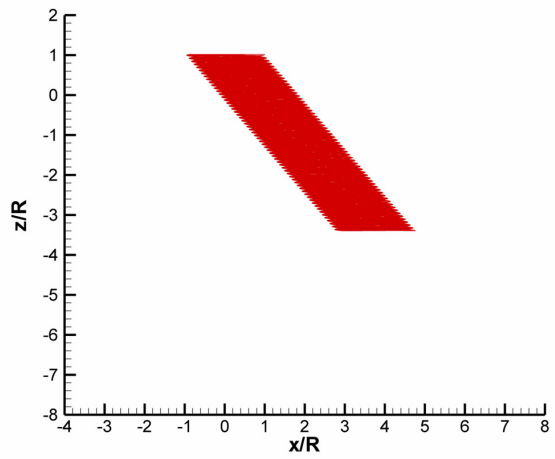

(a) Iteration = 0

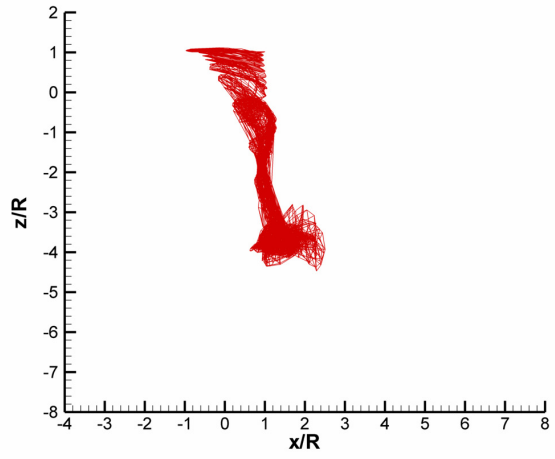

(b) Iteration = 75

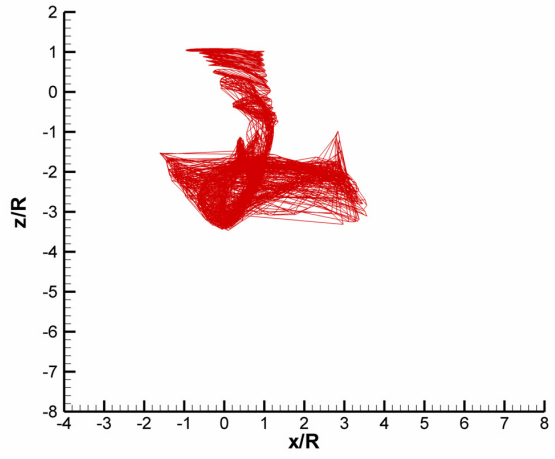

(c) Iteration = 150

Figure 4.51: MFW code generated wake geometry visualization for an advance ratio = 0.05. Side view.

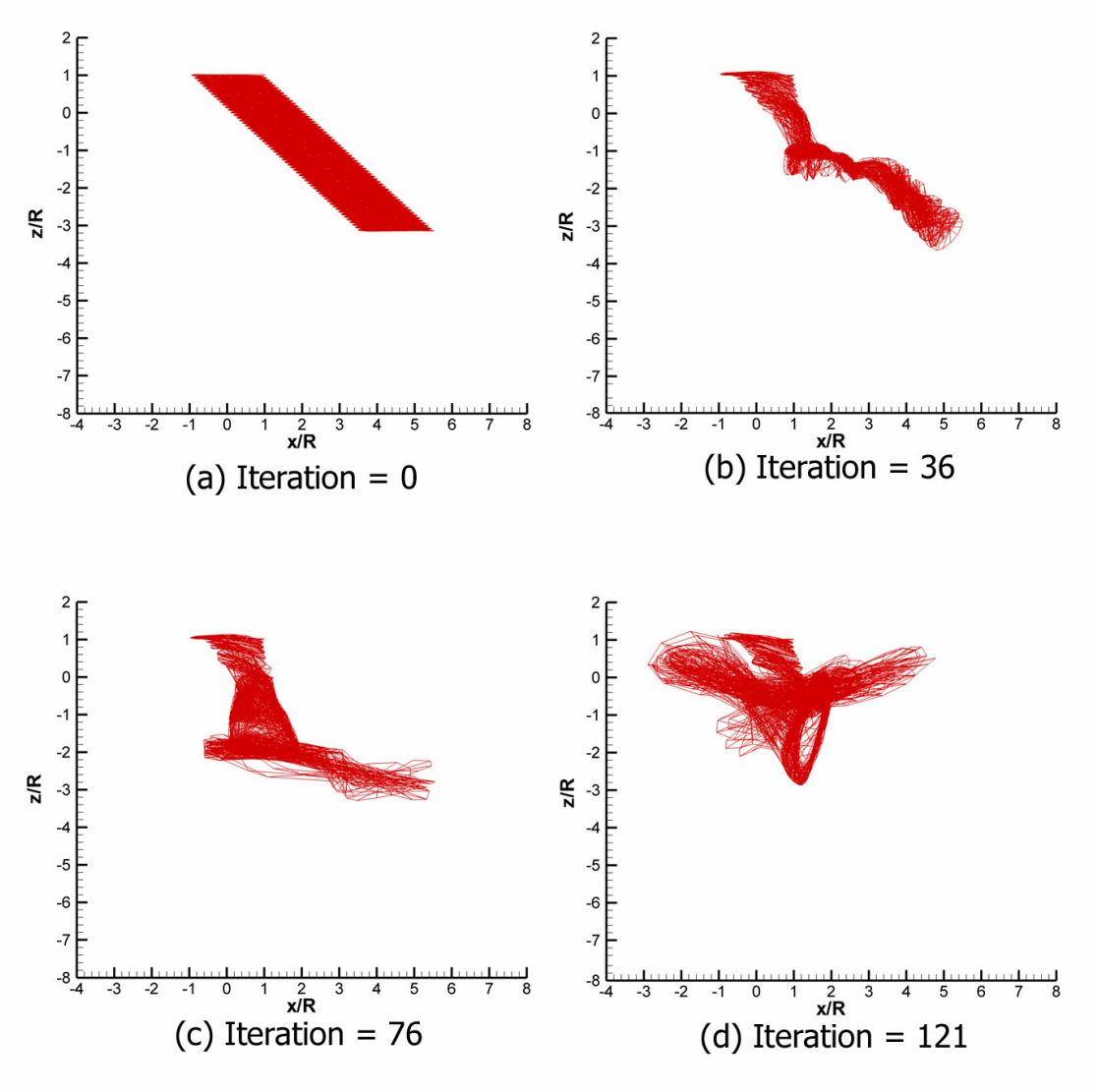

Figure 4.52: MFW code generated wake geometry visualization for an advance ratio = 0.06. Side view.

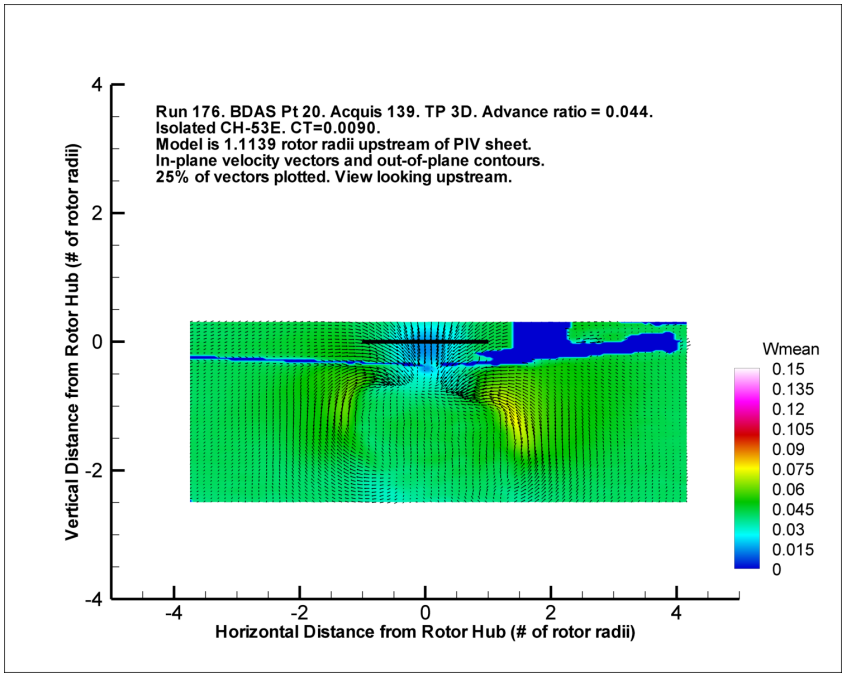

Figure 4.53: NASA PIV Image. Thrust coefficient = 0.009. Advance ratio = 0.044. PIV image captured 1.1129 rotor radii downstream of the rotor.

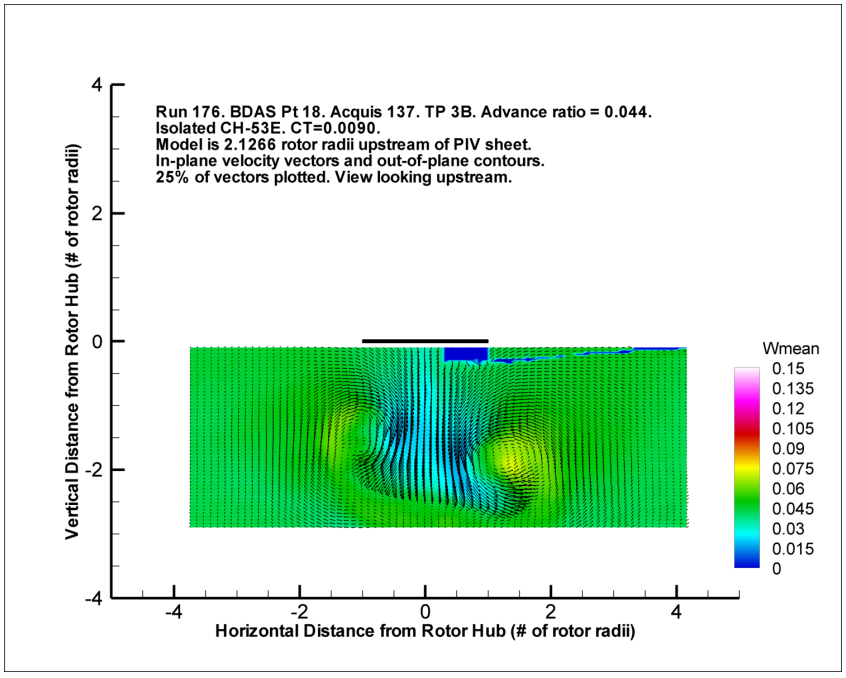

Figure 4.54: NASA PIV Image. Thrust coefficient = 0.009. Advance ratio = 0.044. PIV image captured 2.1266 rotor radii downstream of the rotor.

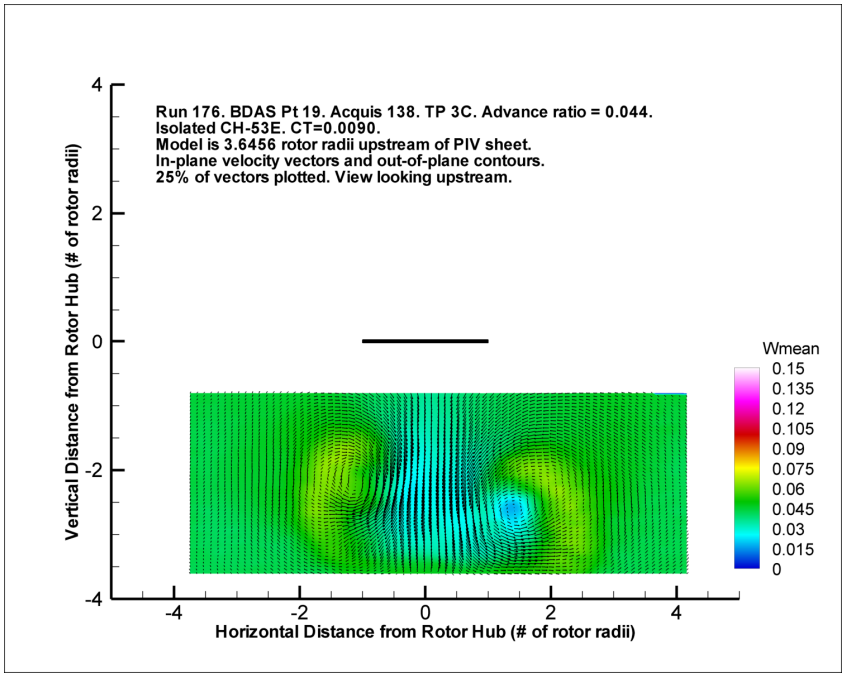

Figure 4.55: NASA PIV Image. Thrust coefficient = 0.009. Advance ratio = 0.044. PIV image captured 3.4456 rotor radii downstream of the rotor.

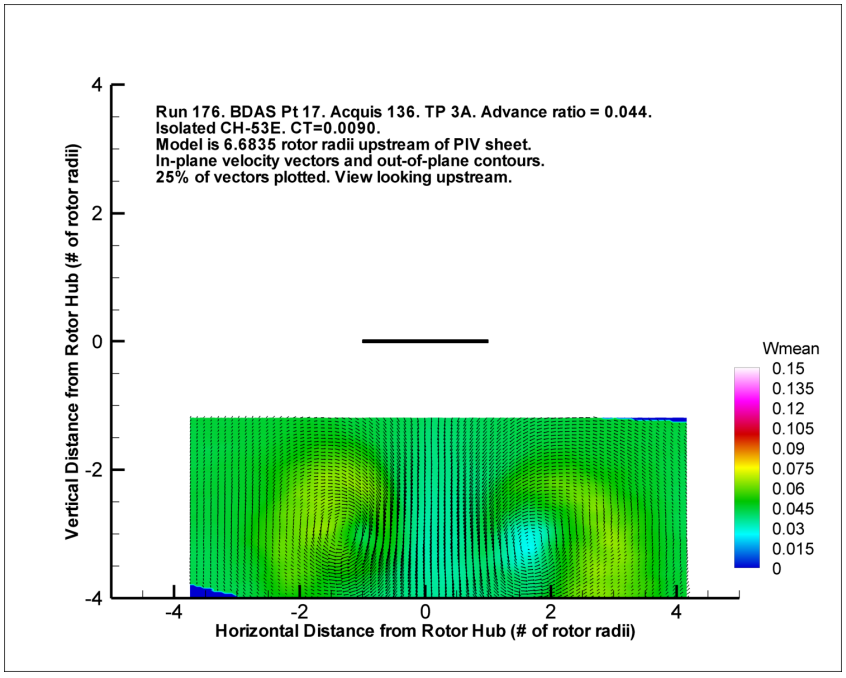

Figure 4.56: NASA PIV Image. Thrust coefficient = 0.009. Advance ratio = 0.044. PIV image captured 6.6835 rotor radii downstream of the rotor.

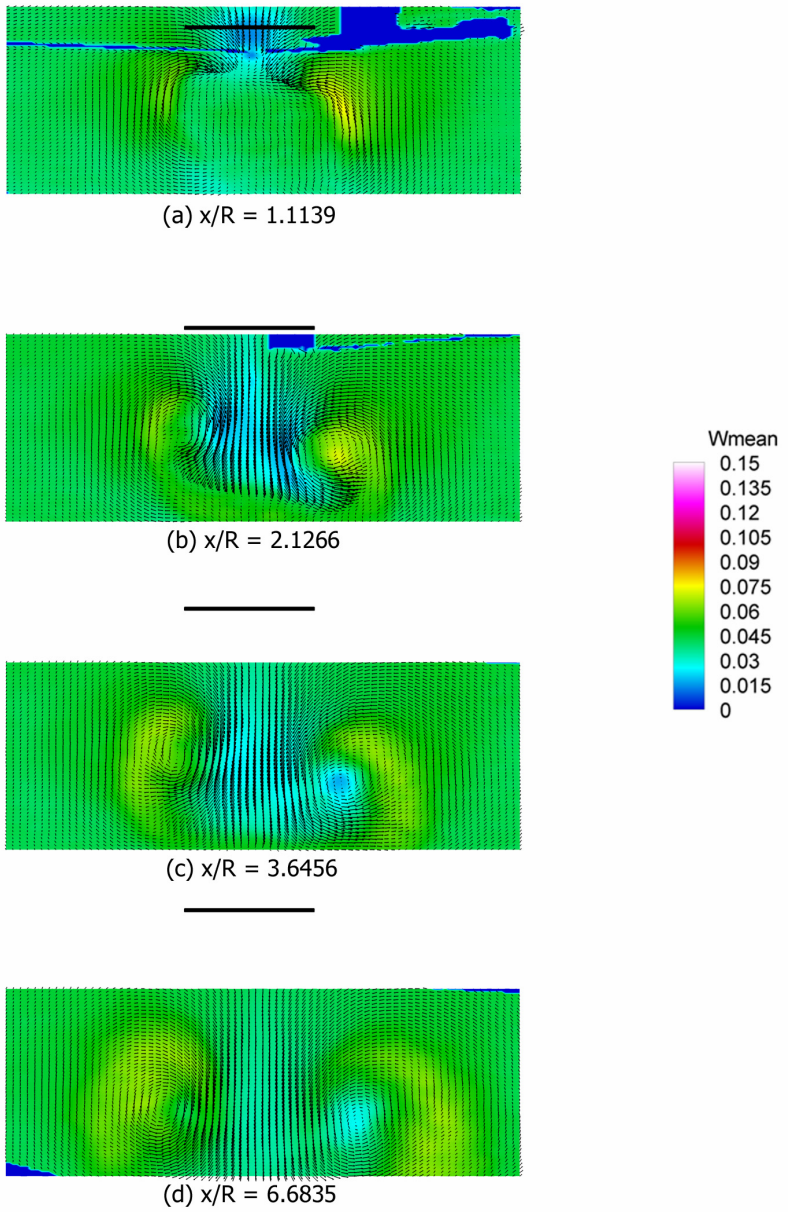

Figure 4.57: Collection of NASA PIV images. Thrust coefficient = 0.009. Advance ratio = 0.044. PIV images captured 1.1139 - 6.6835 rotor radii downstream of the rotor.

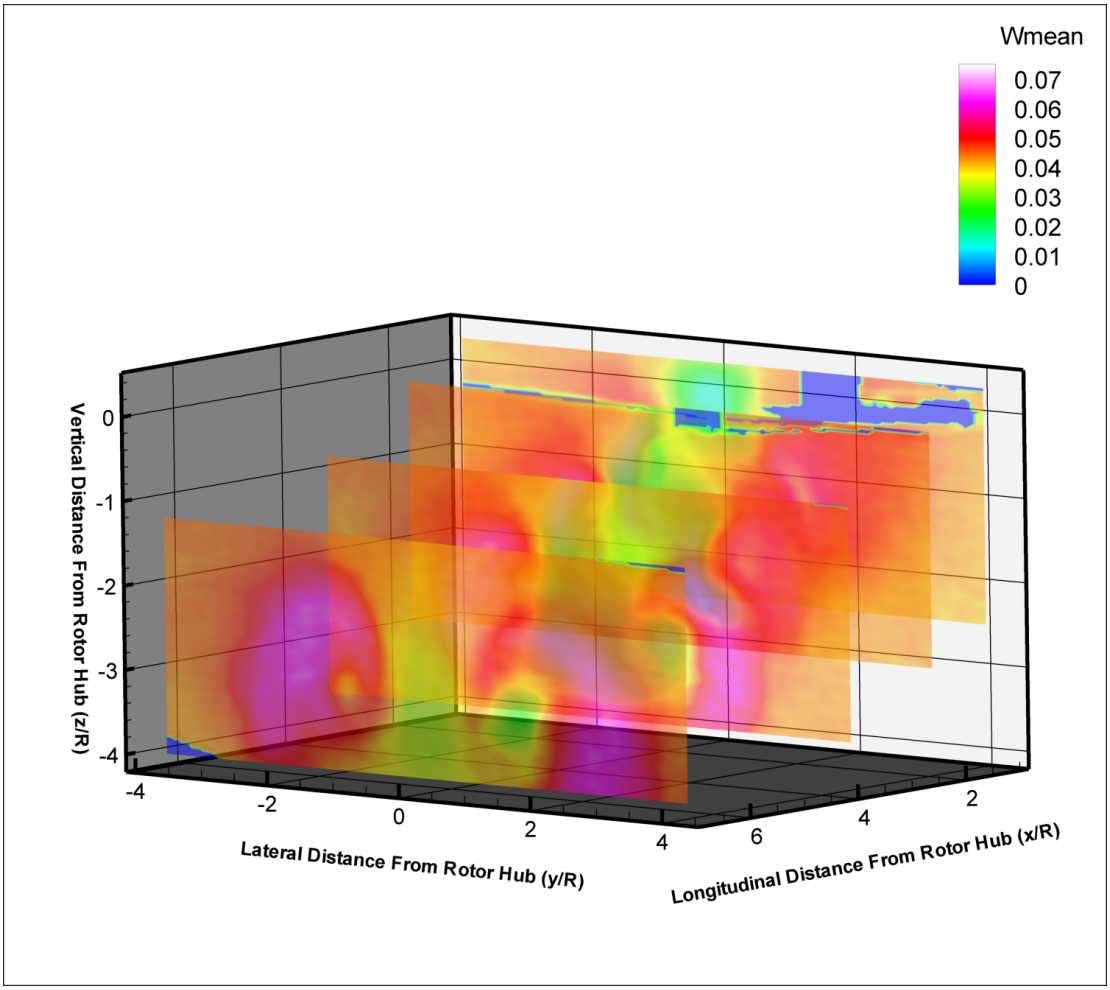

Figure 4.58: Isometric view of the NASA Wind Tunnel PIV images accurately placed in space to help visualize the rotor wake structure for the full-scale WOD 20 case.

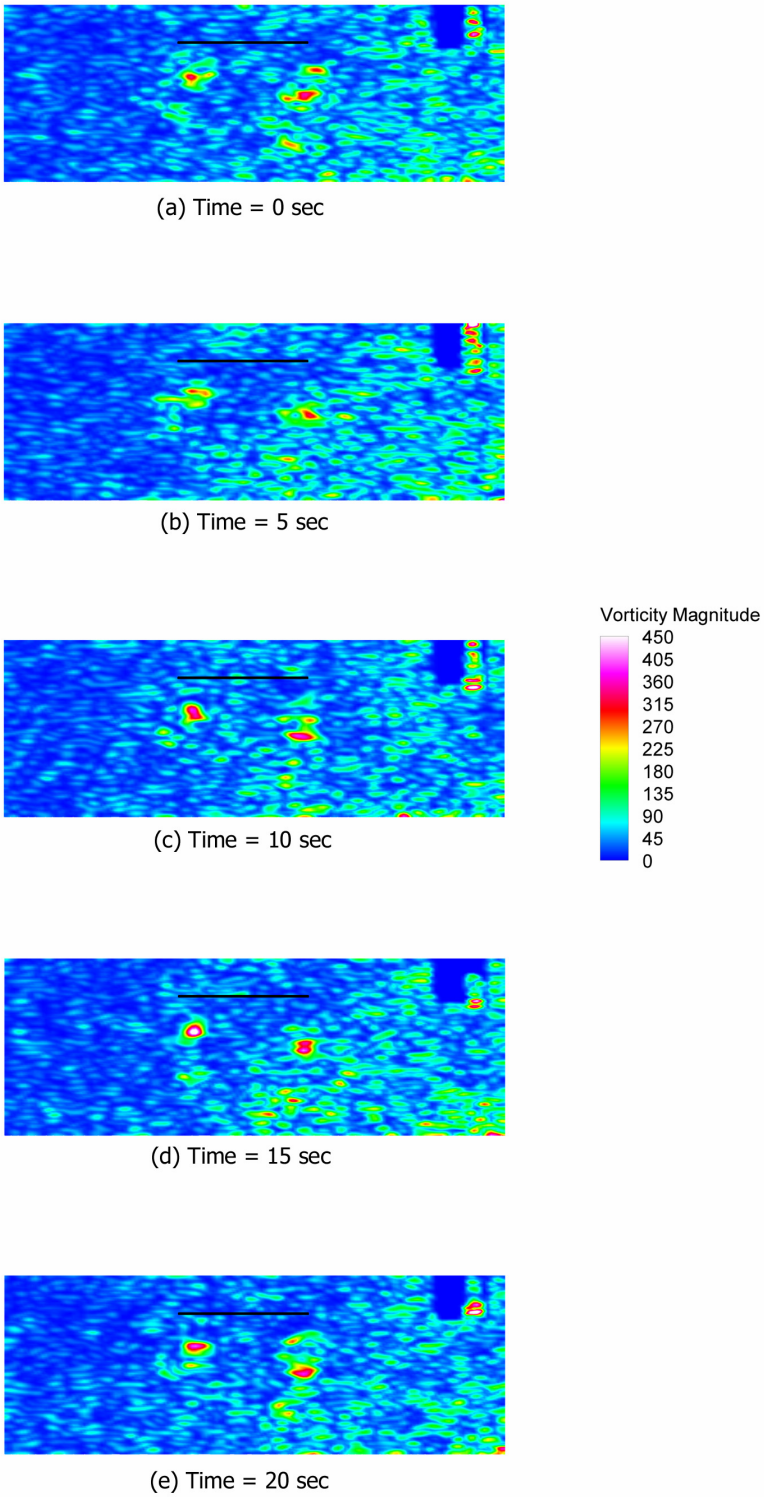

Figure 4.59: Vorticity images calculated from NASA PIV images taken at various times over 20 seconds. Thrust coefficient = 0.009. Advance ratio = 0.0997. Source images captured 3.228 rotor radii downstream of the rotor.

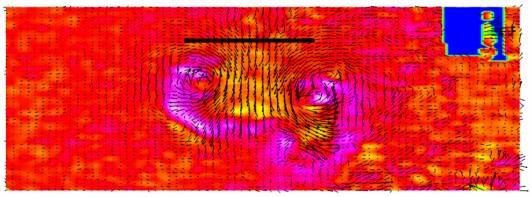

(a) Time = 0 sec

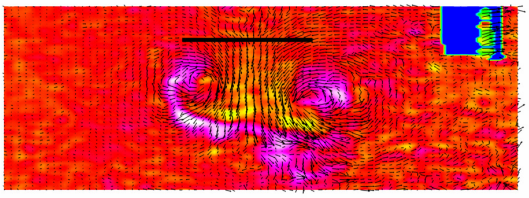

(b) Time = 5 sec

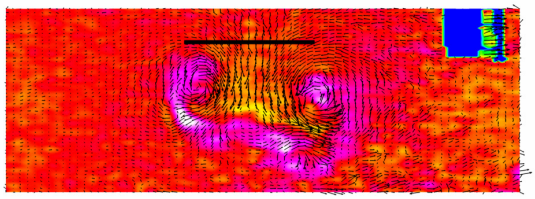

(c) Time = 10 sec

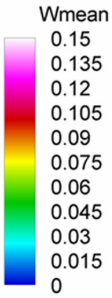

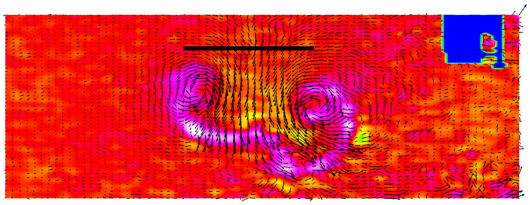

(d) Time = 15 sec

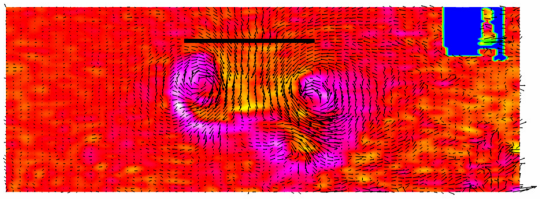

(e) Time = 20 sec

Figure 4.60: Collection of NASA PIV images taken at various times over 20 seconds. Thrust coefficient = 0.009. Advance ratio = 0.0997. PIV images captured 3.228 rotor radii downstream of the rotor.

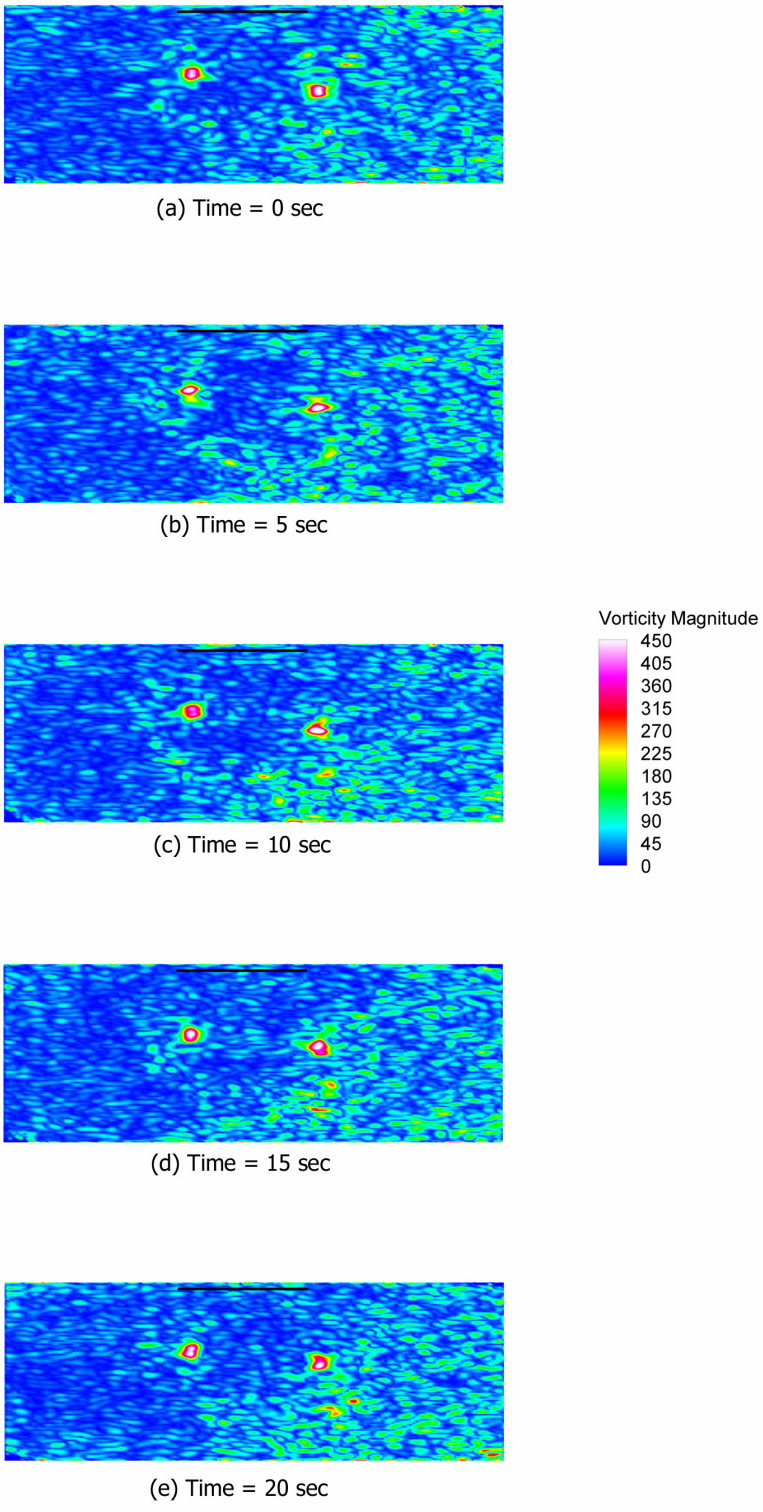

Figure 4.61: Vorticity images calculated from NASA PIV images taken at various times over 20 seconds. Thrust coefficient = 0.009. Advance ratio = 0.0997. Source images captured 5.266 rotor radii downstream of the rotor.

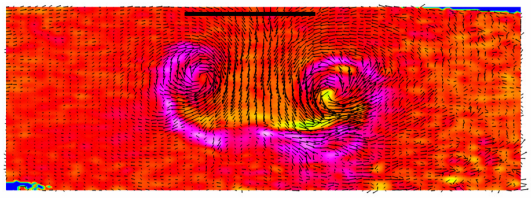

(a) Time = 0 sec

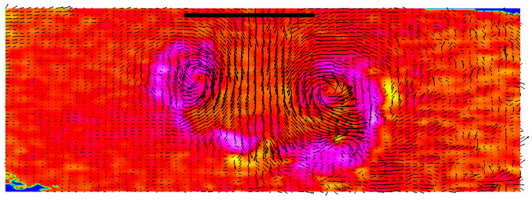

(b) Time = 5 sec

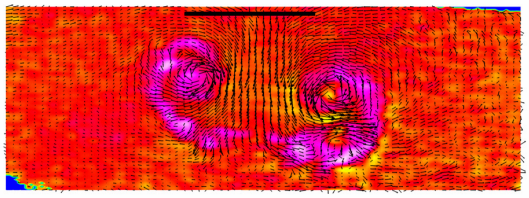

(c) Time = 10 sec

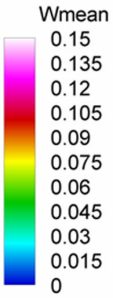

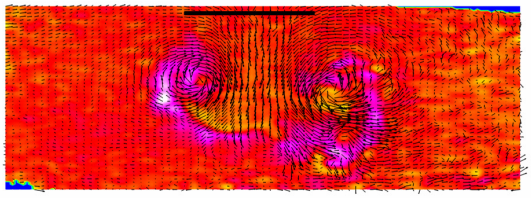

(d) Time = 15 sec

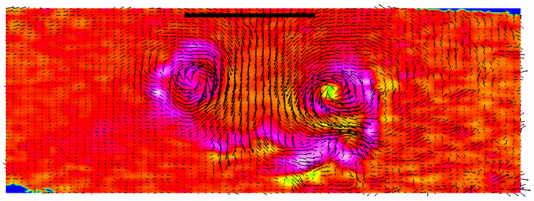

(e) Time = 20 sec

Figure 4.62: Collection of NASA PIV images taken at various times over 20 seconds. Thrust coefficient = 0.009. Advance ratio = 0.0997. PIV images captured 5.266 rotor radii downstream of the rotor.

As shown in this section, advance ratio has a major effect on the wake structure predicted by the MFW code and that visualized from the wind tunnel results. The wind tunnel results show that for this particular sub-scale rotor, advance ratio does change wake skew angle, vortex core size, or the in-plane and out-of-plane velocities at the downstream positions. As seen in Figs. 4.16, 4.31, and 4.58, the wake has an initial skew angle but slowly the angle increases until the wake skew angle is approaching 90 degrees. This behavior is predicted by the MFW code at the higher advance ratios, but at an advance ratio of 0.0997 the mechanism that causes this roll-up and wake skew angle increase breaks down, and the wake, during quiescent periods, has more of a helicoidal structure. The wind tunnel results show that this skew angle increases and wake roll-up still occurs at advance ratios as low as 0.044. In this region, the MFW exhibits large wake aperiodicity and cannot be used to obtain meaningful phase averaged velocity field images. This author's original intention was to use the greater database of points at the advance ratio of 0.066 for the validation effort, but this course had to be abandoned. Instead this author focused on using the Group F points, gathered at the higher advance ratio of 0.0997 as his validation dataset. As discussed previously, at this advance ratio the wake aperiodicity only becomes a problem at distances greater than three rotor radii. This leaves three cases out of eighteen available wind tunnel cases at a thrust coefficient of 0.009 to validate the MFW code.

4.3 Attempts to improve MFW code and the wind tunnel correlation

With the results from the increased blade mass as the baseline configuration, attempts were made to improve the match to the NASA wind tunnel points, with the focus on controlling the aperiodicity in the MFW solution, getting the correct wake skew angle, and scaling down the large negative out-of-plane flow velocities between the vortices. Using the wake geometry files from the case presented in Figs. 4.42 and 4.43, velocity field images were generated for three locations downstream of the rotor hub: 1.114, 2.1267 and 3.228 rotor radii. The final 25 iterations were averaged to obtain the images contained in Figs. 4.63 through 4.65. At 1.1139 rotor radii downstream all components of velocity are predicted well but at subsequent positions they are over predicted. In Fig. 4.65 the vertical position of both vortices does not correlate well with the wind tunnel results presented in Fig. 4.27.

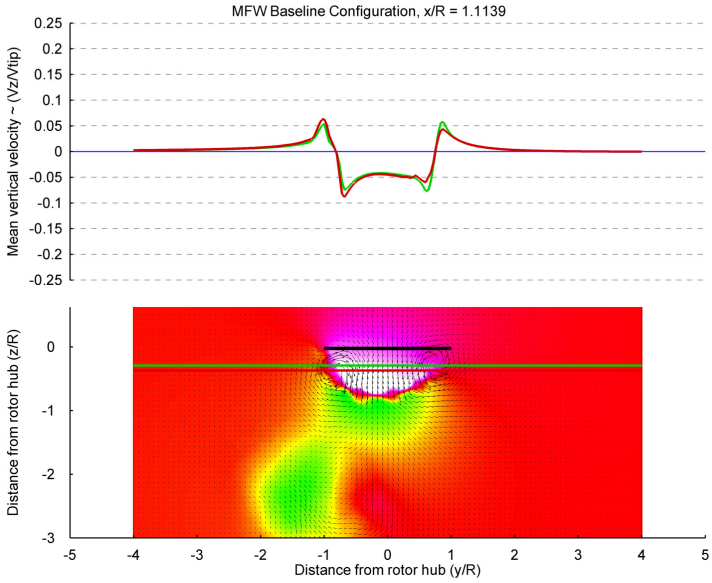

Figure 4.63: MFW PIV image at 1.114 rotor radii for the baseline configuration at an advance ratio = 0.0997.

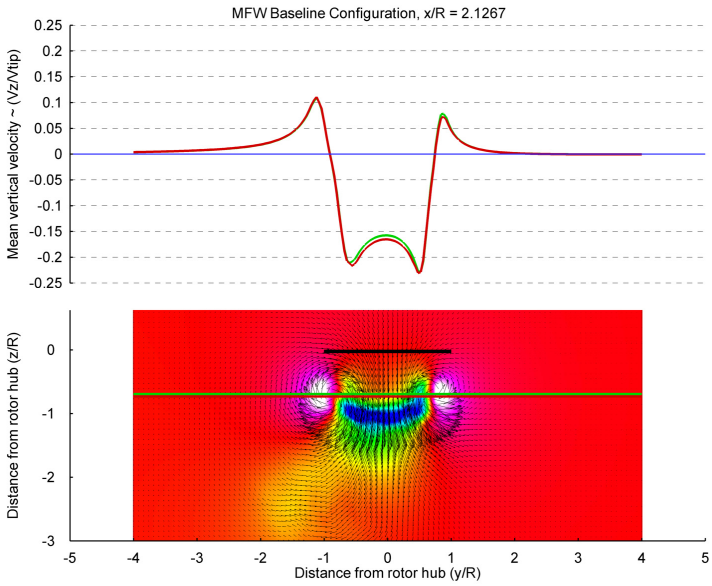

Figure 4.64: MFW PIV image at 2.1267 rotor radii for the baseline configuration at an advance ratio = 0.0997.

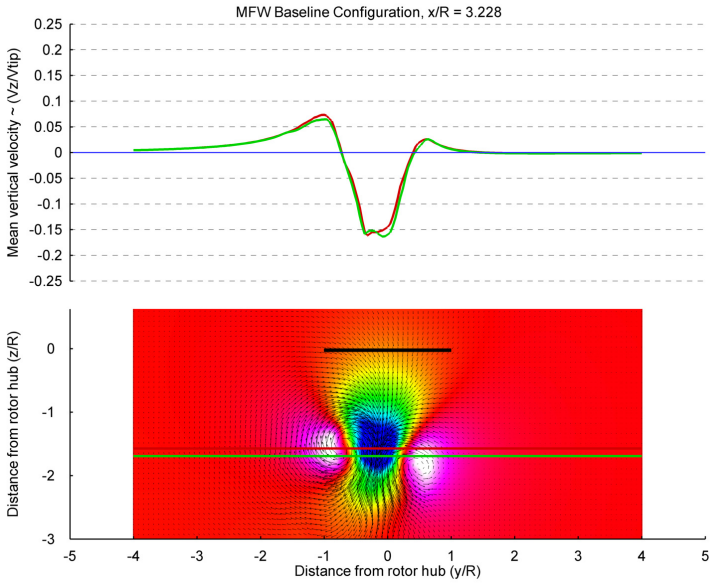

Figure 4.65: MFW PIV image at 3.228 rotor radii for the baseline configuration at an advance ratio = 0.0997.

One of the modifications attempted was to allow the blade to undergo flapping motion. Since the start of this effort every attempt was made to mimic the sub-scale rotor parameters as closely as possible. It was postulated that keeping the rotor from

flapping could be one contributor to the aperiodicity noted in the wake solutions. The input file parameters for this case are contained in Table 4.9. As noted in the table, the flap spring value was set to zero, the flap hinge location used was that from the H-60 full-scale verification case, and the twist was the correct model value. After running the cases presented previously, it was realized that the wrong blade twist was being used. It is believed that the approximately five degree error does not affect the results because the rotor was trimmed to a given thrust coefficient, so the MFW program would simply trim to a different collective for the different twist. And as mentioned previously, the main drivers of the far wake structure were advance ratio and thrust coefficient so the different twist should have a small effect at low advance ratios. The wake geometry images are contained in Figs. 4.66 and 4.67 while the averaged velocity field images are contained in Figs. 4.68 through 4.70.

Table 4.8: Input file parameters for the "free to flap" MFW case.

flight.input	
Paramter	Value
mu	0.0997
muc	0.0
pbar	0.0
qbar	0.0
ct0	0.00901
t0_0	14.0
t1c0	0
t1s0	0
b0_0	2.75362
b1c0	0
b1s0	0
cttol	1.0e-8
fltol	1.0e-8
altitude	0.0

(a)

geometry.input	
Paramter	Value
nr	1
nb	5
ns	32
asr0	0.0
rad	0.25083
flph	0.046
rcout	0.324
crd	0.02819
twt	-15.9
om	320.77
taperst	1.1
taper	0.0
rotgeo	0

(b)

rotprop.input	
Paramter	Value
bmass	0.83724
kbeta	0.0
betap	0.0

(c)

user.input	
Paramter	Value
nw	1
pw	0
nfw	200
nk	1
ft	10
bct	2
dp	12
dz	12
rcb	0.05
dcy	0.0002
trm	y
lin	0.0
li	0.0
method	t
initial	n

(d)

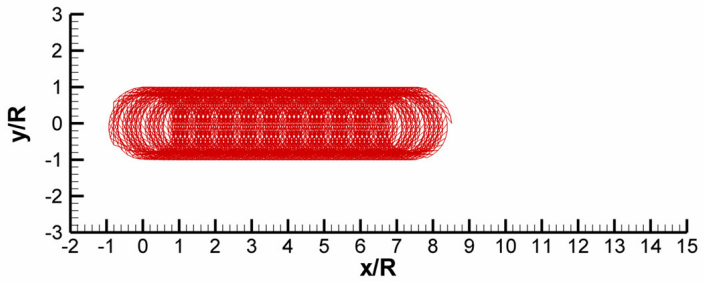

(a) Iteration = 0

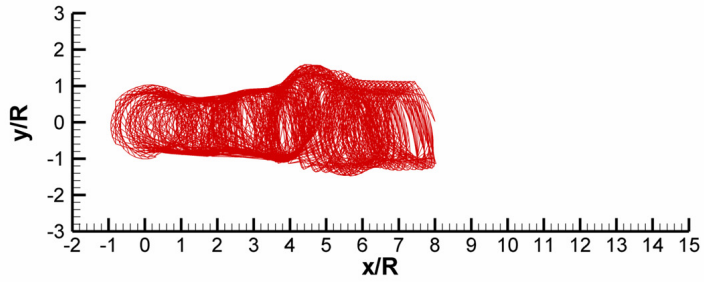

(b) Iteration = 50

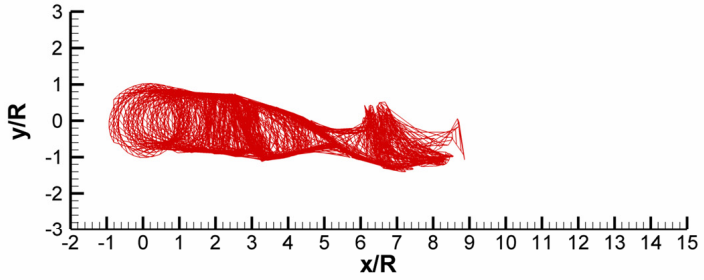

(c) Iteration = 100

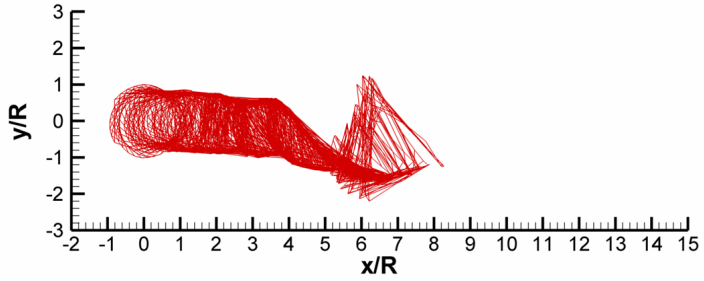

(d) Iteration = 200

Figure 4.66: MFW code generated wake geometry visualization for an advance ratio = 0.0997. Free to flap solution. Top view.

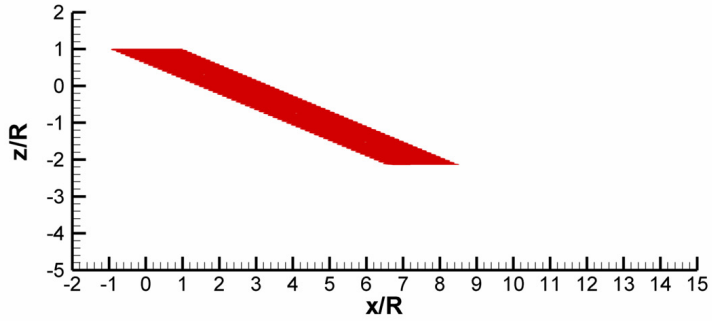

(a) Iteration = 0

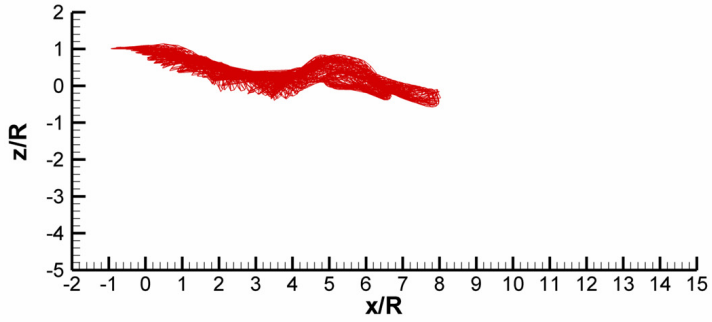

(b) Iteration = 50

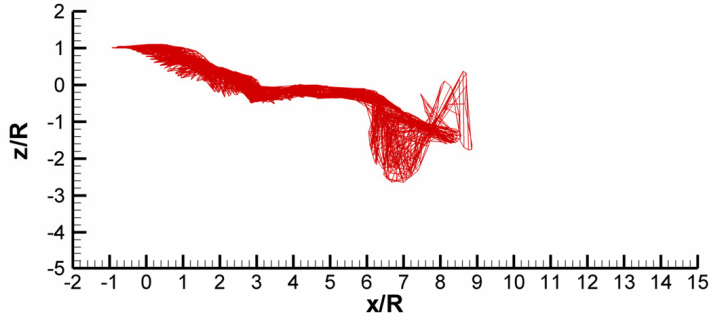

(c) Iteration = 100

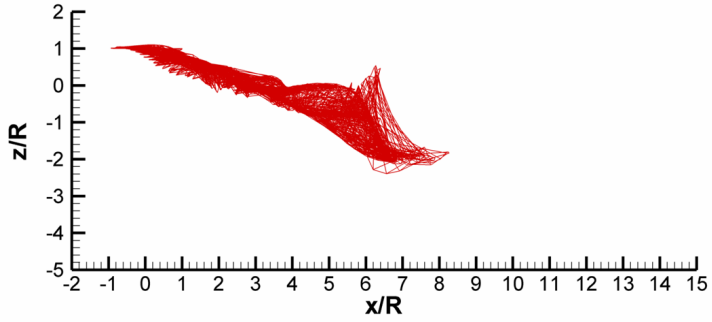

(d) Iteration = 200

Figure 4.67: MFW code generated wake geometry visualization for an advance ratio = 0.0997. Free to flap solution. Side view.

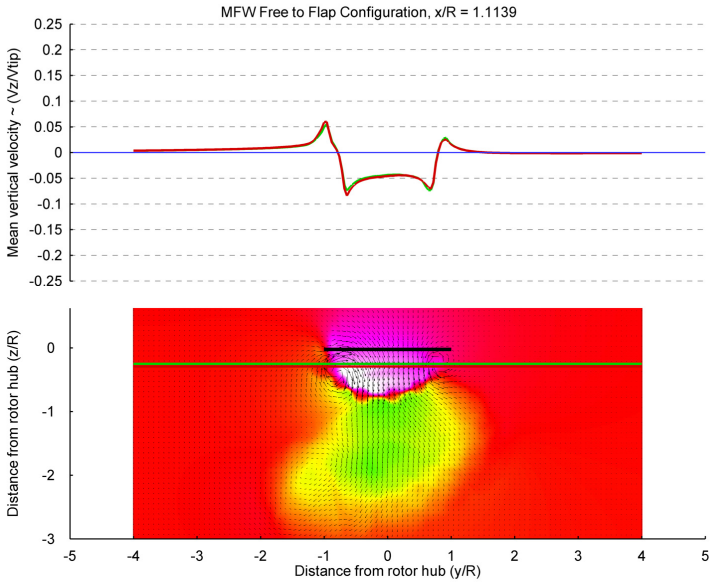

Figure 4.68: MFW PIV image at 1.1139 rotor radii for the "free to flap" configuration at an advance ratio = 0.0997.

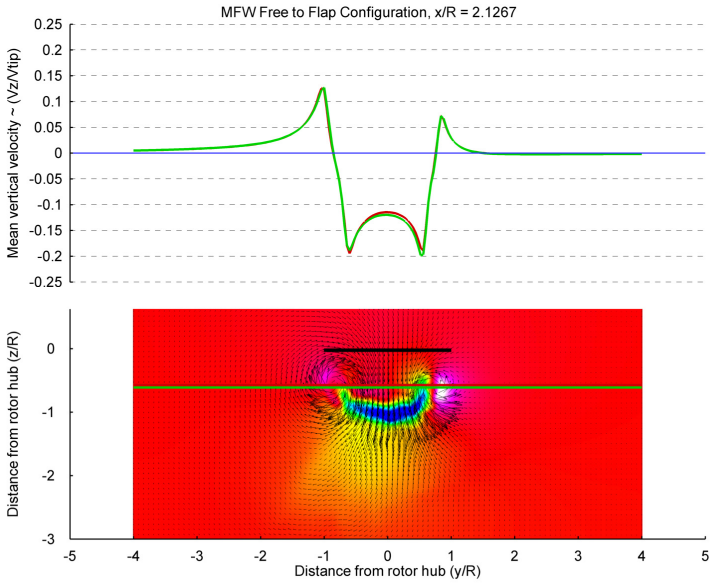

Figure 4.69:MFW PIV image at 2.1267 rotor radii for the "free to flap" configuration at an advance ratio = 0.0997.

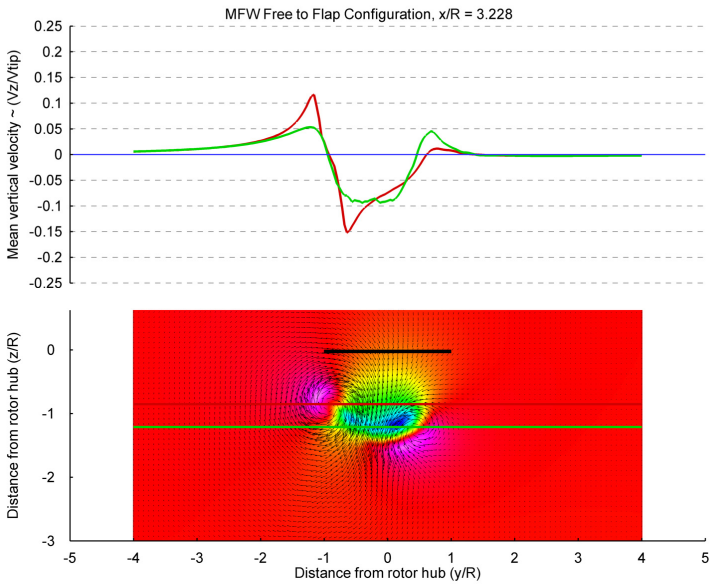

Figure 4.70: MFW PIV image at 3.228 rotor radii for the "free to flap" configuration at an advance ratio = 0.0997.

The effect of changing the rotor from a teetering rotor, as it was for the increased rotor mass advance ratio sweep, to that of a rotor with a flap hinge spring stiffness corresponding to a full-scale H-60 is noticeable. The rotor wake, as shown in Figs. 4.66 and 4.67 seems less prone to large magnitude aperiodicity. The far wake still contracts, as shown in Fig. 4.66(c) and (d), but it occurs farther downstream. The magnitude of the aperiodicity is reduced as well. However the velocity field images do not correlate well with the baseline case. The starboard vortex swirl velocity in Fig. 4.68 is reduced from that in Fig. 4.63 further degrading the correlation to the wind tunnel data contained in Fig. 4.25. However the port vortex swirl velocity remains relatively unchanged from the baseline configuration. For the plane 2.1267 rotor radii downstream, the “free to flap” case as shown in Fig. 4.69 has reduced out-of-plane velocity compared to Fig. 4.64 but both MFW generated images show a negative flow region between the rotors. The image from the wind tunnel contained in Fig. 4.26, shows that the flow is actually accelerated between the two vortices.

The port vortex position and size shown in Fig. 4.69 correlates well with wind tunnel results but the swirl velocities are still over predicted. The results presented in Fig. 4.70 show a poorly formed starboard vortex. This is more than likely due to the aperiodicity of the flow adversely affecting the phase averaged velocity field solution. The port vortex bundle swirl velocity remains over predicted, when compared to Fig. 4.27. While the wake aperiodicity has been reduced, the velocity field results aren't overall improved over those of the baseline configuration.

Since a full-scale flap hinge location was used, the effects of changing the location to one more representative of the sub-scale model wind tunnel test, was examined. The input file parameters for this flap hinge sensitivity run are presented in Table 4.10. The wake geometry images are shown in Figs. 4.71 and 4.72 while the velocity field images are contained in Figs. 4.73 through 4.75.

Table 4.9: Input file parameters for the flap hinge sensitivity evaluation.

flight.input	
Paramter	Value
mu	0.0997
muc	0.0
pbar	0.0
qbar	0.0
ct0	0.00901
t0_0	14.0
t1c0	0
t1s0	0
b0_0	2.75362
b1c0	0
b1s0	0
cttol	1.0e-8
fltol	1.0e-8
altitude	0.0

(a)

geometry.input	
Paramter	Value
nr	1
nb	5
ns	32
asr0	0.0
rad	0.25083
flph	0.150
rcout	0.324
crd	0.02819
twt	-15.9
om	320.77
taperst	1.1
taper	0.0
rotgeo	0

(b)

rotprop.input	
Paramter	Value
bmass	0.83724
kbeta	0.0
betap	0.0

(c)

user.input	
Paramter	Value
nw	1
pw	0
nfw	200
nk	1
ft	10
bct	2
dp	12
dz	12
rcb	0.05
dcy	0.0002
trm	y
lin	0.0
li	0.0
method	t
initial	n

(d)

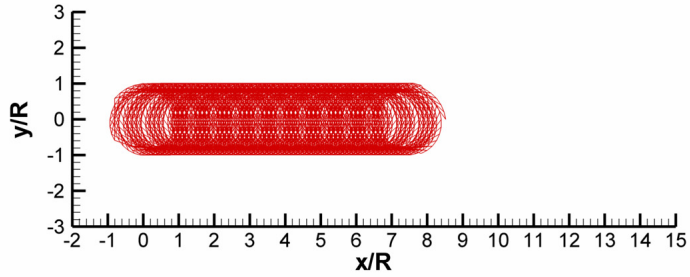

(a) Iteration = 0

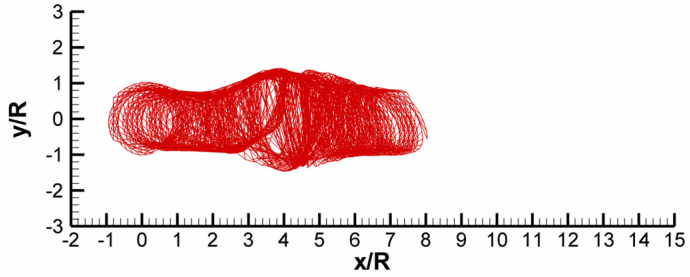

(b) Iteration = 50

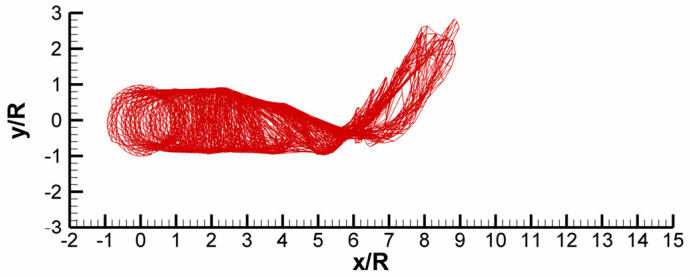

(c) Iteration = 100

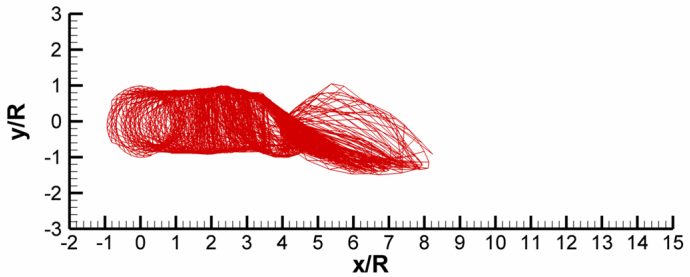

(d) Iteration = 200

Figure 4.71: MFW code generated wake geometry visualization for an advance ratio = 0.0997. Flap hinge change solution. Top view.

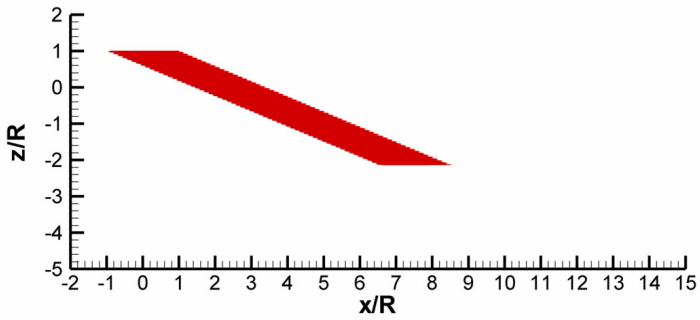

(a) Iteration = 0

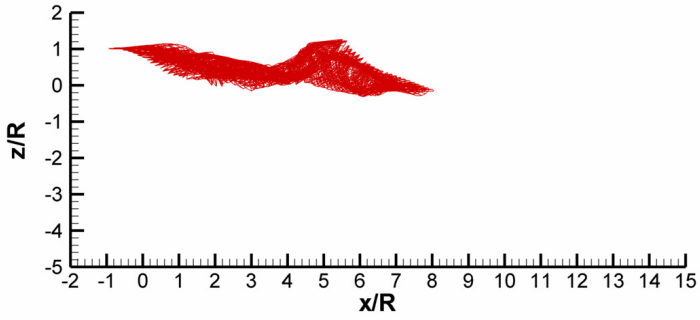

(b) Iteration = 50

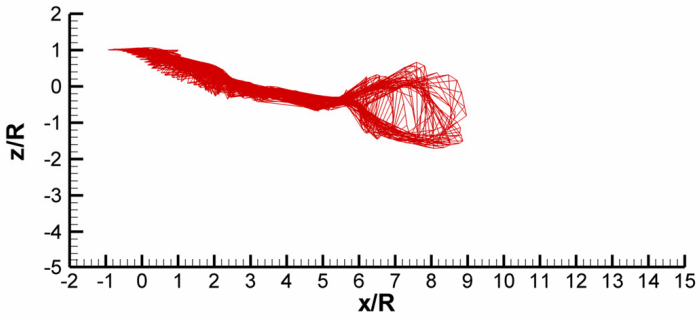

(c) Iteration = 100

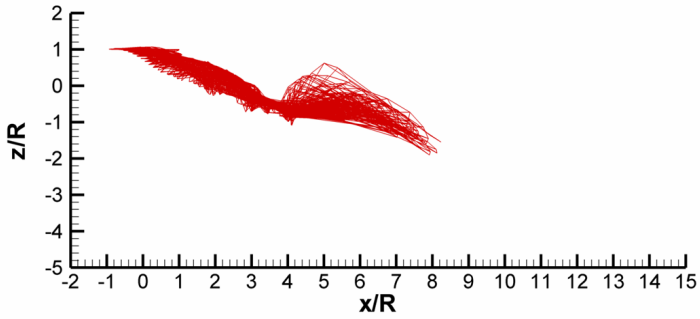

(d) Iteration = 200

Figure 4.72: MFW code generated wake geometry visualization for an advance ratio = 0.0997. Flap hinge change solution. Side view.

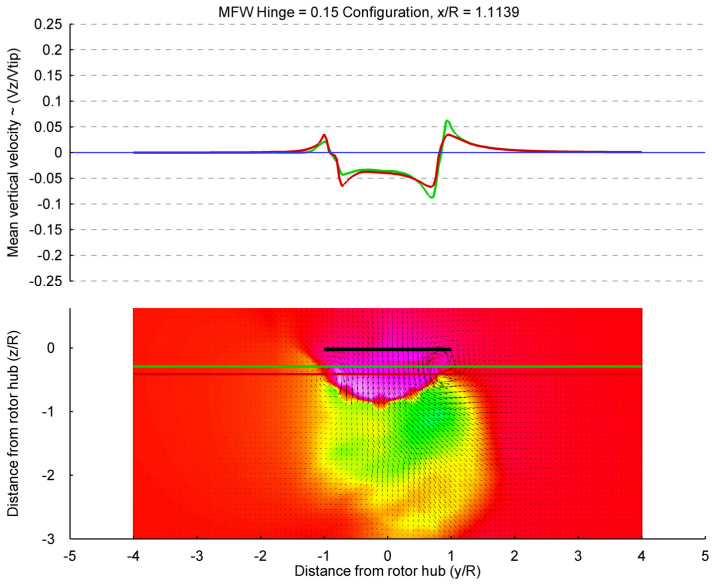

Figure 4.73: MFW PIV image at 1.1139 rotor radii for the "flap hinge farther outboard" configuration at an advance ratio = 0.0997.

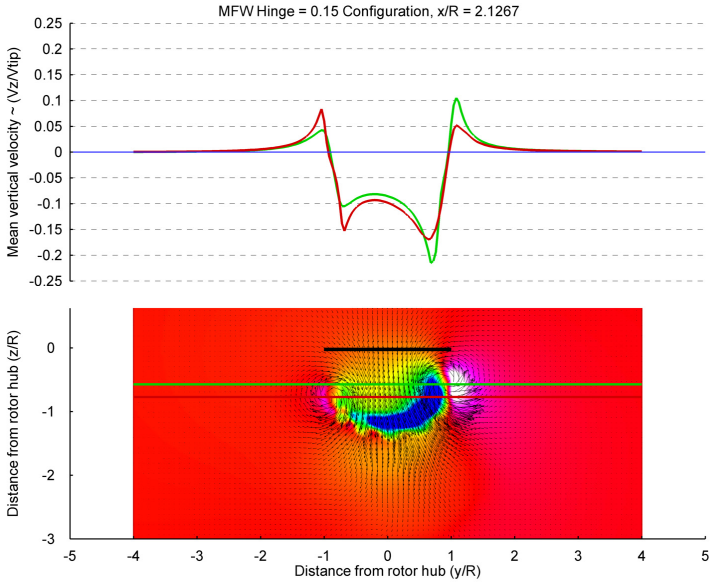

Figure 4.74: MFW PIV image at 2.1267 rotor radii for the "flap hinge farther outboard" configuration at an advance ratio = 0.0997.

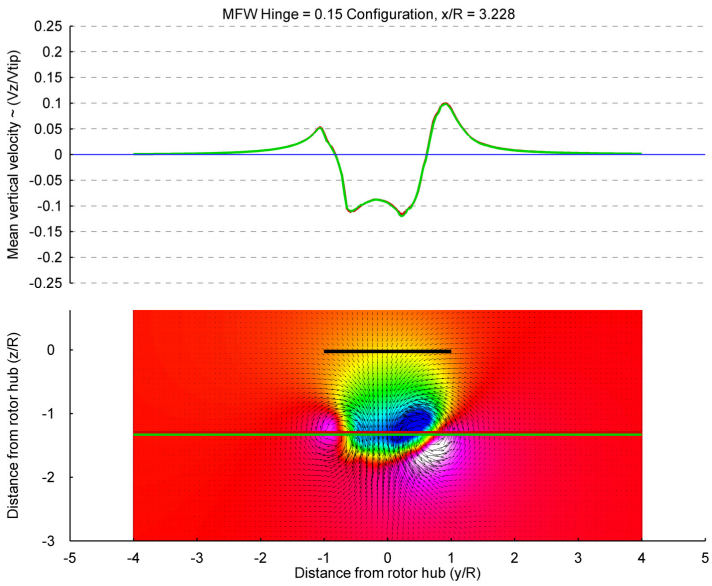

Figure 4.75: MFW PIV image at 3.228 rotor radii for the "flap hinge farther outboard" configuration at an advance ratio = 0.0997.

As shown in Figs. 4.71 and 4.72, the wake geometry remains relatively unchanged from the baseline configuration. The wake still exhibits aperiodic tendencies beyond roughly three rotor radii downstream making any predictions beyond this point impossible. The velocity fields, shown in Figs. 4.73 through 4.75, exhibit much of the same characteristics of the “free to flap” configuration shown in Figs. 4.68 – 4.70. There are differences however. The results shown in Figs. 4.74 and 4.75 predict a very asymmetric wake structure, especially at greater downstream distances. The area and magnitude of negative flow between the vortices has grown compared to Figs. 4.68 through 4.70. In this case, it appears that changing the flap hinge location, bringing it farther outboard, has increased the magnitude of the out-of-plane velocities compared to the “free to flap” case but comparing Fig. 4.74 with Fig. 4.26, a reduction in swirl velocity can be seen.

The last parameter changed in an effort to improve the correlation to wind tunnel was the wake growth parameter. This parameter, graphically represented in

Fig. 3.5 is hard to define exactly. As seen in Fig. 3.5, the there is substantial scatter in the data at the lower vortex Reynolds numbers. For the sub-scale wind test, the vortex Reynolds number was 15,000 while the full-scale value was 1,500,000. While a case can be made for setting the value of a_1 to 0.0002 for a full-scale test, that value may not be appropriate for the vortex Reynolds numbers encountered during the NASA sub-scale tests used to validate the MFW code. A new value of 0.002 was chosen for a_1. Two cases, one at an advance ratio of 0.066 and the other at 0.0997, were run with the new value for a_1. The input file parameters used for these two cases are shown in Table 4.11.

Table 4.10: Input file parameters for the dcy = 0.002 evaluation.

flight.input	
Paramter	Value
mu	Variable
muc	0.0
pbar	0.0
qbar	0.0
ct0	0.00901
t0_0	14.0
t1c0	0
t1s0	0
b0_0	2.75362
b1c0	0
b1s0	0
cttol	1.0e-8
fltol	1.0e-8
altitude	0.0

(a)

geometry.input	
Paramter	Value
nr	1
nb	5
ns	32
asr0	0.0
rad	0.25083
flph	0.046
rcout	0.324
crd	0.02819
twt	-15.9
om	320.77
taperst	1.1
taper	0.0
rotgeo	0

(b)

rotprop.input	
Paramter	Value
bmass	0.83724
kbeta	0.0
betap	0.0

(c)

user.input	
Paramter	Value
nw	1
pw	0
nfw	200
nk	1
ft	10
bct	2
dp	12
dz	12
rcb	0.05
dcy	0.002
trm	y
lin	0.0
li	0.0
method	t
initial	n

(d)

The wake geometry images can be seen in Figs. 4.76 through 4.78. As seen in Figs. 4.76 and 4.77, the results from the lower advance ratio were not improved over the baseline low advance ratio cases, displayed in Figs. 4.46 through 4.52, so averaged velocity field images were not generated. Velocity field images for the

higher advance ratio case at the three points downstream were generated though, and are presented in Figs. 4.80 through 4.82.

For the higher advance ratio case presented in Figs. 4.78 and 4.79, the wake exhibits far less aperiodicity than the baseline case, shown in Figs. 4.42 and 4.43. The wake also more closely resembles the higher advance ratio cases where the wake skew angle increases two to three rotor radii downstream of the rotor, approaching 90 degrees. The velocity field images are also improved over the baseline configuration. The size and strength of the reverse flow region and the vortex vertical position and size, more closely match the wind tunnel results, contained in Figs. 4.25 through 4.27. However the swirl velocities of the port and starboard vortices at each position investigated are under predicted by the MFW code. The vortex core radius, and the rate at which it grows, is over predicted by the MFW code, when compared to wind tunnel results.

Attempts to improve the correlation to the wind tunnel results using rotor geometry variable changes were not entirely successful. Little to no improvement in the wake geometry was realized by allowing the blade to flap, with both the H-60 full-scale flap hinge location and one farther outboard. However, changing the wake growth parameter, to a value potentially more appropriate for the extremely low vortex Reynolds number encountered for the wind tunnel test, did yield improved results over the baseline case. This finding offers supporting evidence that the aperiodicity and other wake characteristics observed for the cases examined in the MFW code could be the result of Reynolds number scaling effects. In addition to the

scaling effects, the inability to exactly match the wind tunnel rotor configuration within the MFW code adversely affected the results.

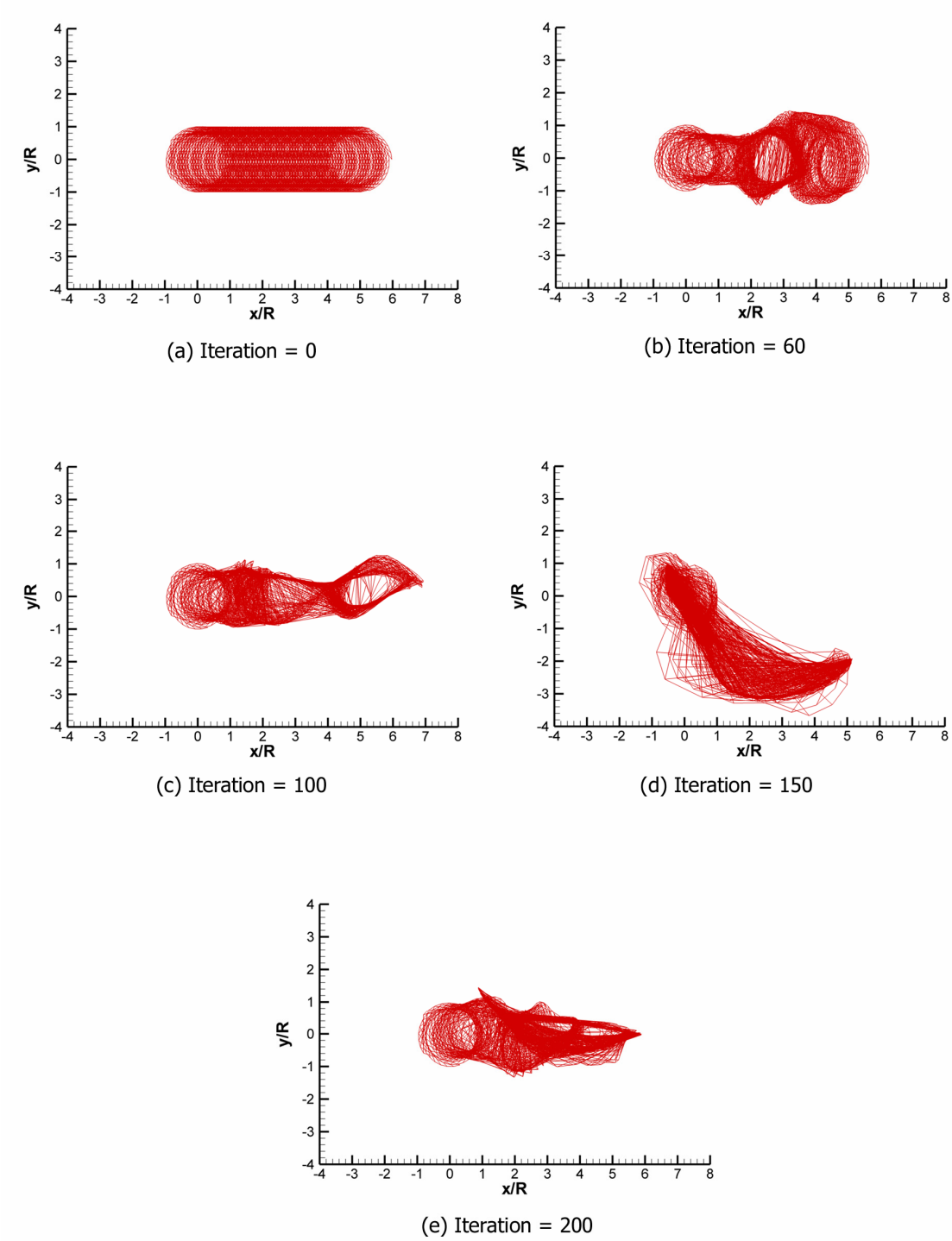

Figure 4.76: MFW code generated wake geometry visualization for an advance ratio = 0.066. Wake growth parameter change solution. Top view.

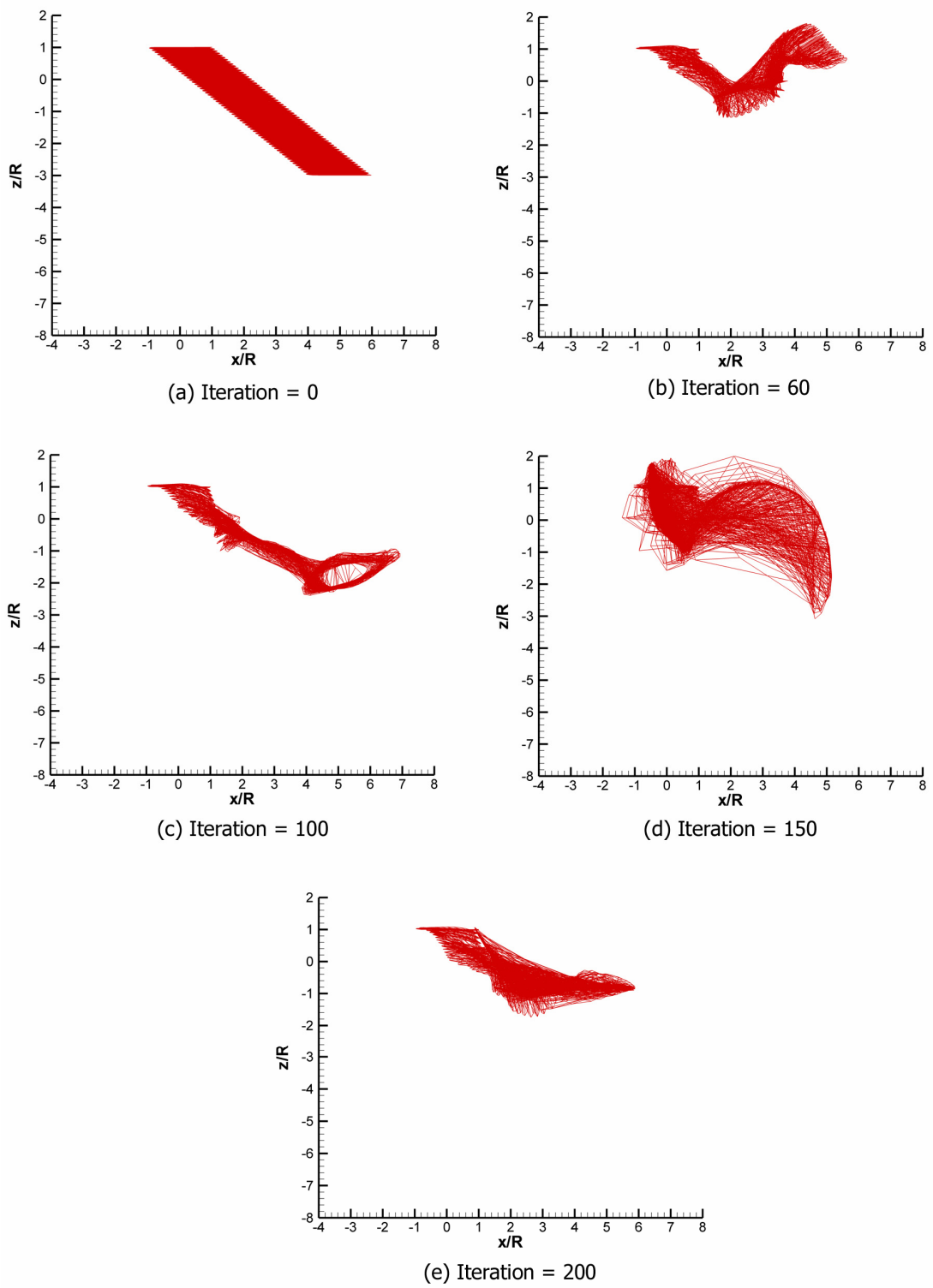

Figure 4.77: MFW code generated wake geometry visualization for an advance ratio = 0.066. Wake growth parameter change solution. Side view.

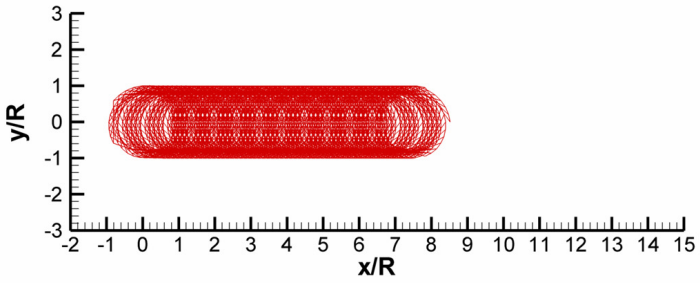

(a) Iteration = 0

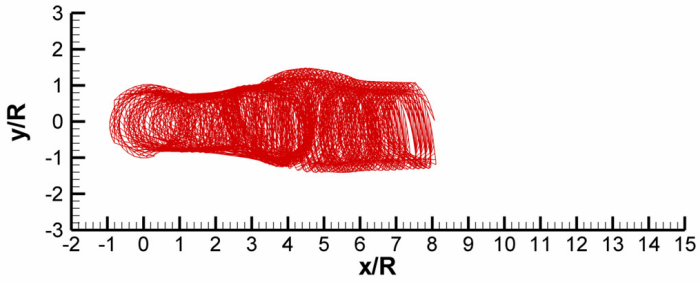

(b) Iteration = 50

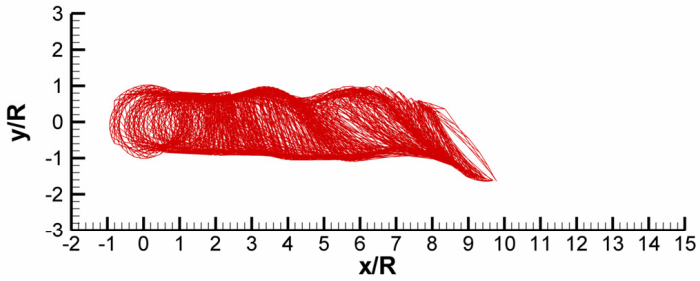

(c) Iteration = 100

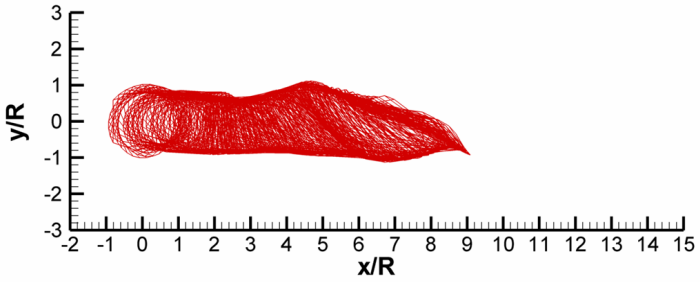

(d) Iteration = 200

Figure 4.78: MFW code generated wake geometry visualization for an advance ratio = 0.0997. Wake growth parameter change solution. Top view.

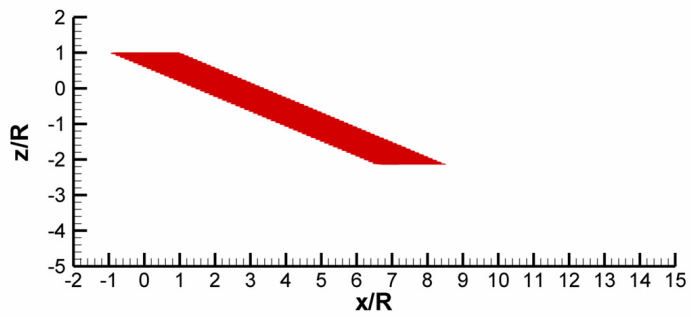

(a) Iteration = 0

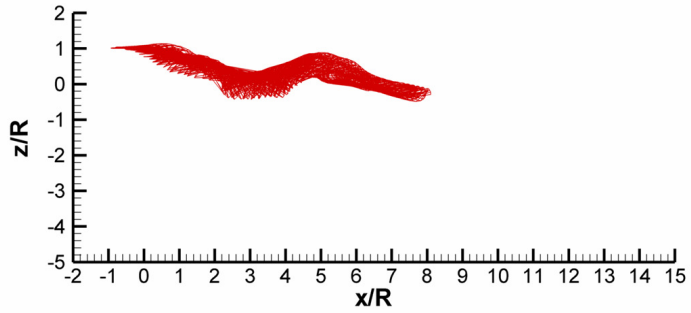

(b) Iteration = 50

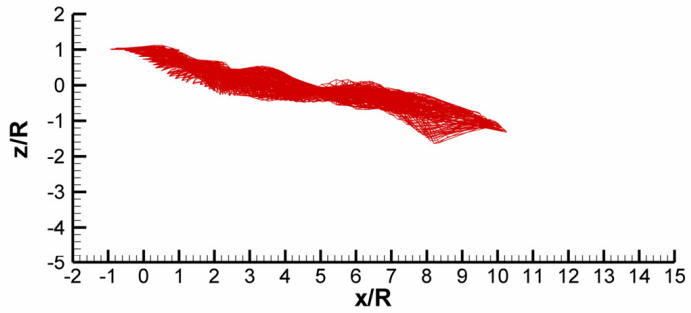

(c) Iteration = 100

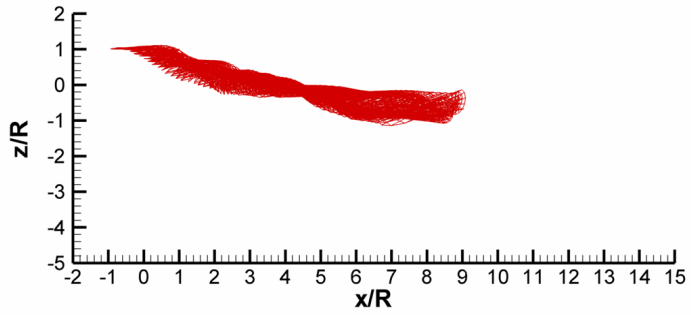

(d) Iteration = 200

Figure 4.79: MFW code generated wake geometry visualization for an advance ratio = 0.0997. Wake growth parameter change solution. Side view.

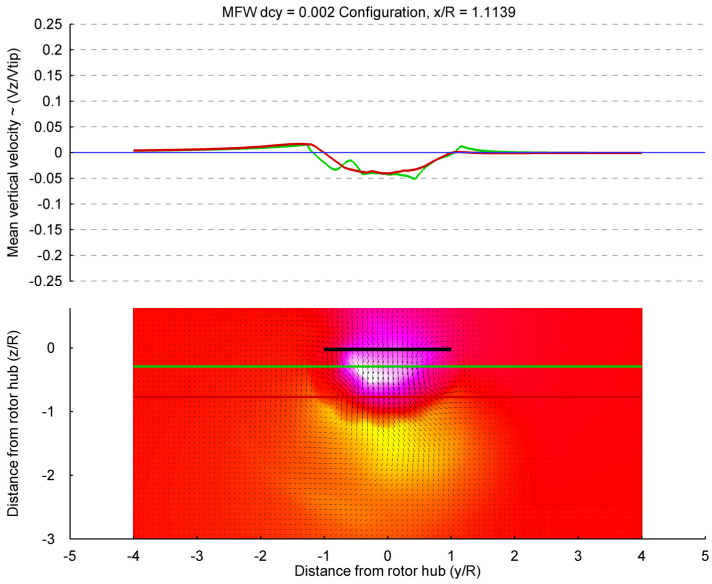

Figure 4.80: MFW PIV image at 1.1139 rotor radii for the "wake growth parameter change" configuration at an advance ratio = 0.0997.

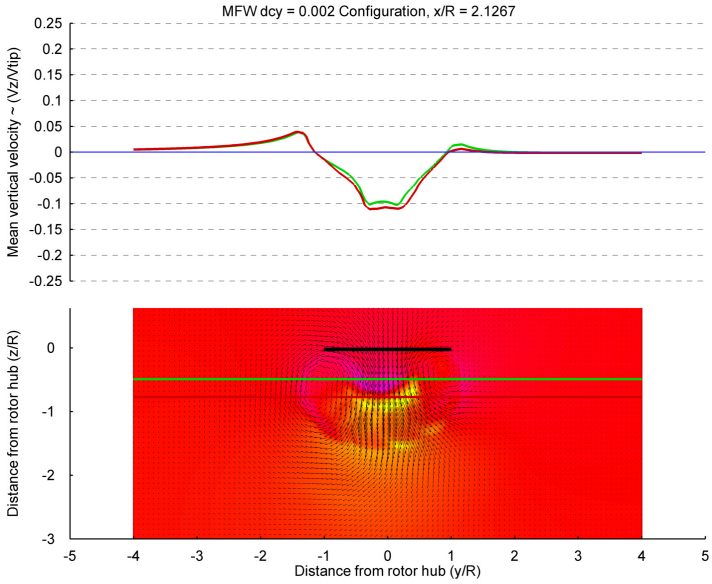

Figure 4.81: MFW PIV image at 2.1267 rotor radii for the "wake growth parameter change" configuration at an advance ratio = 0.0997.

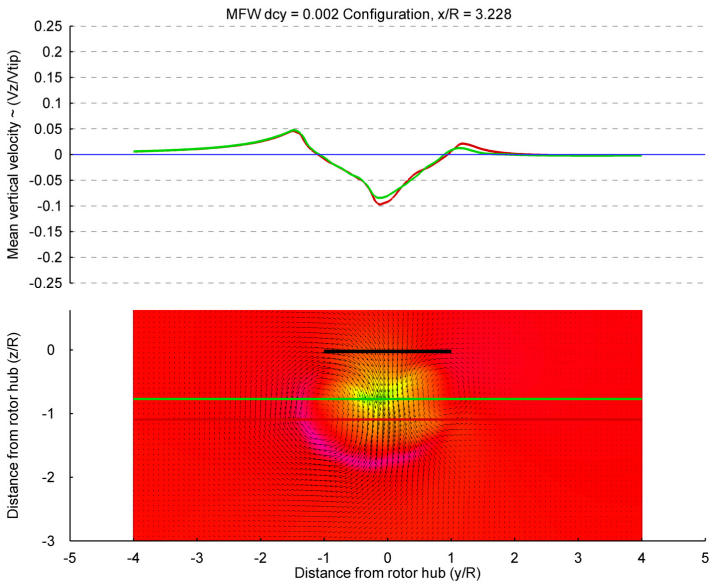

Figure 4.82: MFW PIV image at 3.228 rotor radii for the "wake growth parameter change" configuration at an advance ratio = 0.0997.

While the wake growth parameter was the last one to be changed in an attempt to reduce the wake aperiodicity, one more area deserved investigation. It was theorized that the filament strain could be a primary contributor to the observed wake aperiodicity. As mentioned earlier, as filaments are deformed, their vorticity changes and it is this change that could affect the solution. As seen in Figs. 4.83 and 4.84, removing filament strain from the calculation does not greatly improve the correlation. In Figs. 4.85 through 4.87 the vortex core radius is plotted for all five blades. In these figures, the strain has been turned on. For Fig. 4.88, the strain has been turned off and the core radius from all five blades is identical. Figures 4.83 through 4.88 show that while turning strain off does have a significant effect on core radius growth, it does not greatly affect the aperiodicity observed in the wake solution.

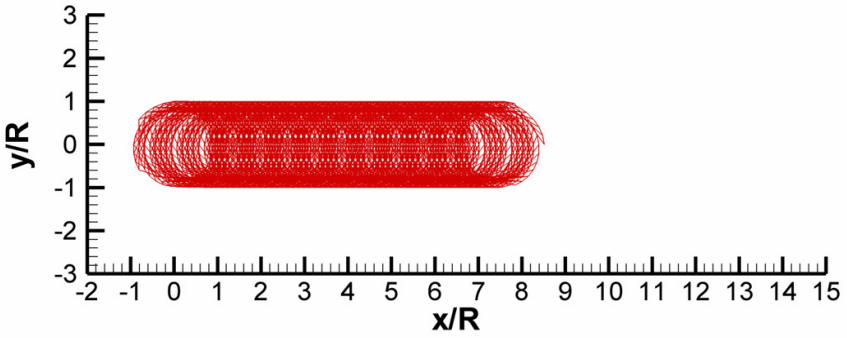

(a) Iteration = 0

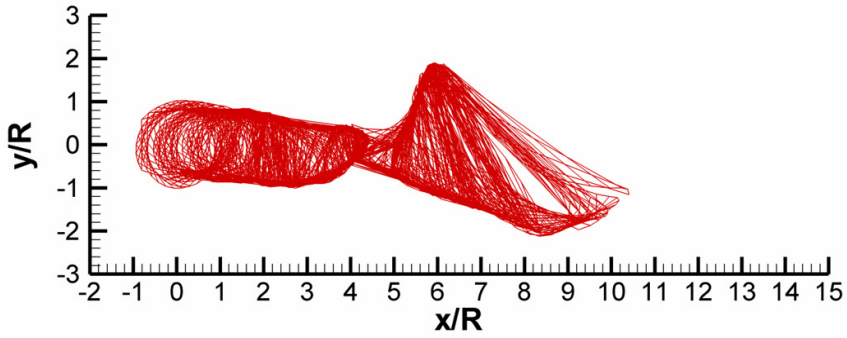

(b) Iteration = 75

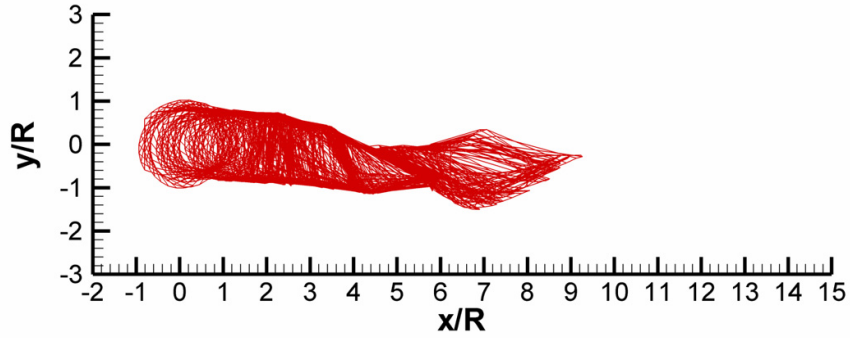

(c) Iteration = 150

Figure 4.83:Top view of the Strain Off case

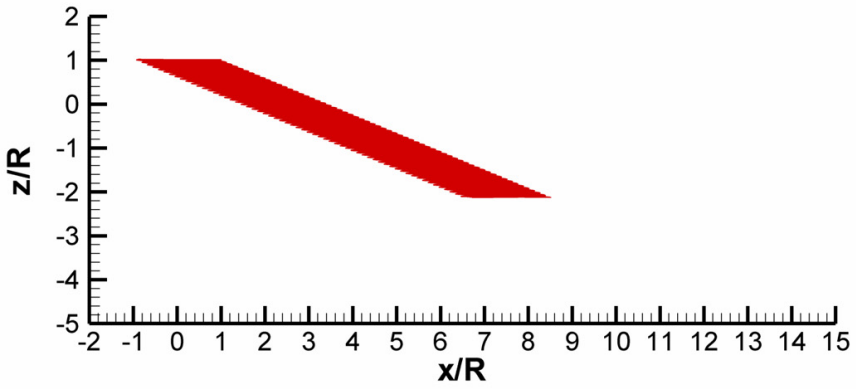

(a) Iteration = 0

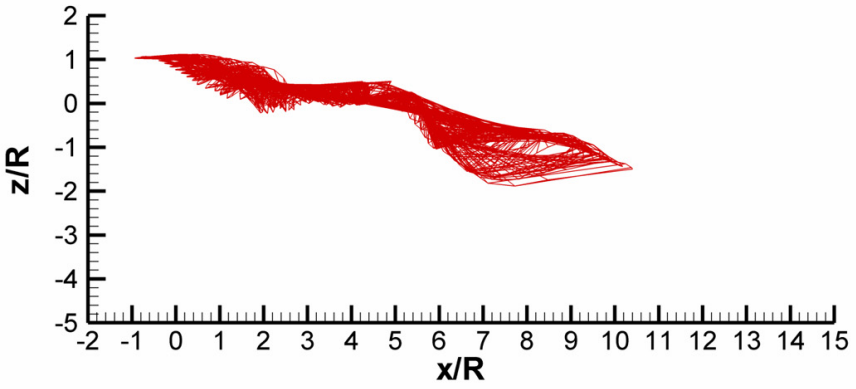

(b) Iteration = 75

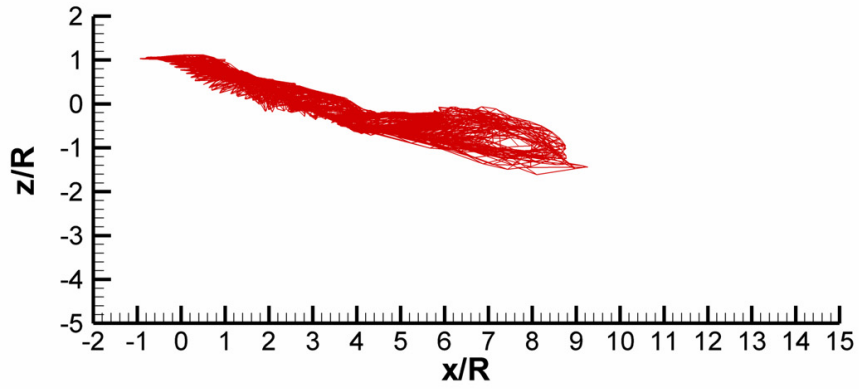

(c) Iteration = 150

Figure 4.84: Side view of the Strain Off case

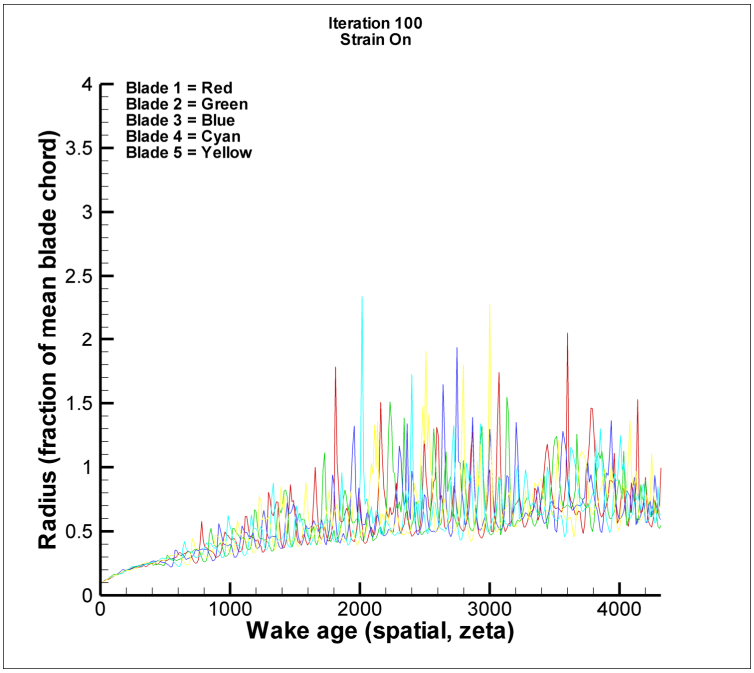

Figure 4.85: Core radius for Iteration 100

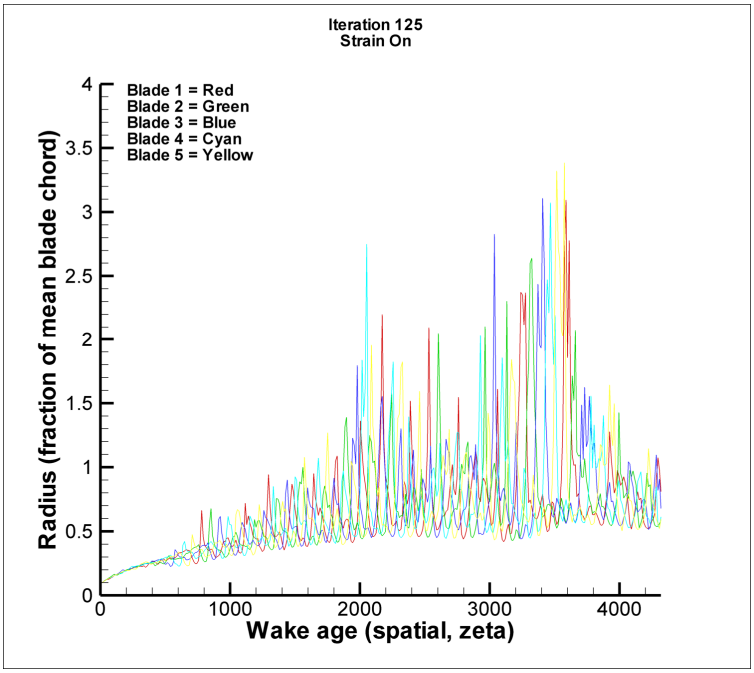

Figure 4.86: Core radius for Iteration 125

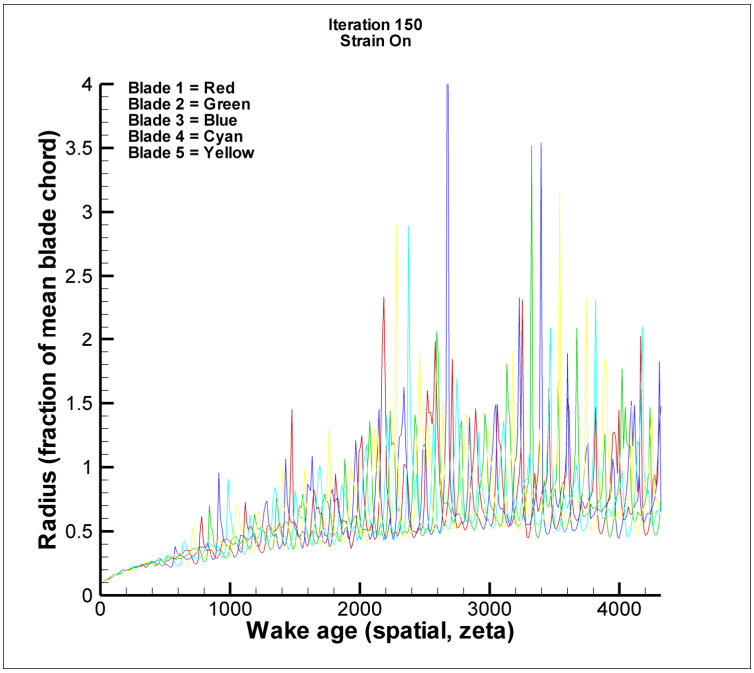

Figure 4.87: Core radius for Iteration 100

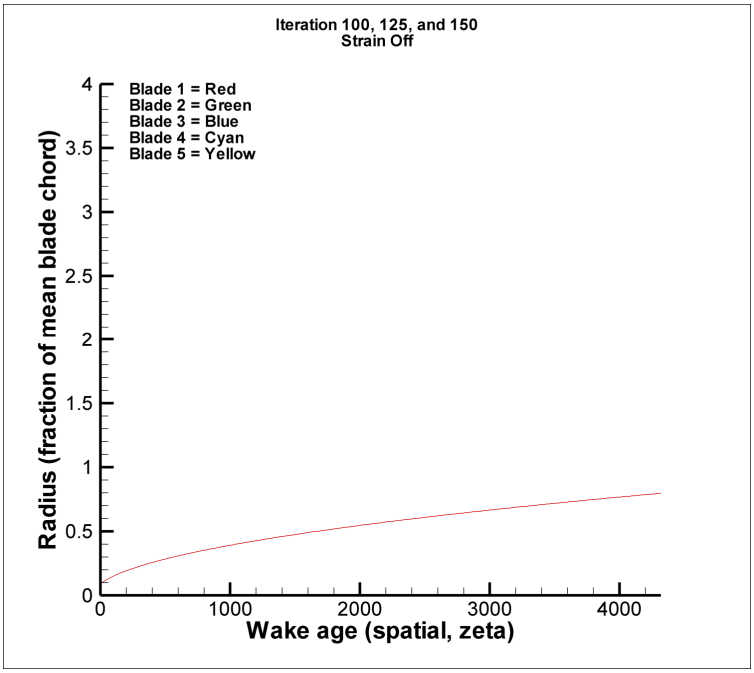

Figure 4.88: Core radius for the Strain Off case

4.4 CHARM Comparison

The goal of this additional model comparison was not to tune the model to improve the correlation with the wind tunnel data but to take the default values, change just what is necessary, and evaluate the results. The variables of importance are summarized in Table 15. The first input file, with the name, *filename*.inp, is the run characteristics input file. In this file, the number of rotors is defined to be one. The height above the ground is set to 3.5 feet. The forward speed is set to 26.12 ft/sec while the other velocities and rates are set to zero. The number of azimuth locations per revolution is set to 15. The maximum number of blade revolutions in the trim solution is set to 60. The number of time-marching revolutions to be performed after trim is set to 10. The wake geometry is initialized using convection and a simple inflow model. A simple inflow model is used for the initial wake-induced velocity on the blade. Setting IGPR = 0 means a time-marching (vice a relaxation solution) solution is used. Having ISCAN = 1 means that a grid of velocity points will be calculated. Finally, IFV = 2 means that the Hierarchical Fast Vortex Method (HFV) will be implemented.

For the *filename_bg*.inp file, which is the blade geometry file, the number of blade segments is set to one. The root cutout is defined. The blade segment length is set. This value, SL, should be equal to the blade radius minus the cutout distance. The chord, blade root twist, twist angle per segment, and thickness are defined. The NCHORD variable specifies the number of vortex lattice panels there are chordwise while NSPAN defines the number of panels spanwise. The ICOS variable, when set to zero, specifies that the vortex lattice is equally spaced both chord and spanwise.

For the *filename_rw*.inp file, which is the rotor/wake input file, the first variable on the list sets the number of blades. The rotational frequency is defined using the OMEGA variable. The IROTAT variable, when set to "1" sets the rotor rotation to counter-clockwise when viewed from the top. ICOLL forces the code to adjust the initial collective angle, COLL, until thrust, CT, is reached. ITRIM = 1 adjusts the cyclic inputs until the flapping values (in this case, zero) are reached. Setting NOWAKE = 0 is a flag that enables the free wake calculation to be performed. The variable ICNVCT = 0 forces the program to include all induced velocities in the calculation of wake geometry. NWAKES = 1 means that wake-on-wake induced velocities are not ignored between wakes of different blades. Setting IFAR = 0 means that no far wake is calculated. This flag needs to be set to a non-zero value only for hover and extremely low advance ratio cases. MBCVE = 0 means the basic curved vortex elements are used to evaluate the near-field wake-induced velocities. The variable ICORE must be set to one for the subsequent variables in the list to be called. AKINEM is the kinematic viscosity for the vortex diffusion model. If this variable is set to zero, the default value of 1.6E-4 ft^2/sec is used. The variable A1 is the turbulent diffusion coefficient in the vortex diffusion model. This author believes this is the same as the "dcy" variable in the MFW code. PCOREM is the power "n" used in the core model used to help model the vortex elements. Setting this value to 0 forces the use of the Scully core model.

The final file, *filename_bd*.inp is the blade dynamics file. Setting ISTRIM = 0 forces the calculation of the modal natural frequencies, masses and shapes to be done from a supplied input file. The variable IART, when set equal to 1, specifies an

articulated blade. HINGE sets the distance of this blade hinge, non-dimensionalized by rotor radius. The final variable sets the pre-cone angle, which in this case is equal to zero.

After specifying the variables in Table 4.11, the code was run. Two main files were output by the code. The first one was the wake geometry file. Post-processing the file, then plotting the results generated Figs. 4.89 and 4.90. The reason multiple iteration steps were not shown, like what was done for the MFW code, was that the wake structure did not change appreciably between iteration steps.

Table 4.11: CHARM input file variables.

filename.inp	
Paramter	Value
NROTOR	1
HEIGHT	-3.5
U/V/W/P/Q/R	26.12/0/0/0/0/0
NPSI	15
NREV	60
MREV	10
IRST	0
IFREE	0
IGPR	0
ISCAN	1
IFV	2

(a)

filename_bg.inp	
Paramter	Value
NSEG	1
CUTOUT	0.27156
SL	0.55135
CHORD	0.0925
TWRD	6.676
TWSTGD	-10.65
THIKND	.12
NCHORD	1
NSPAN	60
ICOS	0

(b)

filename_rw.inp	
Paramter	Value
NBLADE	5
OMEGA	320.7
IROTAT	1
ICOLL	1
COLL	5
CT	0.009
ITRIM	1
NOWAKE	0
ICNVCT	0
NWAKES	1
IFAR	0
MBCVE	0
ICORE	1
AKINEM	0
A1	0.001
PCOREM	0
CRMON	0

(c)

filename_bd.inp	
Paramter	Value
ISTRM	0
IART	1
HINGE	0.1
PRECONE	0.00

(d)

Examining Fig. 4.89, a clear roll-up of the filaments into two vortex bundles can be seen. The aperiodicity seen in the MFW code is not seen in the CHARM code's solution but the trailing edge filaments are not as tightly bundled, as evidenced by the side view of the wake structure in Fig. 4.90. The velocity field images at the same longitudinal positions as the MFW code and wind tunnel test results are presented in Figs. 4.91 through 4.93. CHARM does capture the "U" shaped out-of-

plane velocity area between the two vortices seen in the wind tunnel testing, something that the MFW was not able to do as well; Fig. 4.93 shows a faint out-of-plane "U" between the two vortices. Also the port and starboard vortex swirl velocities correlate quite well to the wind tunnel. However the positions of the two vortices at the three positions downstream in the CHARM code did not correlate as well with the wind tunnel as the MFW results.

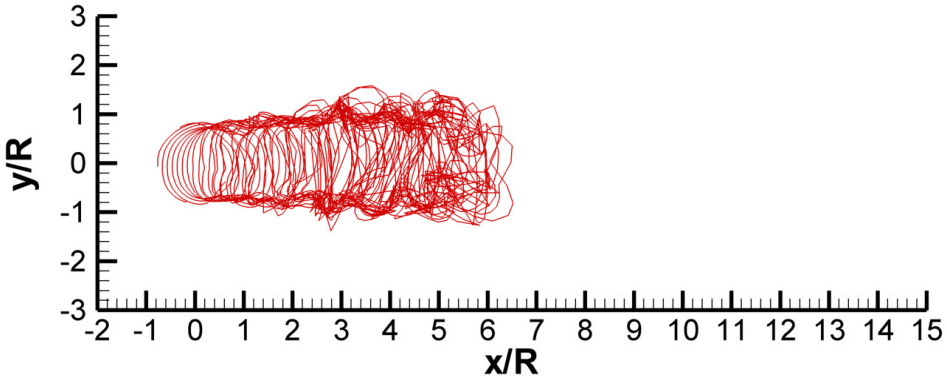

Figure 4.89: CHARM generated wake geometry. Advance ratio = 0.0997. Top View.

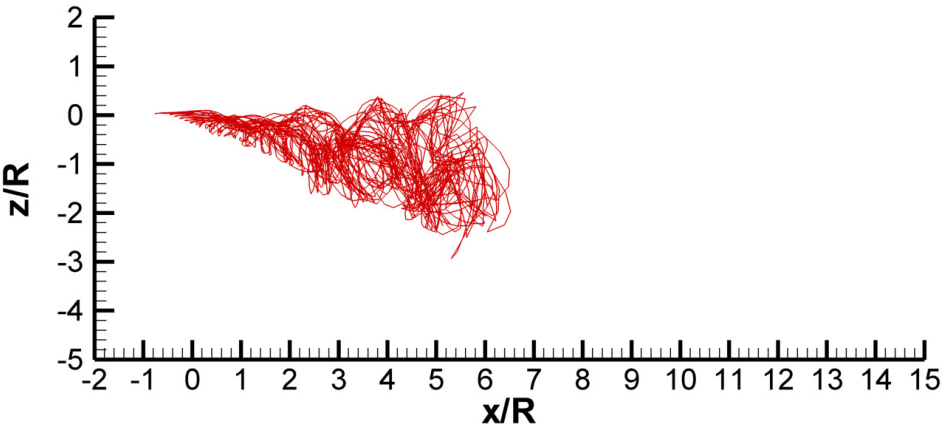

Figure 4.90: CHARM generated wake geometry. Advance ratio = 0.0997. Side View.

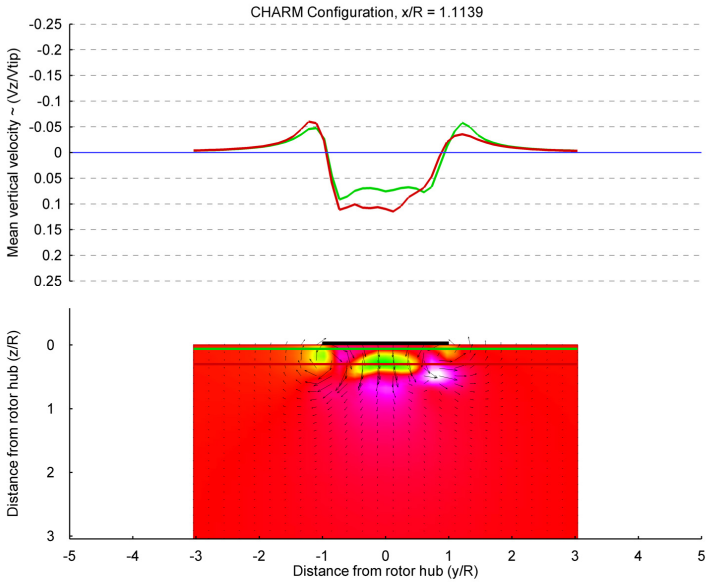

Figure 4.91: CHARM generated velocity field image. Plane is 1.1139 rotor radii downstream of rotor. Advance ratio = 0.0997.

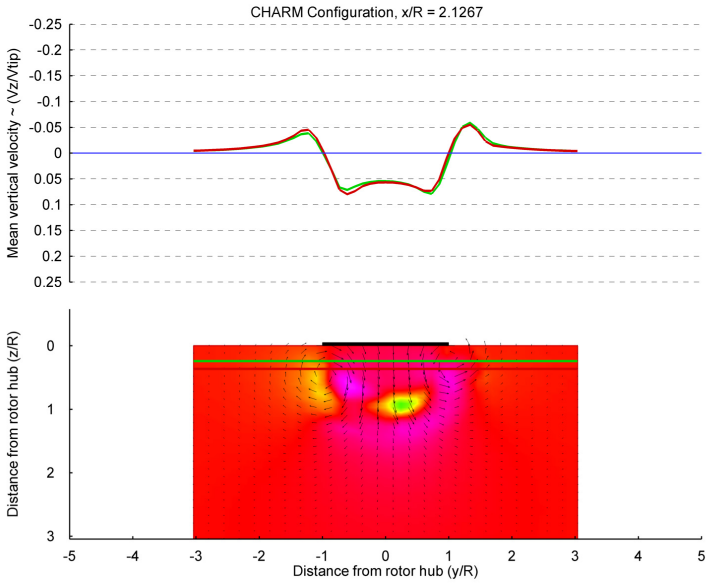

Figure 4.92: CHARM generated velocity field image. Plane is 2.1267 rotor radii downstream of rotor. Advance ratio = 0.0997.

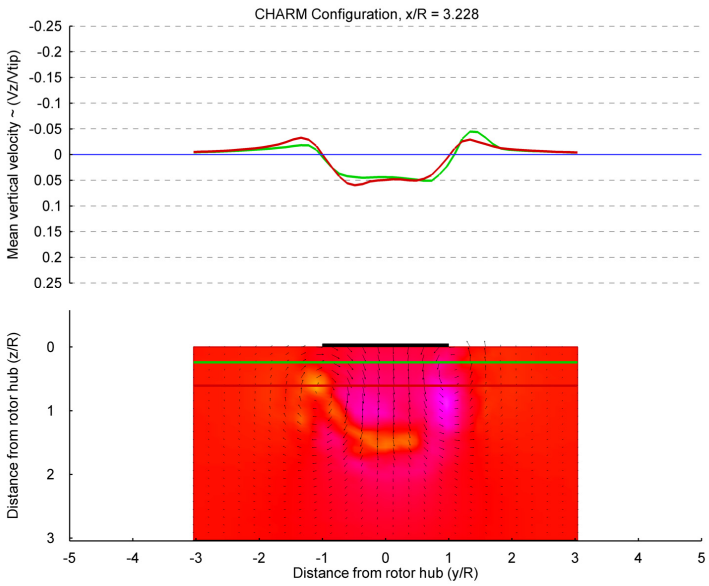

Figure 4.93: CHARM generated velocity field image. Plane is 3.228 rotor radii downstream of rotor. Advance ratio = 0.0997

Chapter 5

5 Summary and Conclusions

In 1999, while conducting shipboard operations, the V-22 Osprey's two rotors interacted with the rotor wake from an upwind helicopter resulting in the on-deck V-22 rolling outboard. The concern was that with a stronger interaction the V-22 could roll over the deck edge and into the water. A multi-phased flight test and wind tunnel test effort was undertaken to understand this phenomenon. While the wind tunnel data was gathered in support of the Roll-On-Deck investigation, the information obtained about rotor wake evolution lent itself readily to a free-vortex wake method validation, the focus being on the rotor far wake, multiple rotor radii downstream. The Maryland Free Wake method was the primary one used in this thesis while the CHARM code was used for cross-check purposes. The velocity field images from the wind tunnel test were compared to the ones generated by both methods. In attempts to improve the correlation between the Maryland Free Wake results and those from the wind tunnel, various rotor parameters were adjusted, the wake growth parameter was increased, and filament strain was removed, all with varying degrees of success. The key conclusions from this work are:

1. Regardless if the initial wake solution used in the MFW code is a prescribed wake or one from a previous run, at low speeds a wake transient develops after the first time step. This transient appears as a bundling of vortex filaments into a ring-like structure. The formation of ring-like wake structures

seems characteristic of the wake at low forward speeds, where the vortices have low helical pitch and lie close to one another.

2. The tendency to develop a wake instability increases as the vortex filament ages. This instability, when it occurs, affects the entire wake, both upstream and downstream of where the wake bundling appears. Upstream of the wake bundling, the effect appears more of a contraction of the wake in the lateral direction while downstream of the bundle the wake is stretched vertically. It is this phenomenon that seems to dominate the tendency for wake aperiodicity that was observed in the MFW solutions at low forward speeds.
3. The degree of aperiodicity is related to the amount of time the ring remains in the solution. The time is also related to the rotor's advance ratio, and how long a vortex filament remains in the solution. The higher the advance ratio or the lower the number of rotor turns before a filament's information convects out of the solution, the more the rotor wake solution becomes periodic.
4. The MFW solutions suggest that they could be potentially driven by Reynolds number effects. Increasing the wake growth parameter (tip vortex diffusion) to represent the low vortex Reynolds number of the sub-scale rotor did reduce the wake's aperiodicity, but only at the higher advance ratios. For an advance ratio equivalent to a full-scale of 30 kts, the MFW solution still exhibited very high amounts of wake aperiodicity, even with the modified wake growth parameter.

5. In the MFW program, the wake solution was found to be relatively insensitive to changes in rotor geometry parameters. Parameters such as the flapping hinge location, blade mass, and flapping spring stiffness were changed, and the effects of the changes analyzed. These modifications to the parameters did result in minor changes in the structure and strength of the wake but did not reduce the wake aperiodicity or how far downstream it occurred.
6. Overall, the degree of aperiodicity observed in the MFW solutions, was higher than that was observed in the sub-scale wind tunnel results used in the validation effort. This resulted in solutions that could be compared to measurements only for positions up to approximately three rotor radii downstream of the rotor. Beyond this point, the degree of wake aperiodicity made it impossible to get usable, phase-averaged results to compare against the wind tunnel.
7. The CHARM solution did not exhibit the same behavior as the MFW solution. After approximately two rotor radii downstream of the rotor, the filaments spread out vertically to a much greater degree than was seen in the MFW solution. This increased distance between the filaments and kept the filaments from bundling together and forming the filament rings observed in the MFW solution. This also more than likely kept the solution from developing the large degree of aperiodicity that was observed in the MFW solution.
8. While the CHARM solution had a decreased level of aperiodicity when compared with the MFW results, the rolled up vortex core positions in the far

wake were better predicted by the MFW code for the downstream positions that were examined.

9. While both codes, MFW and CHARM, have been successfully validated against empirical data made in the near wake, it would appear both methods have some degree of difficulty in correctly predicting far wake structure and strength for a sub-scale rotor operated at low advance ratios.

Recommendations for future research are:

1. Further investigation into the wake aperiodicity predicted by the MFW needs to be undertaken. While the behavior appears to be dependent on vortex Reynolds number and the wake growth parameter, a clear understanding of exact mechanisms that drive the aperiodic behavior remain unclear.

While free-vortex wake models have been used to calculate the near wake on helicopter rotors with some level of success, further research needs to be conducted, perhaps using larger, representative rotor models, to help improve the ability to predict the rolled-up rotor wake well downstream of the rotor. At higher advance ratios the downstream wake of a rotor appears as a pair of vortex bundles, similar to that seen behind a fixed wing, but predicting the stability of the wake appears to be an issue for free vortex wake models at low forward speeds.

6 Appendix A: Group B, D, and E Wind Tunnel PIV Images

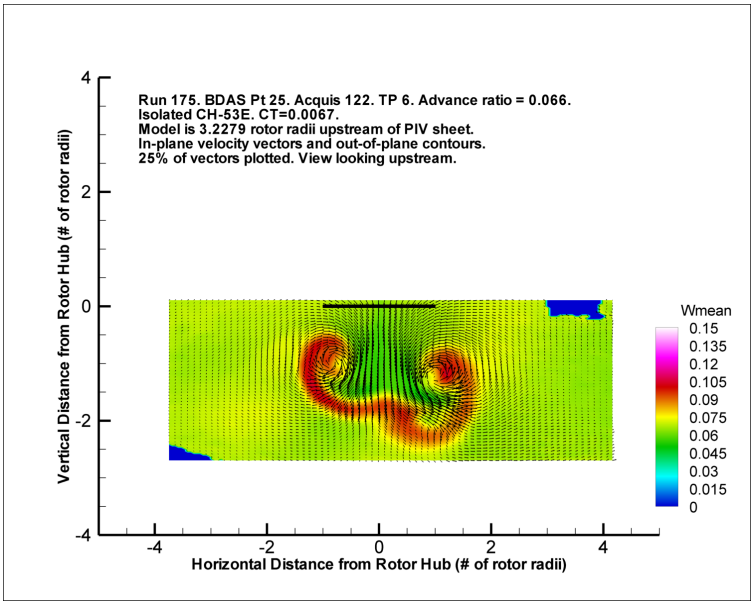

Figure 6.1: NASA Wind Tunnel PIV Image. C_T = 0.0067. Advance ratio = 0.0660. Model is 3.2279 rotor radii upstream of PIV sheet.

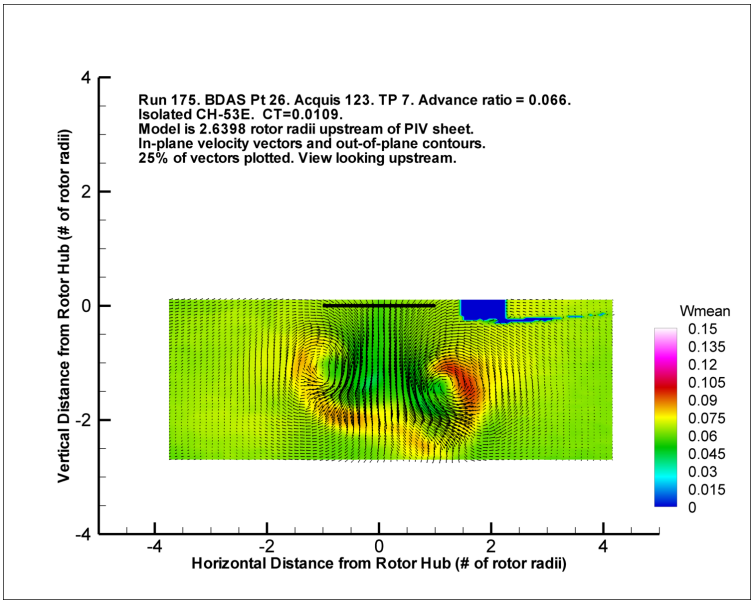

Figure 6.2: NASA Wind Tunnel PIV Image. C_T = 0.0109. Advance ratio = 0.0660. Model is 2.6398 rotor radii upstream of PIV sheet.

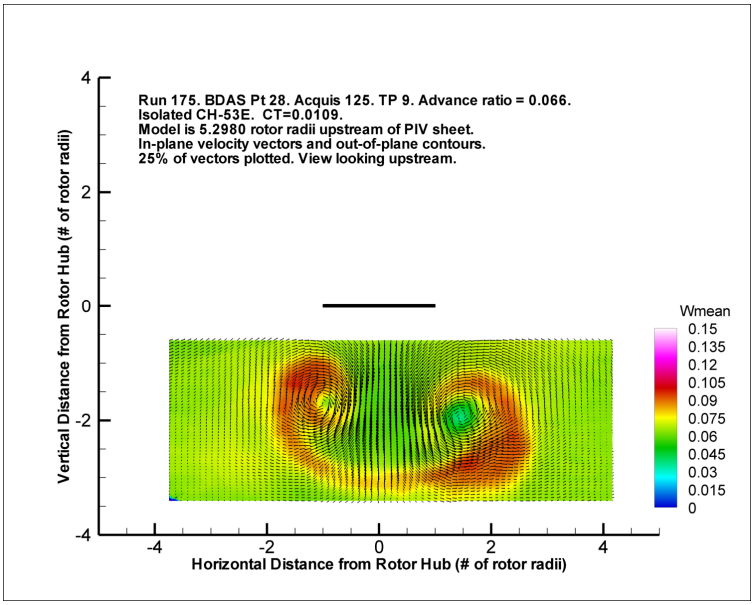

Figure 6.3: NASA Wind Tunnel PIV Image. C_T = 0.0109. Advance ratio = 0.0660. Model is 5.2980 rotor radii upstream of PIV sheet.

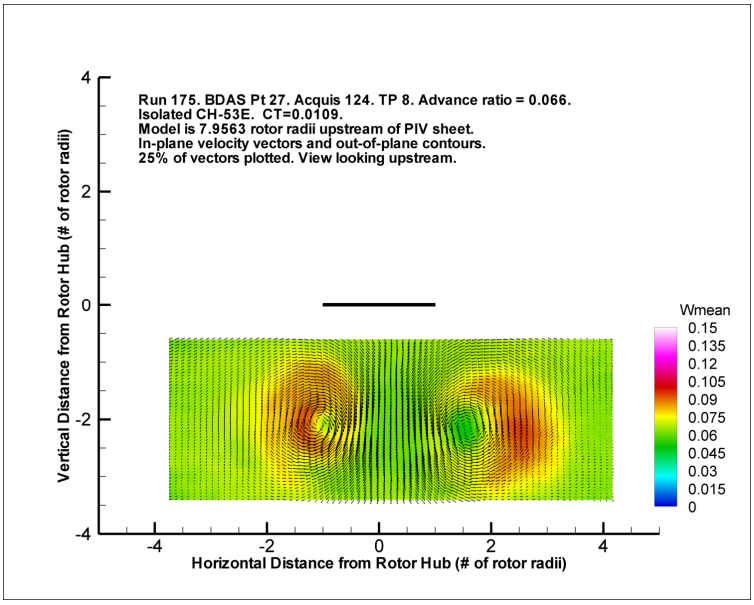

Figure 6.4: NASA Wind Tunnel PIV Image. C_T = 0.0109. Advance ratio = 0.0660. Model is 7.9563 rotor radii upstream of PIV sheet.

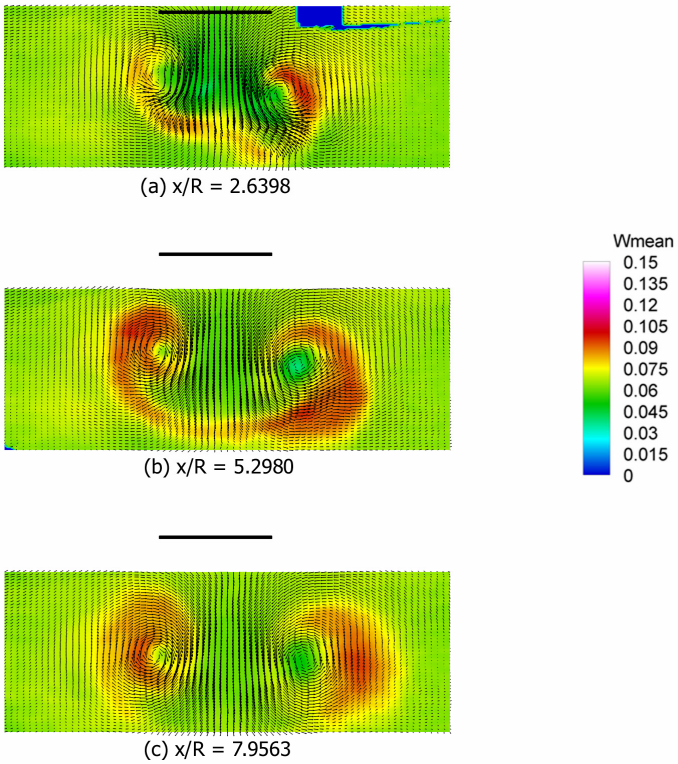

Figure 6.5: Summary of NASA Wind Tunnel PIV Images. C_T = 0.0109. Advance ratio = 0.0660.

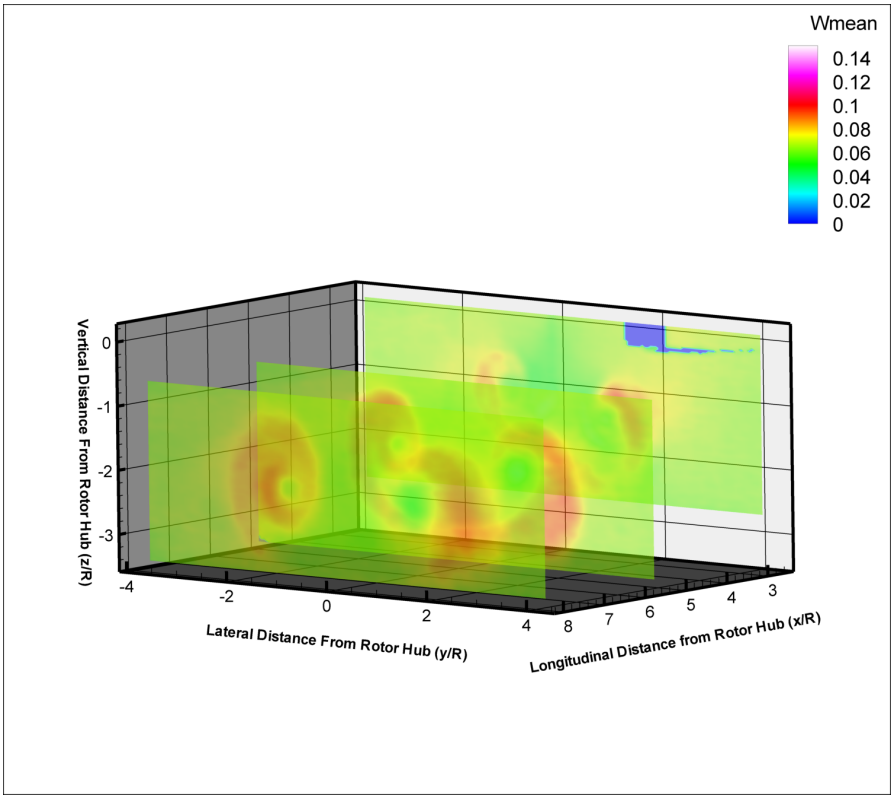

Figure 6.6: Isometric view of the NASA Wind Tunnel PIV images. C_T = 0.0109. Advance ratio = 0.0660.

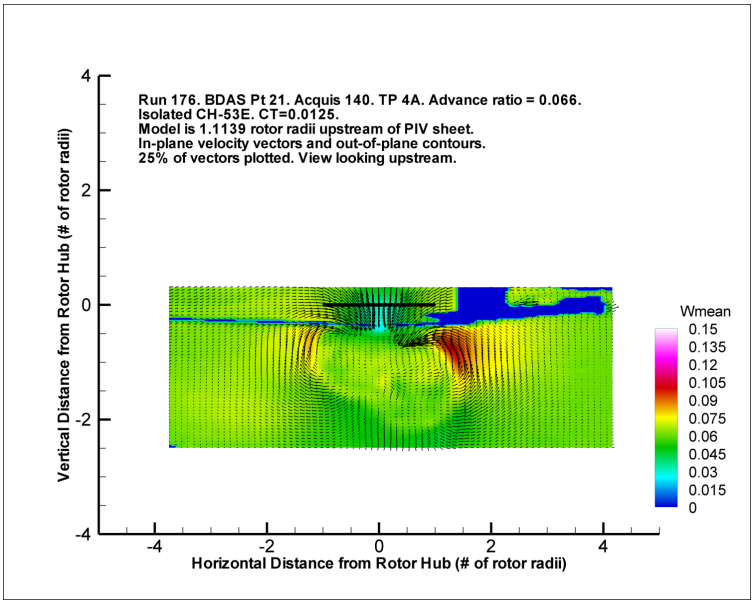

Figure 6.7: NASA Wind Tunnel PIV Image. C_T = 0.0125. Advance ratio = 0.0660. Model is 1.1139 rotor radii upstream of PIV sheet.

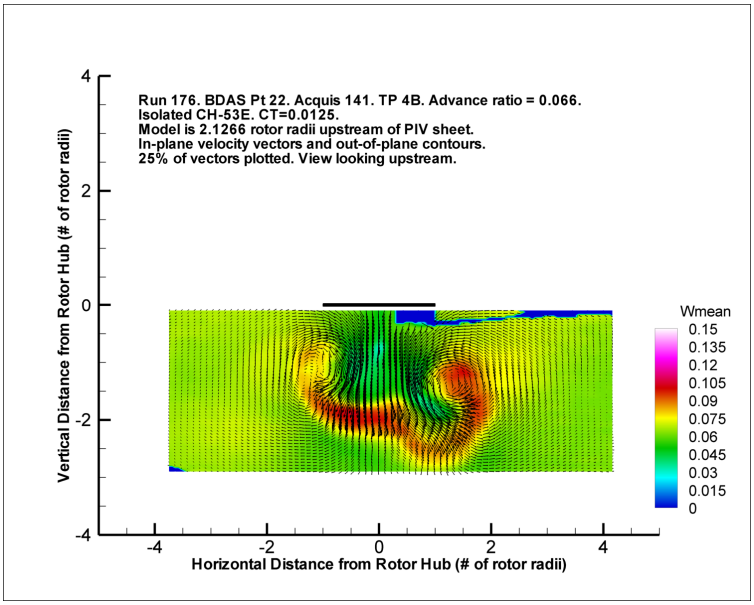

Figure 6.8: NASA Wind Tunnel PIV Image. $C_T = 0.0125$. Advance ratio = 0.0660. Model is 2.1266 rotor radii upstream of PIV sheet.

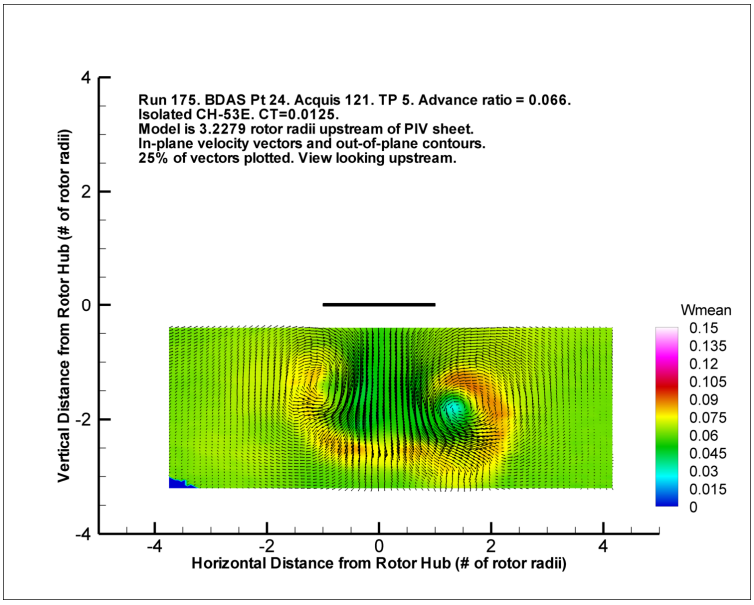

Figure 6.9: NASA Wind Tunnel PIV Image. $C_T = 0.0125$. Advance ratio = 0.0660. Model is 3.2279 rotor radii upstream of PIV sheet.

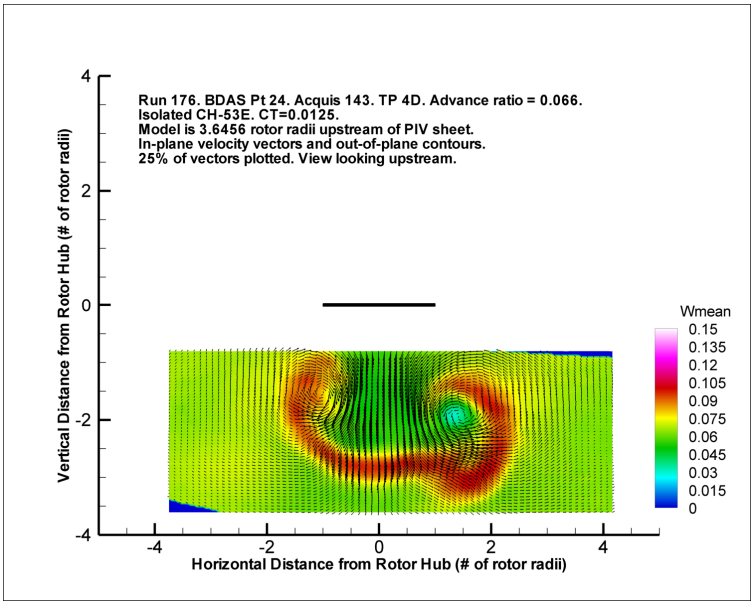

Figure 6.10: NASA Wind Tunnel PIV Image. C_T = 0.0125. Advance ratio = 0.0660. Model is 3.6456 rotor radii upstream of PIV sheet.

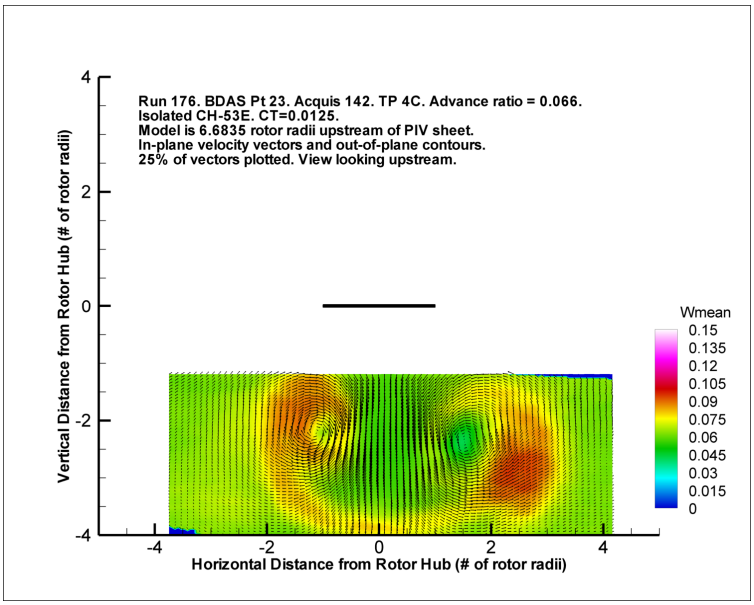

Figure 6.11: NASA Wind Tunnel PIV Image. C_T = 0.0125. Advance ratio = 0.0660. Model is 6.6835 rotor radii upstream of PIV sheet.

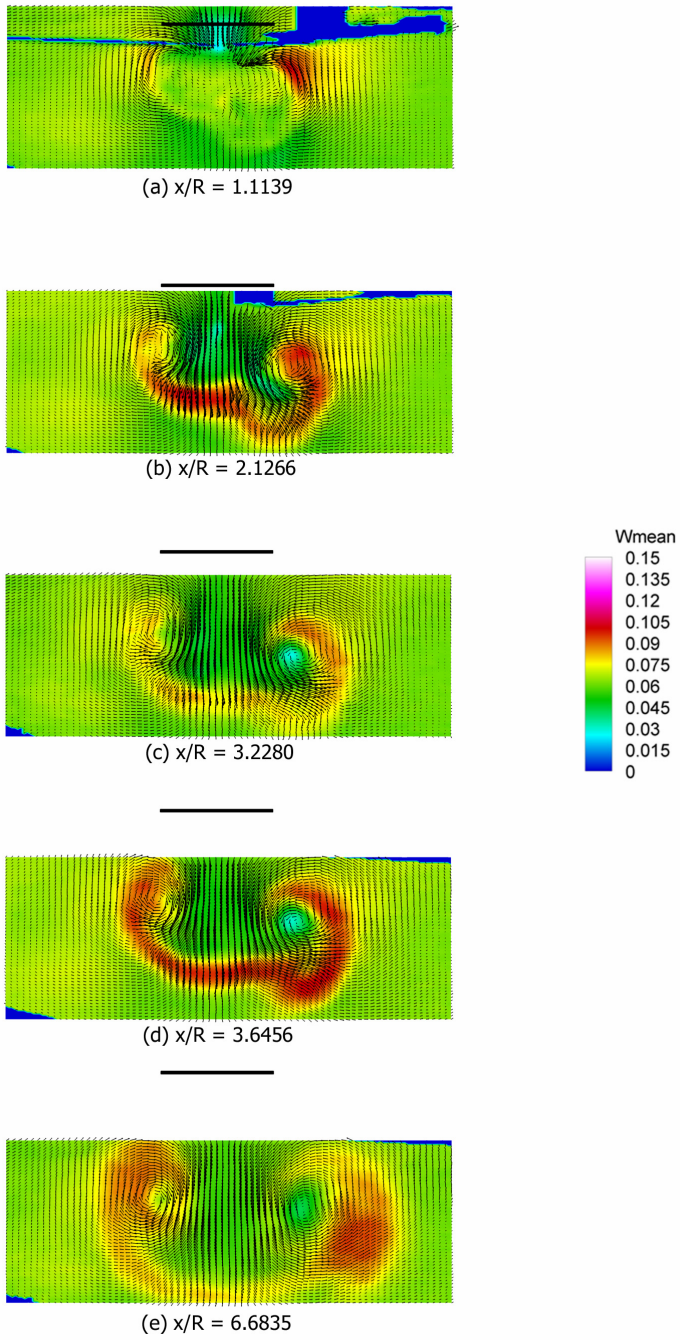

Figure 6.12: Summary of NASA Wind Tunnel PIV images. C_T = 0.0125. Advance ratio = 0.0660.

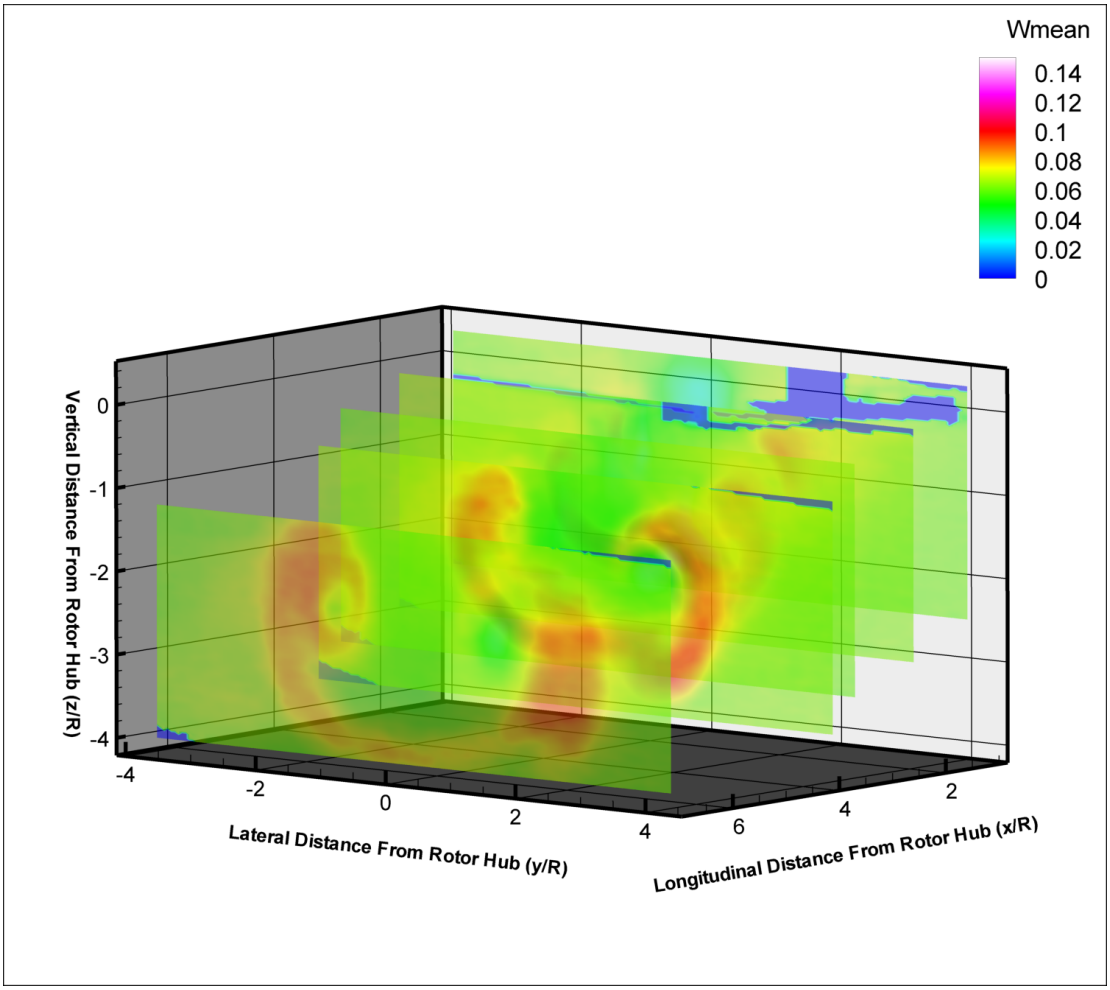

Figure 6.13: Isometric view of NASA Wind Tunnel PIV images. C_T = 0.0125. Advance ratio = 0.0660.

7 Bibliography

[1] McKillip, R. M., Keller, J. D., Quackenbush, T. R., Boschitsch, A. H., "Distributed Mult-Vehicle Simulation Including High-Order Airwake Representation," American Helicopter Society 60th Annual Forum, Baltimore, MD, June 2004.

[2] Leishman, J. G., *Principles of Helicopter Aerodynamics*, Cambridge University Press, New York, 2006.

[3] Silva, M. J., Geyer, W. P., and Nelson, J., "Full-Scale Rotorcraft Downwash Surveys in a Shipboard Environment," American Helicopter Society 60th Annual Forum Proceedings, Baltimore, MD, June 2004.

[4] Thorn, D. S., Nelson, J., de Brun, E. T., McCurdy, B. J., Silva, M. J., "Test Program to Address V-22 Uncommanded Roll While on the Deck of an Amphibious Assault Ship," Society of Experimental Test Pilots Conference, 2004.

[5] Silva, M. J., Wadcock, A. J., Yamauchi, G. K., van Aken, J. M., Shinoda, P. M., "Wind Tunnel Investigation of the Shipboard Aerodynamic Interactions Inducing the V-22 Uncommanded Roll On-Deck Response," American Helicopter Society 61st Annual Forum Proceedings, Grapevine, TX, June 2004.

[6] Silva, M. J., Wadcock, A. J., Yamauchi, G. K., Long, K., "Wind Tunnel Investigation of the Aerodynamic Interactions between Helicopters and Tiltrotors in a Shipboard Environment," American Helicopter Society 4th

Decennial Specialist's Conference on Aeromechanics, San Francisco, CA, January 2004.

[7] Johnson, W., Yamauchi, G. K., Derby, M. D., Wadcock, A. J., "Wind Tunnel Measurements and Calculations of Aerodynamic Interactions Between Tiltrotor Aircraft, " American Institute of Aeronautics and Astronautics, 41st Aerospace Sciences Meeting and Exhibit, Reno, NV, January 2003.

[8] Romander, E., Betzina, M., Silva, M. J., Wadcock, A. J., Yamauchi, G. K., "Investigating Tiltrotor Formation Flight Via 1/48-Scale Wind Tunnel Experiment," American Helicopter Socity 62nd Annual Forum, Phoenix, AZ, May 2006.

[9] Ananthan, S., "Analysis of Rotor Wake Aerodynamics During Maneuvering Flight Using a Free-Vortex Wake Methodology," Dissertation for Doctor of Philosophy, 2006.

[10] Simons, I.A., Pacifico, R. R., and Jones, J.P. 1966. "The Movement, Structure and Breakdown of Trailing Vorticies from a Rotor Blade," CAL/USAAVLABS Symposium on Aerodynamic Problems Associated with V/STOL Aircraft, Vol. 1-Propeller and Rotor Aerodynamics, Buffalo, NY, June 1966.

[11] Tung, C., Pucci, S. L., Caradonna, F. X., Morse, H. A., "The Structure of Trailing Vorticies Generated by Model Rotor Blades," NASA Technical Memorandum 81316, August 1981.

[12] Scully, M. P. and Sullivan, J. P., "Helicopter Rotor Wake Geometry and Airloads and Development of Laser Doppler Velociemeter for Use in

Helicopter Rotor Wakes, " Massachusetts Institutue of Technology, Al TR 179. 1972.

[13] Martin, P. B., Bhagwat, M. J., Leishman, J. G., "Visualization of a Helicopter Rotor Wake in Hover," AIAA 99-3225, 1999.

[14] Rossow, V. J., Tinling, B. E., "Research on Aircraft/Vortex-Wake Interactions to Determine Acceptable Level of Wake Intensity," Journal of Aircraft, Vol. 25, June 1988, pp. 481-492.

[15] Burnham, D. C., Teager, S. A., "Preliminary Measurements of Helicopter Wake-Vortex Velocity Profiles," DOT-TSC-FA527-PM-85-7, March 1985.

[16] Teager, S. A., Biehl, K. J., Garodz, L. J., Tymczyszyn, J. J., Burnham, D. C., "Flight Test Investigation of Rotorcraft Wake Vortices in Forward Flight," Federal Aviation Administration Technical Center, Atlantic City, NJ, Technical Report DOT/FAA/CT-94/117, February 1996.

[17] Schillings, J. J., Ferguson, S. W., Brand, A. G., Mullins, M. R., Libby, J., "Wake Vortex Measurements of the XV-15 Tiltrotor Using a Ground Based LIDAR System," American Helicopter Society, 57th Annual Forum, Washington D.C., May 2001.

[18] Egolf, T. A., Landgrebe, A. J. 1983. "Helicopter Rotor Wake Geometry and Its Influence in Forward Flight, Vol. I-Generalized Wake Geometry and Wake Effect on Rotor Airloads and Performance," NASA CR-3726.

[19] Beddoes, T. S. 1985. "A Wake Model for High Resolution Airloads," 1st International Conference on Basic Rotorcraft Research, Triangle Park, NC.

[20] Leisman, J. G., Bhagwat, M. J., Bagai, A., "Free-Vortex Filament Methods for the Analysis of Helicopter Rotor Wakes," Journal of Aircraft, Vol. 39, No. 5, September-October 2002.

[21] Strawn, R. C., Caradonna, F. X., Duque, E. P. N., "30 Years of Rotorcraft Computational Fluid Dynamics Research and Development," Journal of the American Helicopter Society, Volume 51 – Number 1, January 2006.

[22] Bhagwat, M., Moulton, M. A., Caradonna, F. X., "Hybrid CFD for Rotor Hover Performance Prediction," 24th Applied Aerodynamics Conference, San Fransisco, CA, June 2006.

[23] Derby, M. R., Yamauchi, G. K., "Design of 1/48th-Scale Models for Ship-Rotorcraft Interaction Studies," AIAA 2003-3952, 21st AIAA Applied Aerodynamics Conference, Orlando, FL, June 2003.

[24] Wadcock, A. J., Yamauchi, G. K., Heineck, J. T., Silva, M. J., Long, K. R., "PIV Measurements of the Wake of a Tandem-Rotor Helicopter in Proximity to a Ship," American Helicopter Society 4th Decennial Specialists' Conference on Aeromechanics, San Francisco, CA, January 2004.

[25] Rajagopalan, G., Niazi, S., Wadcock, A. J., Yamauchi, G. K., Silva, M. J., "Experimental and Computational Study of the Interaction Between a Tandem-Rotor Helicopter and a Ship," American Helicopter Society 61st Annual Forum, Grapevine, TX, June 2005.

[26] Weissinger, J., "The Lift Distribution of Swept-Back Wings," NACA TM 1120, 1947.

[27] Saffman, P. G., *Vortex Dynamics*, Cambridge University Press, Cambridge, UK, 1992.

[28] Beddoes, T. S., "Representation of Airfoil Behavior," *Vertica*, Vol. 7, No. 2, 1983, pp. 183-197.

[29] Leishman, J. G., "Aeroacoustics of 2-D and 3-D Blade Vortex Interaction Using the Indicial Method," American Helicopter Society 52nd Annual Forum, Washington, DC, June 1996.

[30] Leishman, J. G., Beddoes, T. S., "A Semi-Emperical Model for Dynamic Stall," *Journal of the American Helicopter Society,* Vol. 34, No. 3, July 1989, pp. 3-17.

[31] Leishman, J. G., "Subsonic Unsteady Aerodynamics Caused by Gusts Using the Indicial Method," *Journal of Aircraft*, Vol. 33, No. 5, September-October 1996, pp. 869-879.

[32] Bhagwat, M. J., Leishman, J. G., "Time-Accurate Modeling of Rotor Wakes Using A Free-Vortex Wake Method," AIAA CP 2000-4120, 18th AIAA Applied Aerodynamics Conference, Denver, CO, August 2000.

[33] Ramasamy, M., Leishman, J. G., "A Generalized Model for Transitional Blade Tip Vortices," Proceedings of the 60th Annual Forum of the American Helicopter Society International, Baltimore, MD, June 2004.

[34] Bhagwat, M. J., Leishman, J. G., "Generalized Viscous Vortex Model For Application To Free-Vortex Wake and Aerocoustic Calculations," Presented at the 58th Annual Forum of the American Helicopter Society, Montreal, Canada, June 2002.

[35] Wachspress, D. A., Quackenbush, T. R., Boschitsch, A. H., "First-Principles Free-Vortex Wake Analysis For Helicopters and Tiltrotors," Presented at the American Society 59th Annual Forum, Phoenix, AZ, May 2003.